Mitigation of High Temperature Corrosion in Waste-to-Energy Power Plants

Timothy T. Sharobem

Submitted in partial fulfillment of the
requirements for the degree of
Doctor of Philosophy
in the Graduate School of Arts and Sciences

COLUMBIA UNIVERSITY

2016

ABSTRACT

Mitigation of High Temperature Corrosion in Waste-to-Energy Power Plants

Timothy T. Sharobem

Waste-to-energy (WTE) is the environmentally preferred method of managing post-recycling wastes. In this process, municipal solid waste is combusted under controlled conditions to generate steam and electricity. Waste is by nature heterogeneous and has a substantially high concentration of chlorine (0.47-0.72 wt%) as compared to coal fuel. During combustion, chlorine forms several products, hydrogen chloride and metal chlorides, which can accelerate the high temperature corrosion of boiler surfaces, especially superheater tubes. This corrosion has been shown to significantly impact plant efficiency and profitability, causing unplanned shutdowns or preemptively forcing operators to limit steam temperatures.

This work focuses on the role of chlorine compounds on boiler tube corrosion and investigates approaches for minimizing its effects. The corrosion behavior was studied by conducting laboratory furnace tests on alloys of current and future interest of the WTE industry. Test specimens were coupons machined from boiler tubes to a nominal area of 3.2 cm^2 (0.5 in^2). An environment was simulated to replicate the fireside of superheater tubes by introducing a mixed gas stream comprised of O_2, CO_2, H_2O, HCl, SO_2, and N_2, at temperatures ranging from 400-550°C (752-1022°F). A salt layer with a loading of 4.0 ±10% mg/ cm^2 was applied to the coupons to replicate the behavior of boiler deposits. After each experiment, the corrosion rate was determined from the mass loss by applying an American Standard Testing Method (ASTM) protocol. Additional insight into the corrosion mechanisms was acquired by analyzing the

coupons using scanning electron microscopy (SEM) and elemental dispersive spectroscopy (EDS); and the coupon scale and salt layer with powder X-ray diffraction (XRD).

The addition of 800 ppm of HCl to a mixed gas oxidizing environment accelerated the corrosion rate of SA178A (Fe-0.1C) at 500°C (932°F) as determined by the change in the parabolic rate constant over a period of 72 hours, from 0.18 to 1.7 μm^2/h (3.0 E-03 to 2.5 E-02 mil^2/h). The compound analysis via EDS and XRD was consistent with literature and thermodynamic calculations that HCl accelerates corrosion via active oxidation mechanism.

A parametric study was performed on the effect of HCl on three alloys, SA178A, SA 213-T22 (2.5 Cr-1 Mo-Fe) and NSSER-4 (Fe-17Cr-13Ni). Varying the concentration from 400 ppm to 800 ppm at 500°C increased the mean mass loss by 17.5%, as compared to the 60% increase from 0 to 400 ppm. The corrosion increased sharply with temperature for each alloy between 450, 500, and 500°C, with corresponding apparent activation energies of $E_{a\ NSSER-4}$ 53 kJ/mol, $E_{a\ SA213\ T22}$ 110 kJ/mol, and $E_{a\ SA178A}$ 111 kJ/mol. The lower apparent activation energy for NSSER-4 demonstrates that the corrosion is diffusion limited. Also, it was determined that the corrosion rate under these conditions was not impacted by a temperature gradient, between the metal surface and the gas, of up to 250 °C.

Another important chlorine compound in WTE boilers are chloride salts, which are readily contained in fly ash. Using sodium chloride as a surrogate compound, the corrosion behavior below chloride salts was investigated by applying a salt layer (4.0 mg/cm^2) on coupon surfaces. Corrosion below the chloride layer was much more severe than below the HCl-containing atmospheres alone. The mass loss for the commercial steels was accelerated by more than an order of magnitude. Based on SEM and XRD coupon and corrosion product characterization, the acceleration of the mass loss was inferred to be caused by another active

oxidation mechanism in which the sodium chloride consumes protective or semi-protective oxides. The accelerated corrosion rates were realizable even after 24 hour furnace tests. This observation led to the development of a furnace test which could be used to rank new alloys.

The furnace tests were executed for six different nickel coatings, including Inconel 625 (Ni-Cr-Mo), SW1600, SW1641 (Ni-Cr-Mo-B-Si) and Colmonoy 88 and SP 99 (Ni-Cr-B-W). Colmonoy 88, showed superior corrosion resistance to the chloride environment with mass losses between 0.3-3.1 mg/cm^2 between 450-550°C. The mass loss of the Ni-Cr-Mo, and Ni-Cr-B-So were shown to be significantly higher between 10-30 mg/cm^2 The improved corrosion resistance was attributed to the alloying addition of tungsten, which has been previously shown to improve pitting corrosion resistance.

It was also shown that sulfate salts are semi-protective on WTE boiler tube surfaces up to temperatures of 550°C. The mass loss for carbon steel and Fe-17Cr-13Ni (NSSER-4) below sodium sulfate was an order of magnitude lower than corrosion sodium chloride. On the basis of these results, the SO_2/HCl ratio in the synthetic flue gas was increased from 0.3 to 0.6 and 1.0 respectively to determine the impact on sodium chloride corrosion. The surface of coupons was readily converted to from chlorine to sulfur demonstrating the effect of SO_2. As the ratio is increased above 0.3, the experiments showed that the corrosion of several candidate superheater tube alloys is reduced at temperatures as high as 500°C.

The impact of sulfating the alloy was observed most prominently with alloys that were aggressively corroded by the chloride layer. Tests showed a reduction in the corrosion rates of SA213 T22 (37%), Inconel 625 (23%), and NSSER-4 (27%); there was no change in corrosion rate for Colmonoy 88 At 550 °C, there was no trend with respect to increases of the ratio, which suggests that other corrosion reactions were faster than the rate of sulfation.

Finally, the annualized cost factor of using various metals was defined and can be used as a way of justifying the use of expensive, but more corrosion resistant alloys. For example, colmonoy 88 has an installation cost of 1.4 times the cost of the widely used Inconel 625 superheater tubes but, because of its superior corrosion resistance, a lower annualized cost.

Table of Contents

List of Figures

List of Tables

Acknowledgements

First, I would like to thank my thesis advisor, Professor Marco J. Castaldi for his guidance, patience, and support during the pursuit of my doctoral degree. I have been inspired by his diligence and unwavering passion toward research and chemical engineering. I am forever grateful for his confidence in me. I would also like to especially thank Professor Nickolas J. Themelis for his invaluable and generous support on this research. His expertise and knowledge in the field of waste management was an invaluable asset to my studies.

Many thanks also are due to my esteemed committee members: Professor Paul F. Duby, Professor Robert J. Farrauto, and Professor Siu-Wai Chan. Especially, Professor Duby has been a longtime mentor during my tenure at Columbia University, which began as an undergraduate transfer student in chemical engineering. He taught me innumerable, practical lessons on how to approach experimental research. I have also been fortunate to have been lectured by Professors Farrauto and Chan.

I gratefully acknowledge the financial support of the Waste-to-Energy Research and Technology Council (WTERT) of the Earth Engineering Center at Columbia University and its sponsors. Without them, this academic pursuit would not have been possible. I would like to express gratitude especially to Covanta Energy and the leadership of Steve Goff. I would also like to acknowledge Shang-Hsiu Lee, Eric Hanson, and Andrey Tovstukha for their valuable technical input and their generosity in providing materials for my experimental work.

I would also like to thank both former and current members of the Combustion and Catalysis Laboratory at the City College of New York and at Columbia University. I would like

Chapter 1: Introduction

1.1 Background

For millennia humans have had to manage waste. Initially, this concerned human excrement and sewage but in time also included municipal solid wastes (MSW), which are streams of matter generated from residential activities [1]. In the United States an average person generates 3.3 kg (7.2 lbs) of MSW per day which can include a variety of items such as paper, glass, metals, plastics, food wastes, among others. In total, the US manages 389 million tons annually [2]. Based on current domestic habits, these values will only increase over time.

After reuse and recycling there are only two methods that can manage waste at the rates at which it is generated, either disposal in a landfill or thermal treatment for material and energy recovery [3]. The latter is more commonly known as to waste-to-energy (WTE), in which MSW is combusted under controlled conditions, reducing its volume by 90%. The heat from the combustion gases is transferred through metal surfaces to steam which powers turbines for production of electricity [4].

Under the current state of waste management, landfilling and waste-to-energy will co-exist for the foreseeable future. However, in the face of global climate change, thermal treatment will become a more important approach for handling waste. Many studies have shown the environmental benefits of waste-to-energy [5-7]. One benefit, in particular, is the avoidance of methane which is released from landfills due to biological activity with MSW [8]. In the United States alone, landfill gas is the second largest source of anthropogenic emissions of methane and only 18% of it is captured and utilized as an energy source [9].

In 2007 a study between the Earth Engineering Center at Columbia University and NASA's Goddard Institute for Space Studies demonstrated how increasing the capacity of waste-to-energy can reduce methane emissions [10]. The major results are shown in figure 1-1 and figure 1-2. The study developed four scenarios of WTE growth, ranging from very conservative, in which the year 2000-2007 growth in capacity was assumed to remain at a constant rate of 2.5% through to the year 2030, to assumed increases in the rate of growth of WTE capacity of 5%, 7.5% and 10% per year, respectively, between 2010-2030. The only way to reduce landfill greenhouse gas emissions to the year 2030 is by achieving a 7.5% annual growth in WTE capacity globally.
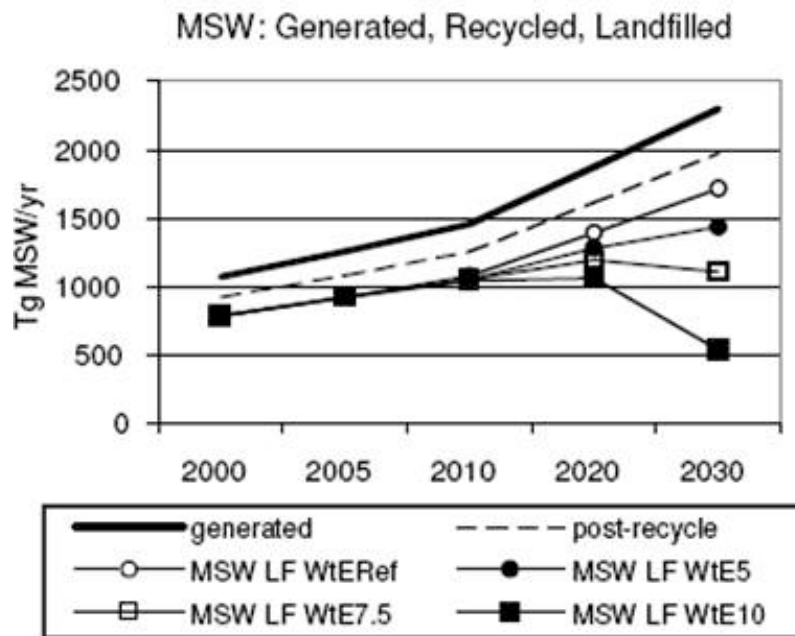
Figure 1-1. Rates of MSW generated, recycling and landfilling based on four WTE growth scenarios. Reference (ref) is an annual capacity growth rate of 2.5% [10].
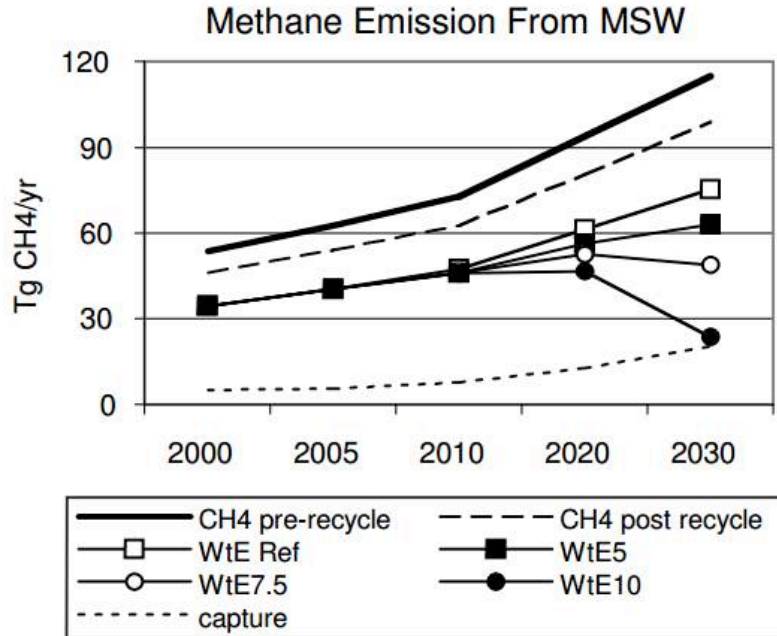
Figure 1-2. Impact of WTE growth on net methane missions from MSW. Impact of WTE growth scenarios on MSW landfilled is shown in figure 1-1 [10].

Another cited benefit of WTE is its classification as a renewable source of electricity by the Energy Policy Act of 2005, the US Department of Energy, and 24 state governments [11]. It was proven through carbon-14 measurements of (ASTM D6866 protocol) carbon dioxide in WTE stack gas that 64-66% of the total carbon in MSW is biogenic [12].

WTE has a significant advantage over other renewable electricity sources in that it is a mature technology which already provides baseload electricity and is located in populated areas where the power is most needed. Figure 1-3 is from a 2011 US Energy Information Administration (EIA) report on WTE plants in the United States. This shows the current electricity generating capacity by state. Most of the facilities operate in the northeastern US and in Florida. In total, 87 facilities convert approximately 30 million tons of MSW into 15 billion kWh [13].
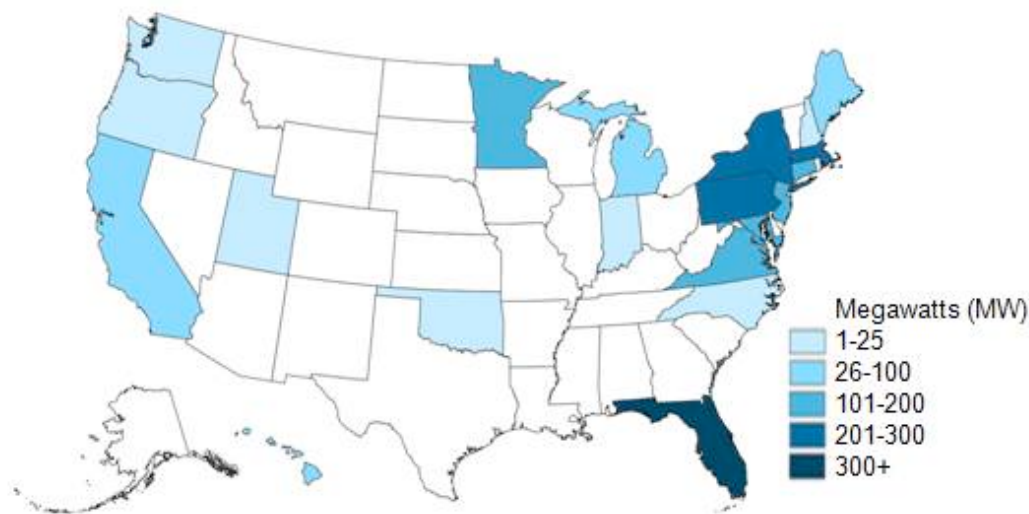
Figure 1-3. MSW electricity generating capacity in the United States [13]

1.2 Waste-to-energy technology

Analyses on the combustible portion of MSW have shown that an elemental composition can be expressed by the formula $C_6H_{10}O_4$, which has a calculated heating value of 23.5 MJ/kg [14]. In reality, MSW does not consist solely of combustible materials. It has significant moisture content (about ~20% in the U.S.) and a significant inorganic fraction comprised of metals, and glass, also about 20% by mass. In practice, the actual heating value of MSW is on the order of about 11.6 MJ/kg (~5000 Btu/lb) [15] or half the heating value of the combustible materials. Given the heterogeneous nature of waste, and variability in precipitation, the value of 5000 Btu/lb, is highly variable.

WTE plants are classified in two broad categories based on the characteristics of the fuel, mass burn and refuse-derived fuel (RDF) combustion systems. Mass burn systems are more common, 80% of the WTE plants worldwide, and are simpler in design, since they process waste "as received", directly without presorting. RDF systems aim to produce a more uniform material (and a higher heating value) by shredding, removing ferrous metal, and some additional

4

screening to remove grit or non-ferrous metal recovery [16]. The RDF technology was surpassed by mass burn facilities in the 1980s, as they were able to process larger tonnage and had the advantages of lower capital costs. Since the fuel is more heterogeneous, one tradeoff for mass burn plants is that it has a lower thermal efficiency [17].

A typical mass burn system is shown in figure 1-4. Waste is introduced via a moving grate which slowly moves the waste through the furnace and tumbles, exposing as many particles to the combustion air as possible, as they undergo drying, combustion, and burnout stages before the residue is discharged. The most common grate is the reciprocating grate and combustion air is injected into a furnace as underfire air, below the grate, and as overfire air, into the flame above the grate. Underfire air is injected into the hoppers below the grate to keep the grate cool and promote combustion. Generally, most mass burn furnaces operate at 50-100% excess air, with 50-70% of the total air fed as underfire air and the balance as overfire air. [18]. Afterward the flue gas passes through an integral waterwall boiler, superheater, and economizer, producing steam. The cooler flue gas is then cleaned by air pollution control (APC) equipment to remove fine particulates (fly ash), acid gases, and any remaining traces of organic compounds [19]. The burned out residue is discharged from the grate and is known more commonly as bottom ash.

1.3 Corrosion problem in WTE boilers

The combustion of MSW is different than that of any other fuels because of its heterogeneous nature. Besides its high moisture content, MSW contains elements such as chlorine, sulfur, alkali metals like sodium and potassium, and heavy metals like zinc and lead. During combustion these species can be liberated in the flue gas and produce an environment

which can cause fouling of heat transfer surfaces and even worse depletion of the heat transfer surfaces and tube failure.
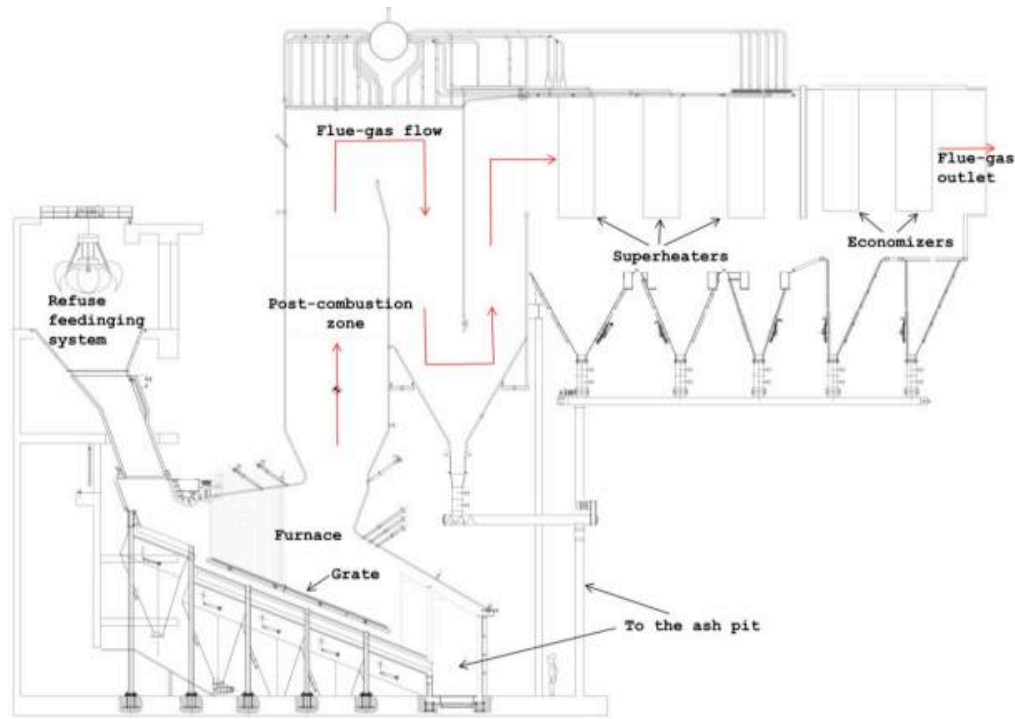
Figure 1-4. Typical Waste-to-Energy boiler configuration [20]

High temperature corrosion in WTE boilers typically occurs in three sensitive areas: the top of the refractory lining in the first pass, the transition of the first to the second pass, and tube bundles of the screen, evaporator and superheater [21]. The most aggressive corrosion, i.e. the fastest corrosion rate, occurs in the superheater as this is the metal surface which has the highest temperature. The corrosion behavior is generally referred to as high temperature corrosion- as it involves the transformation of the metal in an environment absent of a liquid electrolyte (which would be considered aqueous corrosion). The corrosion behavior is also referred to as fireside

corrosion, which indicates that the important gas-liquid-solid interaction occur between the outer surface of the boiler tubes with the flue gas environment [22]

The corrosion problems in WTE plants are realized in several ways. First, it is one of the common causes of shutdowns. It has been estimated that corrosion accounts for 70% of plant shutdowns [23]. Secondly, corrosion impacts plant profitability and the health of the waste-to-energy industry. It has been estimated that corrosion-related maintenance costs account for a third of the annual maintenance budget and can be as high as the 10% of the annual turnover [23]. Finally, the threat of unmanageable high temperature corrosion limits the thermal efficiency by forcing plants to operate at lower steam, boiler tube temperatures. It is not uncommon for example to have a WTE operate at 18-25% efficiency versus a coal fired plants which are on the order of 30% [24]. This is largely because the aggressive environment produced by the combustion of waste, most notably the presence of chlorine compounds

Previous literature and plant experience have identified chlorine, as the most problematic component of MSW, given its relatively high concentration in MSW and the various forms in which it is liberated from the furnace which can interact boiler alloys. MSW on average contains between 0.47-0.72 wt% chlorine [25]. Table 1-1 below is data adapted from a study estimating the chlorine content in MSW and shows a chlorine concentration within the specified range at 0.58 wt%. Plastics, largely due to polyvinyl chloride, PVC, are a significant source of chlorine, since they contain the highest chlorine per mass at 2.5 wt%. Paper, organics, and biomass have considerable chlorine content which can be either a part of organic (e.g. polyvinyl chloride) or inorganic compounds (e.g. sodium chloride) [25].

Table 1-1. Chlorine concentrations in MSW [25]

Waste component	% of component in MSW (average)	Cl concentration (g/kg)	Cl in MSW (g/kg)
Paper	29.4	2	0.59
Plastics	10.4	25	2.6
Organics	34.7	3	1.04
Textiles	4.4	12.5	0.55
Wood	2.7	12.5	0.34
Misc. combustible	5	12.5	0.63
Glass and metals	4	0.6	0.02
Metals	4.7	0.6	0.03
Misc. non-combustible	4.7	0.6	0.03
Total	100		5.82 (0.58%)

Recognition that chlorine in the refuse is the primary source of corrosion problems came slowly to the WTE community. Unlike other combustion based power plants, WTE power plants were not commonplace until the 1960s. As the pioneer WTE plants ran into severe corrosion problems, these were initially attributed to similar conditions occurring in coal plants (which are more related to various sulfur compounds). The largest body of work on WTE corrosion was initiated by engineers at Battelle Memorial Institute, the Electric Power Research Institute (EPRI) and jointly by the American Society of Mechanical Engineers (ASME) and the US Department of Energy (DOE) [26]. The largest collection of the development of that work can be found by ASME's Center for Research and Technology (CRTD) Report Volume 38 that was co-published with the U.S. Department of Energy.

1.4 Thesis Structure

The following thesis is aimed to identify the major causes of superheater tube corrosion in waste fired plants; understand the mechanisms of the underlying chemical reactions; and

recommend solutions that will allow superheated steam temperatures in WTE plants of 500°C and higher. The organizational structure of this work is as follows:

Chapter 2 provides background information elaborating on the chlorine corrosion problem in WTE plants, with particular interest to the reactions which occur with the superheater boiler tubes. Chapter 3 provides background on what has been developed in terms of preventive measures, including material selection, high temperature coatings, sacrificial surfaces, and additive injections. This literature review helps to provide a comprehensive understanding of the current areas of corrosion research and helps promote the experimental work discussed in later chapters. In particular, the role of alternative steels, high temperature coatings, and corrosion additives are explored experimentally and discussed in chapter 5-7.

Chapter 4 provides details on the execution of the laboratory corrosion testing, with the intent that the reader can reproduce the same experiments and analysis. Details are provided on the alloys tested, the synthesized WTE superheater fireside corrosion environment, the determination of the extent of corrosion and the characterization techniques.

Chapter 5 discusses the corrosion behavior of hydrogen chloride for three commercials steels: SA 178A, SA 213 T22, and NSSER-4. The effects of temperature, temperature gradient, and the concentration of hydrogen chloride are provided. This is followed by chapter 6 which focuses uniquely on the behavior below chloride salts, with sodium chloride used as a surrogate compound. As will be discussed, these salts are the some of the major components of WTE fly ash which have been shown to accelerate metal corrosion. In particular, this chapter will investigate conditions at which the chloride salt is at temperatures below the first melting

temperature (FMT). The commercials steels from chapter 5 are utilized for this discussion as well as 10 nickel based coatings- which may have promising

Chapter 7 investigates the impact of sulfur compounds- in particular sulfate salts and SO_2/SO_3 on the chlorine-metal interactions discussed in chapters 5 and 6. These studies help understand how variation in the waste feed (the sulfur, chlorine composition) can impact boiler corrosion at temperatures between 450-550°C. Furthermore, the results discussed in this chapter have relevance to the chemical additive technologies discussed in chapter 3, namely the sulfur recirculation technology currently tested by *Gotaverken Miljo* and the Chlorout additive, developed by *Vatenfall*.

Lastly, chapter 8 provides some additional context to some of the experimental results acquired in this thesis by discussing the economic impact of utilizing different alloys in the superheater and incorporating corrosion additives as part of boiler maintenance. Chapter 9 presents the conclusion of this study as well as recommendations for future work.

Chapter 2: High Temperature Corrosion Concepts

2.1 Oxidation of metals

With the exception of some areas in its first pass, WTE boilers contain an oxidizing gas environment, since MSW is fired with excess air. In the case of a bare (virgin) metal surface in contact with oxygen, metal oxide formation proceeds according to the following reaction:

$$M_{(s)} + O_{2\,(g)} \rightarrow MO_{2\,(s)} \qquad\qquad (2\text{-}1)$$

or more generally

$$xM + 1/2\,(yO_2) \rightarrow M_xO_y \qquad\qquad (2\text{-}2)$$
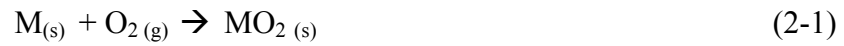
The spontaneous behavior is predicted by a negative change in the Gibbs free energy for the reaction at a given temperature, which is expressed as:

$$\Delta G^0 = \Delta H^0 - T\Delta S^0 \qquad\qquad (2\text{-}3)$$

where ΔH^0 is the change in enthalpy, ΔS^0 is the entropy change in the system, and T is the absolute temperature [27]. The Gibbs free energy can also be expressed in terms of the equilibrium product, which is expressed as the ratio of the activities of the products to the activity of the reactants. Specifically for reaction 2-1, this is a ratio of the metal oxide activity (the products) to the oxygen potential (equilibrium pressure), and the metal activity (the reactants)

$$\Delta G^0 = -RT \ln (a_{MO2}/a_M\, P_{O2}) \qquad\qquad (2\text{-}4)$$

In this expression, a_{MO} and a_M are the activities of the oxide and the metal respectively and P_{O2} is the partial pressure of oxygen. This dictates that an oxide will form on the surface of a metal when the oxygen potential in the environment is greater than the oxygen partial pressure in equilibrium with the oxide. In general, activity is the product of the mole fraction and the activity coefficient. Typically, ideal behavior is assumed for solids and activity of the metal and the metal oxide is assigned the value of unit. Applying this assumption, the Gibbs free energy can be expressed simply as a function of temperature and the partial pressure of oxygen.

$$\Delta G^0 = RT \ln (P_{O2}) \qquad\qquad (2\text{-}5)$$

The two expressions for the Gibbs free energy, such as 2-3 and 2-5, are plotted and can be obtained from Ellingham diagrams (the inclusion of the equilibrium dissociation pressure "P_{O2}" is known as an Ellingham-Richardson diagram). An example of this diagram is shown in figure 2-1 [28]. As discussed, the Gibbs free energy has linear relationship with temperature with a positive slope, which implies that oxidation reactions take place with a decrease in entropy, i.e., the product has a higher order than the reactants. Changes in slope in the diagram, such as that for MgO indicate a phase change, melting, boiling or a change in structure. On the right of the plot additional nomographic scales are shown on the right of the plot to express the equilibrium pressure of oxidants, such as O_2, H_2O, and CO_2 [29].

2.2 Oxide formation and growth

Although oxidation occurs also at room temperature, reaction kinetic is so slow that the consequences often are negligible. However, if the temperature is raised the rate of reaction may increase many orders of magnitude. Oxidation of a metal surface is considered to begin with the
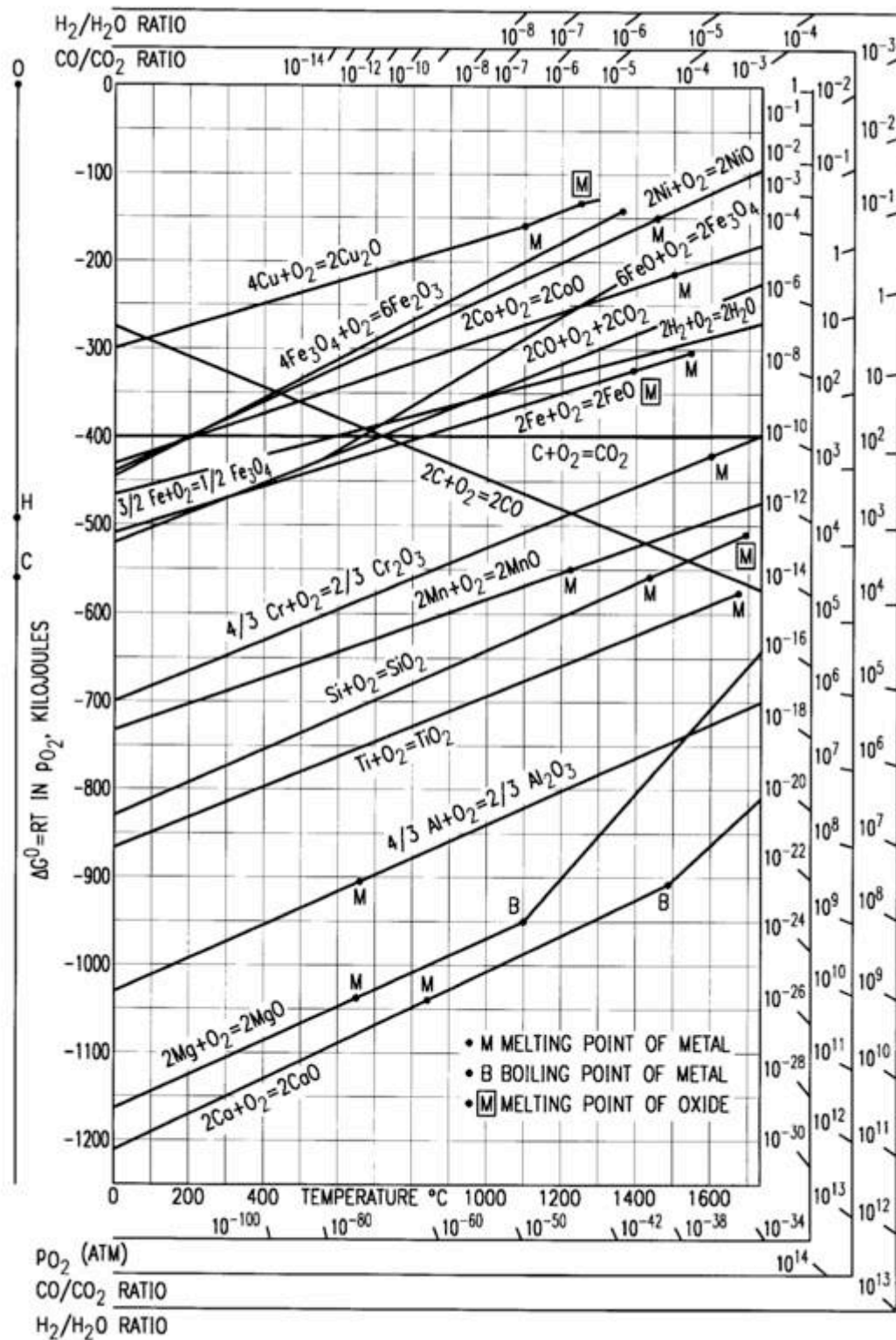
Figure 2-1. Ellingham-Richardson diagram. Additional nomographic scales are shown on the right to express the equilibrium pressure of oxidants, such as O_2, H_2O, and CO_2 [28].

adsorption of oxygen molecules from the atmosphere, followed by nucleation and thereafter the formation of a thin oxide layer as explained by Kofstad [30]. Once a thin film exists, oxidation can proceed only by the diffusion of reactants through the film. There are many factors influencing the oxide growth and a major one is the properties of the oxide layer. A defect-rich or porous oxide scale will be a less efficient diffusion barrier compared to a lattice with low defect concentrations [31]. The basic principles of oxide growth are illustrated in Figure 2-2.
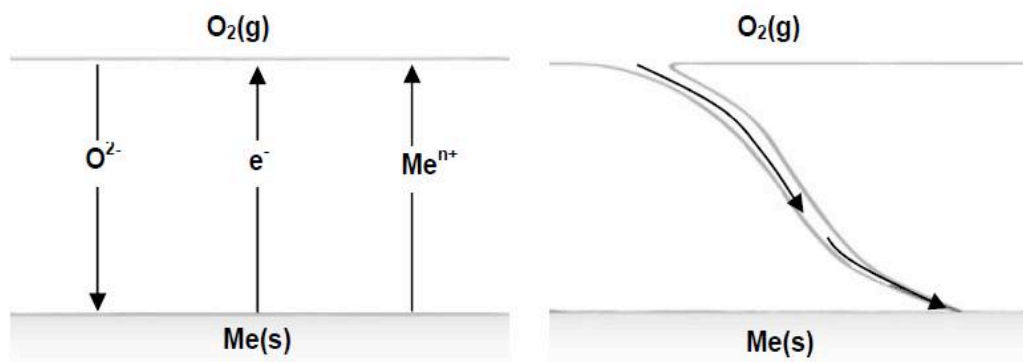
Figure 2-2. Schematic of oxide growth in a pure oxygen environment showing ionic diffusion across the scale (left) and defects in the scale that accelerate the diffusion rate or allow for molecular transport (right) [31].

2.3 High temperature corrosion kinetics

One of the limitations of the Ellingham diagram (figure 2-1) is that it does not take into account the kinetics of reaction. They can only be used to determine whether under certain conditions oxide formation is possible. There are three types of kinetic rate laws associated with the growth of an oxide layer. These kinetic expressions are also generally applied to all high temperature corrosion behavior, even in mixed gas environments in which more than one oxidizing agent is present.

Logarithmic Law usually represents oxidation in a thin layer regime. In the case of most metals heated at *low* temperatures, the kinetics follows logarithmic behavior. The rate of reaction rises very fast in the beginning and then slows down, either following a direct or inverse logarithmic law [32]. An example of the expression of the direct law is:

$$x = K* \log(t) + A \qquad\qquad (2\text{-}6)$$

where x is the change in weight as a result of oxidation or thickness of the oxide formed or the amount of oxygen consumed per unit area, and t is time.

Linear Equation is used to express a kinetic regime in which the rate of oxidation remains constant with time. In that kinetic regime, the oxidation is independent of the amount of the gas or metal previously consumed in the reaction. In this case, the rate of reaction is directly proportional to time and is expressed as follows:

$$dx/dt = K*t \qquad\qquad (2\text{-}7)$$

$$x = K*t + D \qquad\qquad (2\text{-}8)$$

The linear kinetic regime can sometime occur when an oxide layer undergoes spallation, in which the oxide layer growing on the surface is cracked, exposing unreacted metal underneath. This is also referred to as breakaway [33].

Parabolic Oxidation is the most common form of oxidation kinetics. This expresses that the oxide growth rate is decreasing with time. The rate of reaction is therefore inversely proportional to the scale thickness or the weight of the oxide formed. This is represented as:

$$dx/dt = K_p/x \qquad\qquad (2\text{-}6)$$

or after integration:

$$x^2 = 2\,K_p\,t + C \tag{2-7}$$

where x is either: the change in weight as result of oxidation, thickness of the oxide formed, the amount of oxygen consumed per unit surface area of the metal, or the amount of metal converted to the oxide, t denotes the exposure time, K_p is the parabolic rate constant, and C is the integration constant.

Most metal and alloys follow parabolic kinetics at elevated temperatures. The oxide growth process is usually governed by (i.e. the rate limiting step) by the diffusion of ions or electrons through the initially formed scale [34], as discussed in section 2.2. The rate constant, Kp, follows an Arrhenius relationship and can be therefore be expressed as a function of temperature [34].

$$K_p = A^* \exp(-E_A / RT) \tag{2-8}$$

where R is a constant 8.314 J/mol-K and T is absolute temperature (Kelvin) and E_A is the apparent activation energy. Figure 2-3 demonstrates what the oxide measurement would appear as over time in the different kinetic regimes.
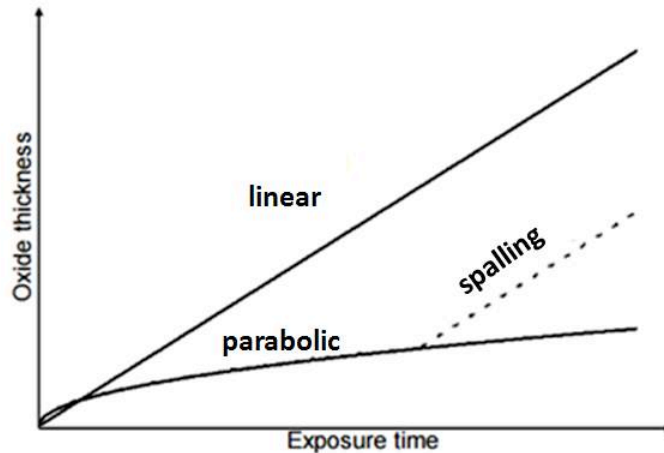
Figure 2-3. Oxidation kinetics for linear and parabolic oxidation [34]

2.4 Superheater environment

In addition to the oxidizing environment, the combustion of MSW contains several species which if liberated into the flue gas can participate in corrosion reactions- with the alloy surface and with the oxide layers. Table 2-1 is a summary of the ultimate analysis performed on various waste streams found in U.S. MSW, reported on a dry basis [35]. Other than the significant concentration of chlorine, there is a large concentration of ash, which can contain alkali metals such as sodium and potassium or heavy metals, such as zinc and lead. The major source of ash is from the glass and metal streams. The major source of ash is from the glass and metal streams. There is also an appreciable amount of sulfur in waste streams like textiles, but they are not as common in U.S. MSW. There is roughly 5-10 times more chlorine in MSW than sulfur [36].

The gas environment in a WTE boiler will depend on the components of MSW that were fed into the furnace, the moisture content of waste, and the percentage of excess air fired. Table 2-2 provides approximate ranges for the major gas species in WTE flue gas, taken from studies from various WTE plants [36].   In WTE superheaters, the metal temperatures typically range 400-450°C while the gas entering that pass is around 700-750°C. In addition to the species listed in table 2-2, there are others compounds present in the flue gas which can deposit or condense downstream onto boiler tubes. Some of these compounds have been identified by analyzing the boiler ash during shutdowns using X-ray diffraction (XRD), which is capable of identifying crystalline compounds. A list of the common species and the studies they were taken from is provided in table 2-3.

Table 2-1. Ultimate Analysis of MSW Fuel Based on US MSW Composition [35]

Waste component	Percent by weight (dry basis)						
	carbon	hydrogen	oxygen	nitrogen	sulfur	chlorine	ash
Paper and paperboard	43.5	6	44	0.3	0.2	0.06	5.9
Plastics	60	7.2	22.8	0	0	0.26	9.7
Textiles	55	6.6	31.2	4.6	0.5	0.55	1.6
Rubber and leather	69	9	5.8	6	0.2	0.06	9.9
Wood	49.5	6	42.7	0.2	0.1	0.34	1.2
Yard waste	47.8	6	38	3.4	0.3	0.11	4.4
Glass and metals	2.5	0.35	2.9	0.1	0	0.03	94.1
Food waste	48	6.4	37.6	2.6	0.4	0.03	5.0
Others (dirt, etc.)	26.3	3	2	0.5	0.2	0	68

Table 2-2. Typical range for flue gas composition in WTE boilers [36]

O_2 (%)	CO_2 (%)	H_2O (%)	SO_2 (ppmv)	HCl (ppmv)
5-11	8-14	10-20	0-150	250-1300

Table 2-3. Crystalline compounds in WTE fly ash identified by XRD [37-39]

Ref	Fly Ash Compounds
[37]	$NaCl$, KCl, $CaSO_4$
[38]	$NaCl$, KCl, $CaSO_4$, SiO_2
[39]	KCl, $NaCl$, Na_2SO4, $Na_2Ca_2(SO_4)_3$

2.5 Corrosion affected by hydrogen chloride

Most oxidation follows parabolic kinetics because the oxide layer becomes protective, that it mitigates additional oxidation underneath the formed scale. Chlorides can accelerate the oxidation of alloys by participating in reactions which yield the oxide layer un-protective, containing cracks or pores. The corrosion effect caused by HCl in an oxidizing environment is shown in figure 2-4. It is sometimes referred to as the chlorine cycle, as chlorine gas is regenerated after a series of reactions between oxygen, the oxide layer, and the metal [40].

HCl in the gas phase reacts with oxygen to form chlorine. In the reaction below

$$HCl_{(g)} + 0.5\ O_{2\ (g)} = H_2O_{(g)} + Cl_{2\ (g)} \qquad (2\text{-}9)$$
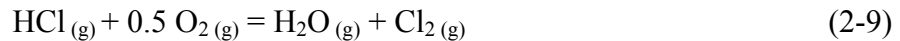
This reaction is sometimes referred as the reverse-Deacon reaction [40]. Chlorine (Cl_2) is thermodynamically favored over HCl at lower temperatures in an oxygen environment, as shown by the thermodynamic data (provided by HSC 5.1) in table 2-4.

Chlorine gas penetrates through the scale to the scale/metal interface. This step will occur if the oxide layer non-protective or semi non-protective. This would depend on the alloy or other gases under which the alloy is exposed. At the scale-metal interface, chlorine reacts to form metal chlorides. The presence of metal chlorides is generally not found in the scale, except at the metal-scale interface. This is because the oxide species is thermodynamically preferred over the chloride species in an environment in which sufficient oxygen is present. This is observed in a metal/alloy-O-Cl predominance diagram. An example of a predominance diagram for iron, Fe-O-Cl , at 500°C is shown in figure 2-5. The dotted lines connect the partial pressures of oxygen and chlorine that are present in the bulk of WTE flue gas.

Table 2-4. Thermodynamic data of reverse Deacon reaction (T = 200-1000°C)

Temperature (°C)	Gibbs Free Energy, ΔG (kJ/mol)
200	-26.5
300	-19.8
400	-13.1
500	-6.4
600	0.4
700	7.1
800	13.8
900	20.5
1000	27.2
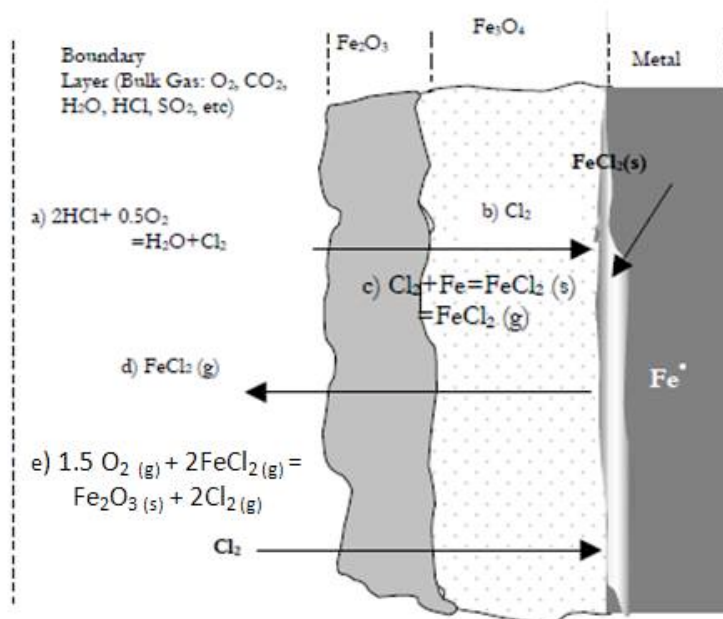
Figure 2-4. Schematic of active oxidation mechanism caused by hydrogen chloride gas [40]

If the temperature is sufficient, the metal chloride formed at the metal-scale interface has a high enough vapor pressure to diffuse outward through the scale. Examples of the equilibrium vapor pressure of chlorides are shown in table 2-4. The diffusing metal chloride vapor diffuses outward spontaneously reacts with the available oxygen to form metal oxide and release chlorine gas. An example of this is shown in the below between Iron (II) chloride and oxygen.

$$2FeCl_{2 (g)} + 0.5O_{2 (g)} \rightarrow 2Fe_2O_3 (s) + 2Cl_{2 (g)} \qquad (2\text{-}10)$$
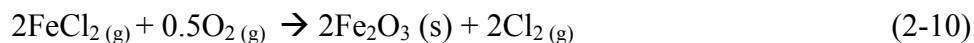
Chlorine is re-released which enables the gas either to participate in this network of reactions again, or to be swept by the bulk gas away from the metal surface. The active oxidation is generally accelerated in oxidizing-chlorinating environments in which the vapor pressure of metal chlorides is significant, typically 10^{-4} atm or greater [40].

2.6 Corrosion affected by metal chlorides

Alkali chlorides, such as KCl and NaCl, are some of the most common superheater tube deposits as shown in table 2-3. These compounds can participate in a few corrosion reactions. The first is similar to the active oxidation mechanism discussed for HCl. A schematic for the behavior using gaseous NaCl is shown in figure 2-4. The key feature is the formation of mixed oxides which provide an even, non-protective scale, and re-release $Cl_{2\ (g)}$.

Alkali chlorides can also release $Cl_{2\ (g)}$ when they are reacted converted to alkali sulfates in environments containing SO_2, O_2, and water via a sulfating reaction. Some authors have discussed that this reaction can reduce corrosion in WTE boilers despite the release of chlorine gas, speculating that the conversion of chlorides to sulfates reduces molten salt corrosion [42].
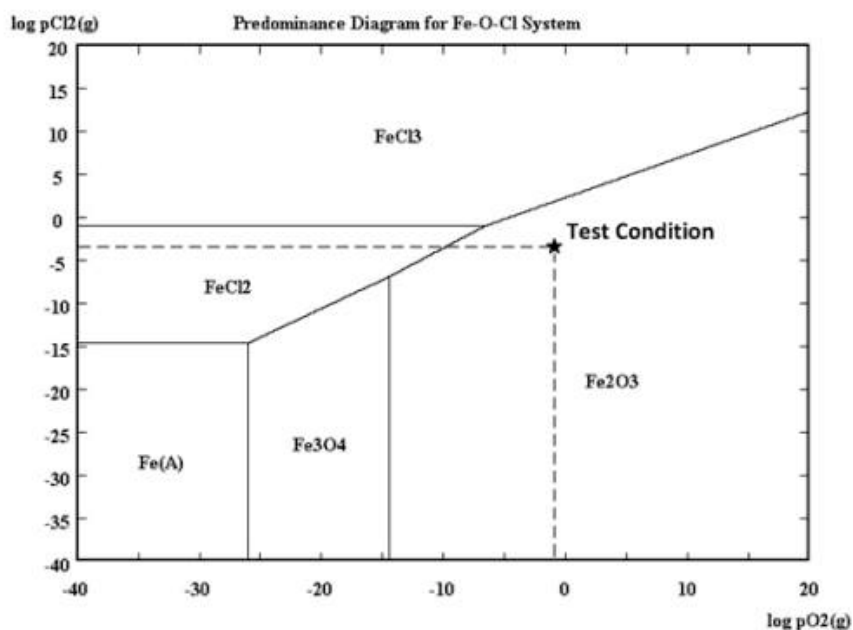
Figure 2-5. Predominance diagram of Fe-O-Cl system at 500°C

Chloride salts in contact with boiler tube alloy and scale can potentially form low melting point eutectics (i.e., salt solutions characterized by the lowest possible melting point) which may dissolve ("flux") the oxide layer that is protecting the metal surface [43]. Corrosion by molten salts is often termed 'hot corrosion' and is divided into type I and type II [44]. The type I hot corrosion refers to temperatures above the melting point of the condensed salt, while in type II a molten salt is formed below the melting point of the pure salt. In the latter case, the melting point is lowered due to dissolution of formed corrosion products. Table 2-5 gives a list of several chloride and sulfate species that may exist on the surface of boiler tubes during operation, the melting point of the pure species, and the concentration and temperatures of some common mixtures [45].

Hot corrosion studies have suggested a fluxing mechanism where an otherwise protective oxide dissolves in the fused salt and precipitates as non-protective particles within the salt or at the salt/gas interface. Due to fast transport in the liquid phase, corrosion by molten salts can have rapid kinetics [46].

Previous authors have shown that iron, nickel and chromium oxides are soluble in molten alkali chlorides and also that the solubility is dependent on the specific gas composition [47]. WTE field exposures have identified fused zinc and lead chlorides as a major concern, since these are known to have low melting points and form low melting eutectic mixtures with other salts [48]. In WTE operation, it is expected that even more complex mixtures, not found in binary or ternary phase diagrams, may be present.

2.7 Corrosion affected by sulfates

Sulfates can induce corrosion on WTE boiler tubes if a molten mixture is present. Individually sulfates are not an active species on WTE boiler tubes, as the metal temperatures are not hot enough. At elevated temperatures above 550° as has been experienced in coal-fired boilers, sulfates can from alkali metal trisulfates in the presence of SO_2 and O_2 [49]. The corrosion mechanism of those species is the sulfur analog of the chloride active oxidation, in that . A figure showing the different tube temperature regimes and the corrosion phenomena that dominates those sections is represented in figure 2-6.
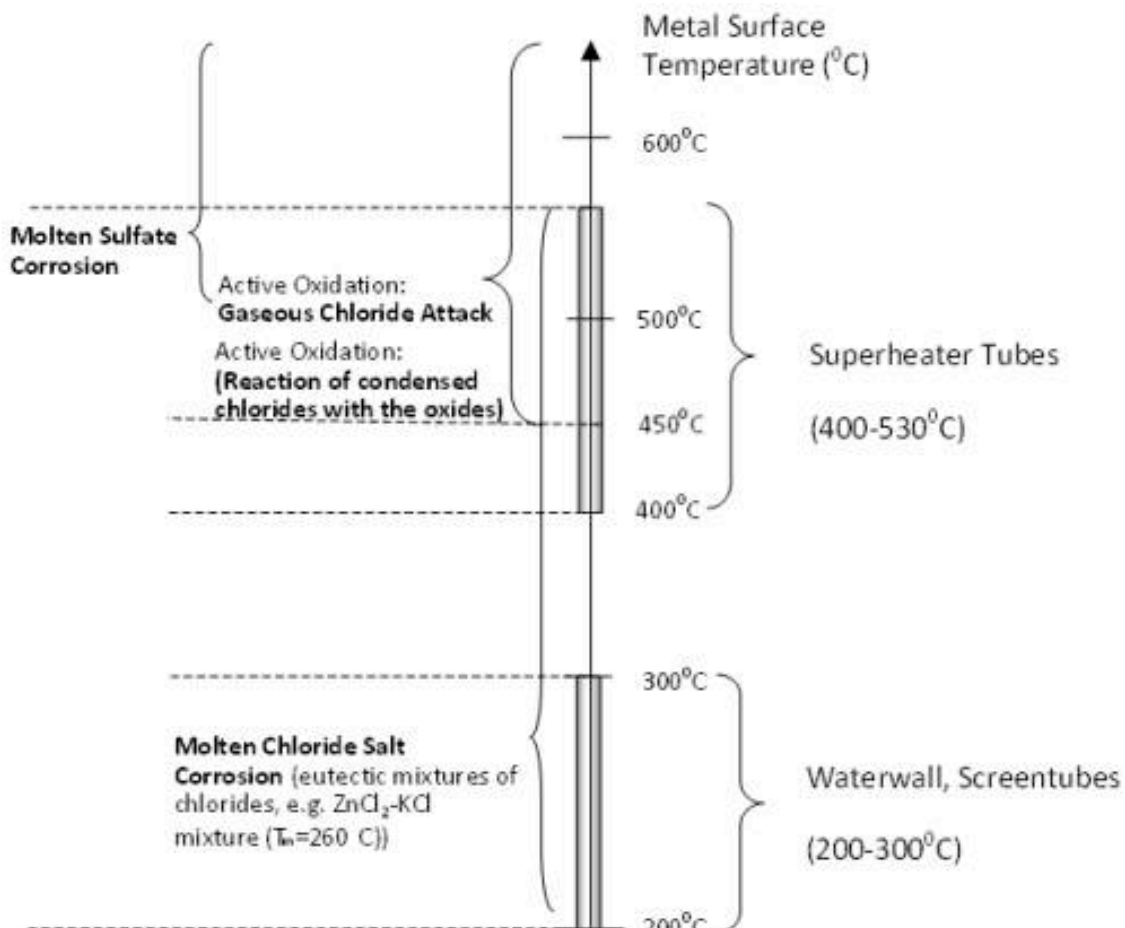
Figure 2-6. Schematic overview of possible corrosion attack in WTE boiler tubes

2.8 Conclusion

There are three major chloride high temperature corrosion mechanisms: active oxidation from HCl, active oxidation from alkali chlorides, and molten salt attack. Each mechanism accelerates tube corrosion by removing or weakening the oxide layer which **is** formed on the tube to naturally protect itself in surrounding environment. In order to prevent this corrosion, strategies need to be adopted to eliminate both HCl and metal chlorides, especially alkali chlorides. Chapter 3 discusses lessons that can be transferred from biomass boilers to WTE boilers on alkali chloride mitigation. In addition, other prevention methods and metallurgical studies are discussed.

Table 2-5. Melting temperature of pure salts and common WTE eutectics [50]

Compounds	Melting Temperature (°C)	Salt Mixtures (wt% mix)	First Melting Temperature (FMT), °C
$ZnCl_2$	283	$KCl-ZnCl_2$ (48:52)	230
$PbCl_2$	489	$NaCl-ZnCl_2$	262
$FeCl_2$	673	$KCl-FeCl_2$ (45.8:54.2)	355
$ZnSO_4$	730	$NaCl-FeCl_2$ (50:50)	370
KCl	775	$K_2SO_4-ZnSO_4-Na_2SO_4$	388
NaCl	801	$KCl-PbCl_2$ (21:79)	412
$CrCl_2$	821	$NaCl-PbCl_2$ (17:83)	415
Na_2SO_4	884	$NaCl-CrCl_2$ (53.7-46.3)	437
$NiCl_2$	1001	$KCl-CrCl_2$ (30-70)	462
K_2SO_4	1076	$KCl-NiCl_2$	508
$CaSO_4$	1400	$NaCl-NiCl_2$	560
$PbSO_4$	1170	KCl-NaCl	657

Note: for salt mixture, the wt% is 50:50 unless otherwise specified

Chapter 3: Solutions for mitigating chloride corrosion

3.1 Introduction

The steam temperature in a power plant is the maximum value for which the superheater design can produce electricity economically. This involves the assessment of two interrelated costs--the initial investment and the maintenance costs necessary to minimize operating problems, outages, and replacements [51]. Determining the optimum steam temperature is usually based on a number of factors including: (a) the alloy choice, (b) the surface area required to provide the superheater steam temperature, (c) the gas temperature zone in which the superheater tubes are located; (d) the permissible steam pressure drop in the tubes—which controls the steam flow; and (g) their arrangement in the boiler [52].

In order to promote higher steam temperatures and, therefore, higher thermal efficiency in WTE plants, modifications in the above factors are necessary in order to minimize the high temperature corrosion phenomena. In general, these measures can be classified as primary or secondary. Primary measures are modifications to the process conditions whereas secondary are metallurgical solutions [53]. Some of these solutions are suited for new plant designs, whereas others can be affected during the plant shutdown period. In this chapter, the modifications suggested focus specifically on mitigating high temperature corrosion mechanisms of chlorides. Some of the methods described in this chapter are based on the experience of biomass-fired power plants, which like WTE plants have significant chloride corrosion problems.

3.2 Material Selection

Most of the materials used in boilers are steels, the majority of which are low alloy or carbon steels. Carbon steels are alloys of iron with about 0.05 to 1 wt% carbon. Low alloys steels include other elements at compositions of about 2 wt% or less for improvements of mechanical properties. Two examples of these materials, SA 213 T22 and SA 213 T11, are listed in Table 3-1, which lists common alloys found in WTE superheater tubes- based on plant survey and correspondence with the WTE industry. Low alloy steels are attractive for their relative inexpensive, while possess a wide range of strength and hardness [54]. Because of these benefits these alloys serve as the base metal for superheater in highly aggressive environments with another alloy—a protective layer applied to it.

While typically 2.5 times more expensive [55] than low alloy steels, stainless steels are an attractive alternative because of their increased oxidation resistance. By definition stainless steels contain at least 10.5% chromium. Oxidation resistance increases with increasing chromium content. They are classified as ferritic, austenitic, duplex, martensitic, and precipitation hardening. Each classification has its own special characteristics, which are well known in the literature. Austenitic stainless steels are widely used in industry for its corrosion resistant properties. The addition of nickel to iron-chromium alloys stabilize the face-centered cubic austenite phase and works with chromium synergistically to improve corrosion resistance- by forming a thin, chromium rich oxide layer on the gas-metal surface [56, 57]. In WTE power plants, the most common austenitic steel for boiler applications is TP 310H, the composition of which can be found in Table 3-1.

In general, a practical approach of extending the lifetime of boiler tubes is the application of a highly alloyed alloy coating with a thickness less than or equal to 3 mm [58]. This is an

enticing option because of difficulties associated with mechanical properties, workability, and high material price. The role of coatings is to provide a metal surface composition which will react with the environment to produce the most protective scale possible. Nickel has intrinsically low corrosion rates in oxidizing-chlorinating environments compared with the other major base metals in high temperature alloys. Additions of chromium, molybdenum, and tungsten to nickel based alloys have all shown to improve oxidation resistance [59]. Two of the more common deployed nickel based alloys are provided in Table 3-1. To bring perspective on cost, the purchase cost of an Inconel 625 cladded superheater is approximately 4.5 times for the same area [60]. Based on the corrosion performance and lifetime, this cost can be considered prohibitive or attractive.

Table 3-1. Common superheater tube alloys in WTE power plants [61]

Alloy	UNS	Ni (%)	Cr (%)	Mo (%)	Fe (%)	Other (%)
Inconel 625	N06625	63	22	9	1.5	3.4 Nb, 0.2 Si, 0.2 Mn
Incoloy 825	N08825	42	21.5	3	29.8	2.2 Cu, 0.9 Ti
SA 213 T22	K21590		2.25	1	95.5	0.3 Si, 0.1C, 0.5 Mn
SA 213 T11	K11597		1	0.5	97.3	0.4 Mn, 0.4 C, 0.3 Si, 0.1 C
TP 310H		20	25		51.8	0.7 Su, 2 Mn, 0.6 C, 0.8 Nb

Coatings can be produced on boiler tubes by several methods: co-extrusion, weld overlaying, diffusion treatment, thermal spraying, and laser cladding [62]. The application method can sometimes diminish the corrosion performance of a material. For example, weld overlay Ni-Cr-Mo coatings (such as Inconel 625) have not performed well at high temperature WTE superheaters because of iron migration to coating from the base metal due to the high heat load during welding [63]. Such migration does not occur for high velocity oxy-fuel coatings

(HVOF). Laser cladding, similarly to weld overlay, is prone to iron migration, as a result of high dilution with the base material [64,65].

Table 3-2 provides several examples of different types of coatings that have been investigated at WTE superheater conditions along with the specific parameters.

3.3 Boiler design modifications

3.3.1 Extending the length of the passage between furnace and superheater

In Europe, several WTE power plants, have deployed methods for removing alkali chlorides. Two Swedish plants in Södertälje and in Norrköpinga , extended the length of passage between the furnace and the superheater via addition of a separate radiant pass. This allows for the undesirable ash components to fall out of the flue gas before reaching the superheater. Additionally, sulfur granules are added to the furnace to alter the S/Cl ratio (see section 3.4) which increases the melting temperatures of the ash, because sulfates have higher melting temperatures than chlorides. The additional pass allows for a longer residence time for the completion of the sulfation reaction. Water cannons are installed on the sides of the empty pass to clean the walls and spring hammers remove agglomerated deposits. This arrangement allows for a tolerable superheated steam temperature to be as high as 540°C [66].

Table 3-2. Studies of coatings investigated in WTE environments

Alloy(s)	Temperatures (°C)	Environment	Ref
Inconel 625	650	Molten deposits of tin, lead, zinc chloride	67
Fe-12Cr-Mo-V	500-600	eutectic mixture of $PbCl_2$-KCl in air	68
HVOF Coatings: 75Cr3C2-25NiCr; Cr3C2; NiCrSi; Ni20Cr15Mo; WC-1	450	air oxidation with fly ash from biomass- fired boiler (high Ca, K, Cl)	69
HVOF Coating: 75% Cr3C2-25% Ni20Cr	450	biomass fired boiler fly ash	70
HVOF wired sprayed coating: Al/80% Ni-20%Cr	400	field test, WTE plant	71
Laser cladding Alloy 625	300-500	HCl, SO_2 containing synthesized flue gas	72
Sealed flame spray, HVOF, laser cladding of Alloy 625	400-500	HCl, SO_2 containing synthesized flue gas	73
HVOF sprayed NiCr, NiCrBSi, Cr3C2-NiCr	500	HCl, SO_2 containing synthesized flue gas	74

3.3.2 Chloride Trap- collecting fly ash on screen tubes prior to the superheater

In Schweinfurt, Germany, the GKS WTE plant has an extended boiler pass that was retrofitted with a section of screen tubes. As the flue gas flow turns into the extended pass, the flow encounters a section of screen tubes, which are maintained in the temperature range of 300-400°C (Figure 3-1). Low melting ash components condense on the walls of the empty pass. This modification has been referred to as "chloride trap", as the deposits are rich in chlorides. An image of the deposits is shown in Figure 3-2. Deposits are removed daily via the horizontal wash system "HWS" which is shown in Figure 3-1 [75].
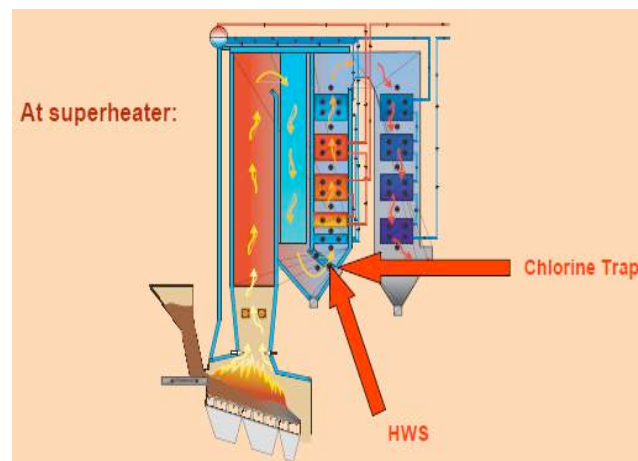
Figure 3-1. Schematic of GKS Boiler in Schweinfurt, Germany [76]

3.4 Chemically modifying fly ash

3.4.1 Co-firing MSW with high sulfur coal or elemental sulfur

Firing high ash coal along with MSW (or biomass) can modify the WTE fly ash chemical composition. The combustion of high sulfur coal generates a significant amount of acidic ash particles (SiO_2, Al_2O_3) [77]. These amorphous, high surface area particles provide sites for the alkali chlorides to trap and collect, instead of passing through with the rest of the flue gas as

Figure 3-2. Accumulation of deposits on chloride trap [76]

vapor. In the presence of higher SO_2/SO_3, the chlorides are converted to sulfates which are much less likely to form melts or undergo hot corrosion with boiler tube alloys [78]. While this measure has been shown to be effective, co-firing of coal in a WTE boiler as a means for corrosion reduction, is not considered to be an economically viable option [79].

3.4.2. Ammonium sulfate additive for corrosion and NO_x reduction

The purpose of ammonium sulfate injection is to obtain the same benefits as co-firing with high sulfur coal mentioned above, but it is economically more viable. This is achieved by the dual benefit of increasing the SO_3/SO_2 levels in the boiler and, also, providing an additional function in selective non-catalytic reduction of NOx molecules (SNCR). This method is commercialized in Europe by Vattenfall and is called the *Chlorout* corrosion additive [80]. The injected aqueous solution of ammonium sulfate dissociates into NH_3 and SO_3 in the following reaction:

$$(NH_4)_2SO_{4\,(aq)} \rightarrow 2NH_3(g) + SO_3(g) + H_2O_{(g)} \tag{3-1}$$

33
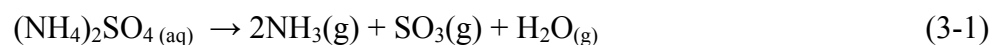
SO_3 reacts with alkali chlorides and converts them into alkali sulfates and HCl.

$$SO_{3(g)} + H_2O_{(g)} + 2KCl_{(g)} \rightarrow 2HCl_{(g)} + K_2SO_{4(s,g)} \tag{3-2}$$
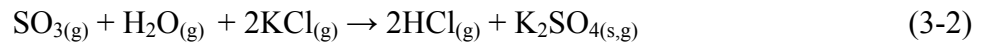
An example of the change in the deposition in the superheater is shown in the photographs of Figure 3-4 which show the same tube after 1000 hour exposure in a) without and b) with continuous injection of the Chlorout additive.

As noted above, the released ammonia contributes to the SNCR reaction in reaction 3 shown below.

$$4NH_3(g) + 4NO\ (g) + O_2(g) \rightarrow 4N_2(g) + 6H_2O\ _{(g)} \tag{3-3}$$
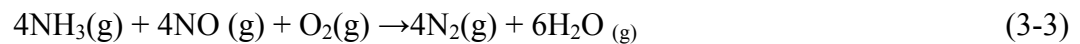
The Chlorout technology also includes a novel alkali chloride measuring technique, called IACM (In-situ Alkali Chloride Monitor), which measures the concentration of gaseous alkali chlorides (KCl and NaCl) on-line. The measurement principle is based on molecular absorption over a certain wavelength interval. IACM enables monitoring and control the incoming fuel mix as well as control of the required amount of the ChlorOut additive.

3.4.3 Sulfur recirculation

Gotaverken Miljo, a Babcock Wilcox affiliate in Sweden, also increased SO_2 concentrations in WTE boilers without combusting additional sulfur or adding sulfur compounds, by removing SO_2 in the second stage of the wet flue gas scrubbing system and recycling the captured sulfur compounds into the furnace via a patented "sulfur recirculation process." [81].
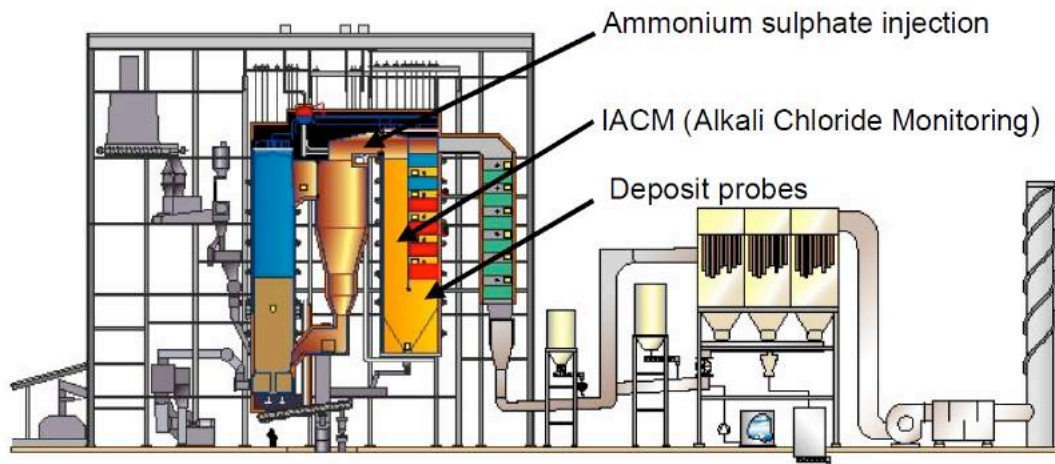
Figure 3-3. Vattenfall Chlorout concept [80].

Figure 3-4. Boiler tubes without and with Chlorout injection [80].

The second wet scrubbing stage (depicted as WS II in Figure 3-5) uses NaOH solution as the desulfurization agent. During preliminary testing, H_2O_2 was used to react with $SO_{2\,(g)}$ to form sulfuric acid

$$H_2O_{2\,(l)} + SO_{2\,(g)} \dashrightarrow H_2SO_{4\,(l)} \qquad (3\text{-}4)$$

The sulfuric acid produced in the scrubber was injected into the furnace through a tuyere with atomization air. In the furnace conditions, the sulfuric acid readily decomposes to SO_2:

$$H_2SO_{4\,(l)} \rightarrow H_2O_{\,(g)} + \tfrac{1}{2}\,O_{2\,(g)} + SO_{2\,(g)} \tag{3-5}$$
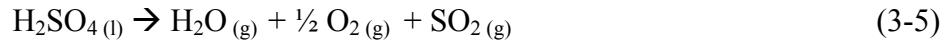
In this sulfur recirculation, the mean concentrations of sulfur in the flue gas were raised from 270 mg/Nm^3 to ~800 mg/Nm^3. In the sulfated ash environment, substantial reductions in tube wastage (between 60-80%) were observed after 1000 hours of field exposure for Inconel 625 (give composition same as Sanicro), Sanicro 28 (Fe-27 Cr-31 Ni), and 15 Mo (low alloy steel) at superheater tube metal temperature of 525 °C.
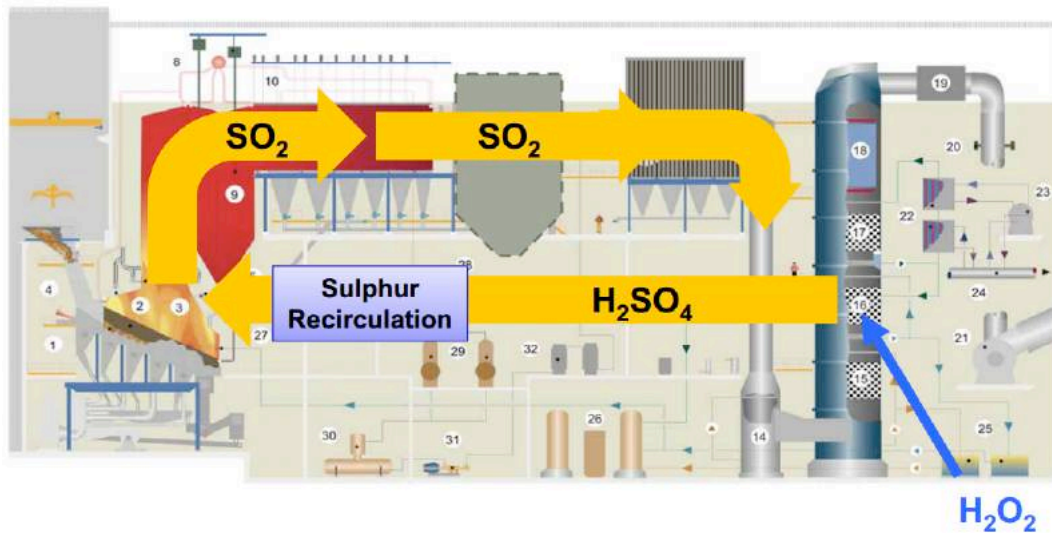
Figure 3-5. The Gotaverken Miljo sulfur recirculation concept [81].

3.5 Calcium hydroxide injection to removed HCl and SO₂

Injection of chemicals such as calcium hydroxide or magnesium hydroxide $Ca(OH)_2$ or $Mg(OH)_2$ into combustion furnaces has been proposed by the Earth Engineering Center of Columbia University and others as a means of sequestering HCl and decreasing its concentration

in the flue gas. This method is still under investigation, but preliminary results have shown it to be effective [82]. An example of a testing system which demonstrated the beneficial effect of this method is shown in Figure 3-6, adapted from the PhD thesis of Shang-Hsiu Lee.

The chemical reaction involved in the proposed process for chlorine sequestration is the same as that used in the semi-dry (or "dry") scrubber section of the Air Pollution Control in WTE power plants. In order to meet the MACT regulations, most WTE
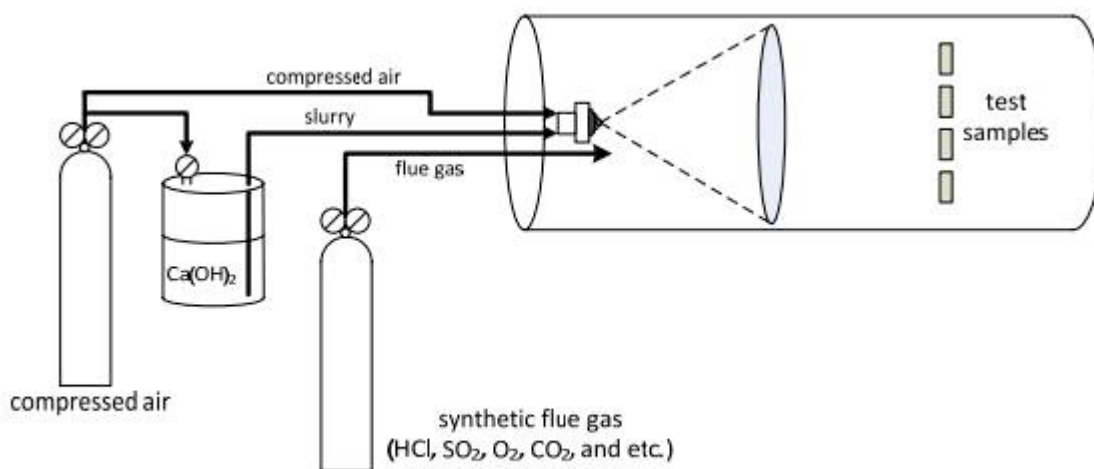
Figure 3-6. Schematic of corrosion test system for calcium hydroxide injection [82].

facilities, worldwide, have adopted the semi-dry scrubber system for acid gases and particulate emissions. In a semi-dry scrubber system, a finely atomized lime slurry of $Ca(OH)_2$ is injected in the scrubber through spray lance/nozzle assemblies to react with the acid gases and generate calcium sulfite/sulfate/chloride reaction products and has a removal efficiency of greater than 95% [82].

WTE power plants consume between 9.1 to 13.6 kg of lime (about 95% CaO) per ton of MSW processed [83]. The CaO is converted to $Ca(OH)_2$, yielding a concentration of about 10 wt.% Ca(OH)2. This slurry is then atomized into the scrubber system with dilution water. The

flowrate of the dilution water is controlled to maintain the desired outlet temperature of the scrubber system, which is typically about 150° C. Adding the dilution water just prior to the atomizers reduces the $Ca(OH)_2$ concentration to just a few percent. The proposed injecting location for the sequestration process is either at a level right above the combustion grate or in front of the superheater section [83].

3.6 Improvements to a cleaning system

Cleaning technologies are implemented to maintain the effectiveness of the surfaces and prevent pluggage of gas passes. Steam and air are the most commonly used media for this application. One disadvantage from sootblowing is that localized erosion and corrosion can occur in areas that are extraordinarily cleaned by the blowing medium. On remedy to that problem has been the installation of tube shields.

A mechanical rapping system can be used to complement sootblowing, to limit the number of cleaning cycles. In this system, a number of anvils strike pins to impart acceleration through the superheater tube assembly. The purpose is to remove the bulk of the ash while leaving a light layer so as to provide some protection to the tube [84].

Chapter 4: Experimental methods

4.1 Summary

In this chapter the details of a custom designed laboratory-scale corrosion apparatus and experiments are provided. The alloys investigated in this thesis were selected based on relevance to WTE boilers and through literature review and discussions with numerous companies in the WTE industry. Coupon test samples with dimensions of 2.5 cm x 1. 3 cm x 0.3 cm (0.5"x 1.0" x 0.3") were fabricated from select alloys provided by WTE vendors and operating companies An array of coupons were subjected to an environment replicating the flue-gas conditions typically present in WTE superheater ducts for approximately 24 hours. The corrosion that developed during the testing was quantified by determining the total mass loss from the coupon following the completion of the test according to an ASTM procedure for corrosion product removal. This procedure enabled the calculation of a corrosion rate that permitted extrapolation to anticipated wastage per year. In addition to the corrosion rate, several techniques were used to assess the physical and chemical changes in the samples, including: scanning electron microscopy (SEM); elemental dispersive spectroscopy (EDS); and X-ray diffraction (XRD)

4.2 Alloys

Three commercial steels and ten high temperature coatings were investigated in this thesis. The steels which were studied at length in chapters 5-7 are shown in table 4-1. Two of the alloys (SA 178A and SA 213 T22) have been widely utilized in WTE boilers and another (NSSER-4, Fe-17Cr-13Ni) has been considered for future use.

With the exception of NSSER-4, the test alloys were provided by plant operators in the form of tube section, like those shown in figure 4.1. The tubes were machined into test coupons. In addition to their industrial relevance, these particular alloys were chosen because of their contrasting metallurgical composition for a thorough understanding of the corrosion mechanisms at WTE superheater conditions.

Figure 4-1 Example of WTE superheater boiler tubes

SA213 T22 is used in commonly in superheaters either individually or with a coating [88]. SA 178A is a carbon steel that is more commonly utilized as a waterwall alloy [85] but is sometimes if metal protected by an overlay. Both alloys are considered a benchmark because it demonstrated poor corrosion resistance. (For the most of the analysis moving forward in this thesis, SA 213 T22 will be used as the benchmark). NSSER-4 is a stainless steel that has not been currently implemented into WTE power plants to date but was identified in previous experimental work as having favorable chloride corrosion resistance [86].

Additionally, six nickel coatings were investigated for this thesis and are discussed in chapter 6. They were comprised of 5 unique materials: Inconel 625, Colmonoy 88, SP 99, SW1600, and SW1641. The other coating was Colmonoy 88 applied by a laser weld, so that the performance of the application technology can also be compared. SP 99 has a very similar

Table 4-1. Elemental composition of investigated base metals [87-89]

Alloy	C	Cr	Ni	Mn	Fe	Mo	W
SA178 A*	0.07	0.02	0.05	0.47	bal	0.01	
SA213 T22	0.1	2.25			bal	1	
NSSER-4	0.04	17.3	13.1	0.8	bal		

SA178A also contains: Si 0.06, P 0.001, Nb 0.002, Cu 0.119, Al 0.026, Ca 0.001, N 0.08, Ti 0.003, and V 0.002

Table 4-2. Elemental composition of investigated protective coatings

Alloy	Process	Composition							
		Ni	Cr	C	B	Si	Mo	W	Fe
Inconel 625	laser	Balance	21.5	0.1			10		5.6
Colmonoy 88	HVOF	Balance	15	0.8				17.3	10.9
Colmonoy 88	laser	Balance	15	0.8				17.3	10.9
SP 99	laser	Balance	15		3	4	1.0	17.3	3.5
SW 1600	TS and IH	Balance	15		3.1	4.3	2.5		
SW 1641	TS and IH	Balance	37.1		3.6	3.4	3		
Substrate		Composition							
		Ni	Cr	C	B	Si	Mo	W	Fe
SA213 T22			2.25	0.1			1		Balance

Process: HVOF = high velocity oxygen fuel coating; TS: thermal spray; IH: induction heating

composition to colmonoy, with the addition of 1 wt% Molybdenum. SW1600 and SW1641 belong to a group of NiCrMoBSi alloys. The thickness of each coating was between 1500-2000 microns (1.5-2.0 mm) and was applied to the same substrate material SA 213 T22.

4.3 Coupon preparation

The coupons were fabricated in the Combustion and Catalysis Lab (CCL) either using a water cooled saw or a cut-off (chop) saw equipped with an alumina-silicon carbide blade. The typical coupon dimensions are 2.5 cm x 1. 3 cm x 0.3 cm (0.5"x 1.0" x 0.3") allowing placement of multiple samples in the corrosion test rig that is described in more detail in section 4.4. The sample coupons were prepared for testing following the ASTM G1-03 procedure for corrosion testing. This includes imprinting the designation code into the sample surface for clear identification post-test; grinding the sample edges and faces using a 120-grit surface; degreasing with an organic solvent (reagent grade acetone) in ultrasonic baths; and drying in air at 100°C for one hour. After preparation, the clean, dry sample was weighed in a Mettler Toledo Analytical balance (XS64), with readability to ± 0.1 mg.

4.4 Corrosion Test Rig

A schematic of the experimental setup is shown in Figure 4-2 and a photo of the actual corrosion test rig is shown in Figure 4-3. Testing was performed in a sealed, single zone tube furnace (Lindberg 55035) in a 25 mm (~1") ID quartz tube. The test coupons were placed on a 316L stainless steel plate (8" x 0.75") to prevent corrosion of the base metal. This technique ensured that the corrosion observed occurred only on the exposed surface containing the metal or alloy of interest. The furnace was operated by PID temperature controllers (Omega Engineering, Inc CN 7800) connected to a K-type thermocouple (Omega Engineering, Inc., KQXL-116U-18) which provided temperature resolution of ± 0.1C.
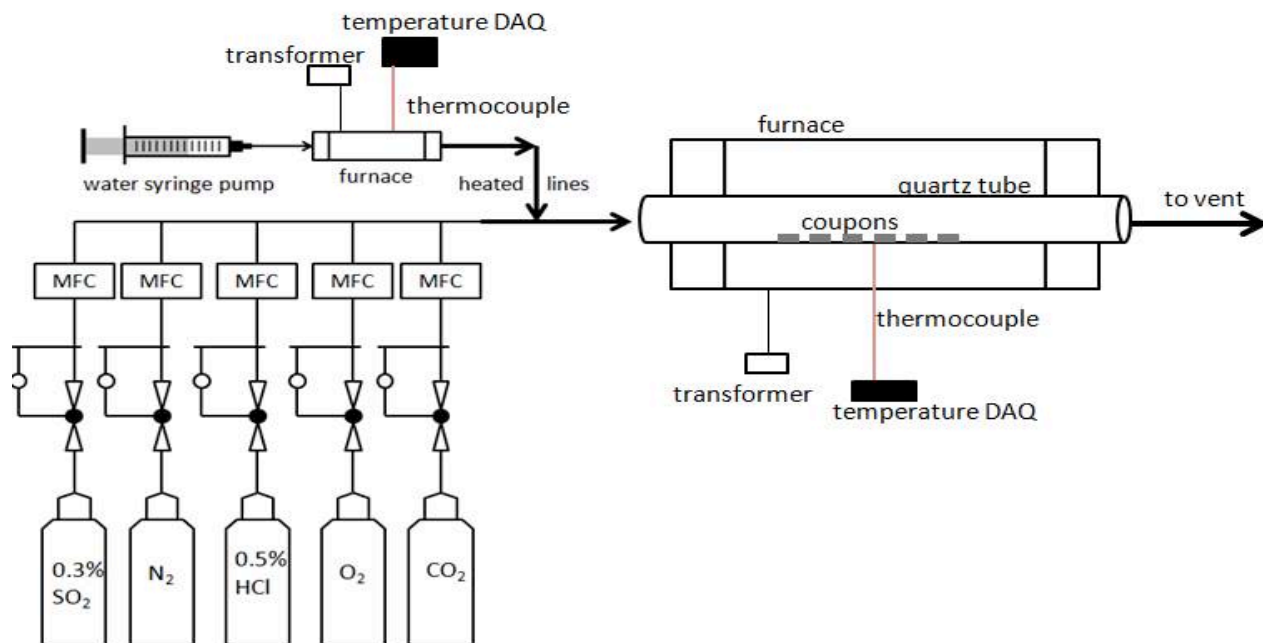
Figure 4-2 Schematic of corrosion test rig.

Figure 4-3 Photograph of corrosion test rig

The gas delivery section shown in Figure 4-2 is represented via cylinder outlines connected to mass flow controllers (MFC). This permitted the use of pure gases that were independently controlled to yield a desired mixture. The gases were procured from Tech Air Inc. and were certified ultra-high-purity grade. The gaseous environment introduced into the furnace was intended to replicate a WTE flue gas mixture. Incorporating suggestions from WTE engineers, the base composition of the WTE flue gas mixture consisted of 8% O_2, 12% CO_2, 800 ppmv HCl, 100 ppmv SO_2, 15% water vapor, with a balance of N_2. For each experiment, the total gas flow rate was constant at 500 mL/min. Upon exiting the furnace, the gas mixture was vented into a fume hood. Given the corrosive nature of the gases used in this experiment and the health risks associated with short-term exposure to SO_2 and HCl [91,92], proper personal protective equipment and protocols were followed.

One of the advantages of using pure gases and concentrated mixtures is to enable an understanding of the effects of varying one gas species against another. In particular, the effect of varying SO_2 and HCl are of great interest to WTE operators because they have been identified as major contributors to hot corrosion events. As such concentrated gas cylinders containing 5000 ppmv HCl in nitrogen and 3000 ppmv of SO_2 in nitrogen were used to vary the HCl and SO_2 concentration within controllable flowrates allowing precise ratios to be established. Additionally, a total flowrate of 500 mL/min was maintained in each experiment by modifying the nitrogen balance. Flowrates were controlled via mass flow controllers (Aalborg Instruments and Controls, Inc., SKUW-183356). The synthetic flue gas mixture was preheated prior to entering the furnace to 350° C $\pm$ 20°C using electrical resistive heating elements (Omega Engineering, Inc., FGS101-060) wrapped securely around the inlet transfer line as shown in Figure 4.2 and controlled by variable transformers (Stacco 1050 B).

Water vapor was introduced into the test rig by vaporizing deionized water (conductivity ≤ 1.5 μS/cm) in a separate furnace upstream of the heated inlet transfer tubing. The water flow rate was controlled via a microsyringe pump (New Era-1000). The steam furnace was controlled via a variable transformer with the temperature monitored by a k-type thermocouple. Temperature data was recorded by wiring the thermocouple and temperature controllers to a data acquisition board (Omega Engineering, Inc. OMB-DAQ-55) providing continuous readings.

Figure 4-4 shows a temperature profile generated for the test furnace at a desired setpoint of 500°C. The temperature measured is within 2°C of the setpoint over a large portion of the heated zone of the furnace, exceeding six inches in the length. Since the test coupons are 1.0 inch in length, it was determined that six coupons can be tested per experiment experiencing a uniform temperature field. The temperatures used in the isothermal experiments correspond with the metal temperatures typically measured in WTE superheater tubes. A discussion comparing the effects of a thermal gradient corrosion test with an isothermal test is provided in chapter 5.

4.5 Salt Layer Application

In addition to the gas environment, the effects of chloride and sulfate salts were also examined. As discussed in Chapters 2 and 3, some of the most common deposits found on superheater tubes during shutdown consist of alkali chlorides and alkali sulfates. Discussions and literature survey resulted in the use of sodium chloride and sodium sulfate being selected for this study as the surrogate species to probe the effect of chloride and sulfate deposits.
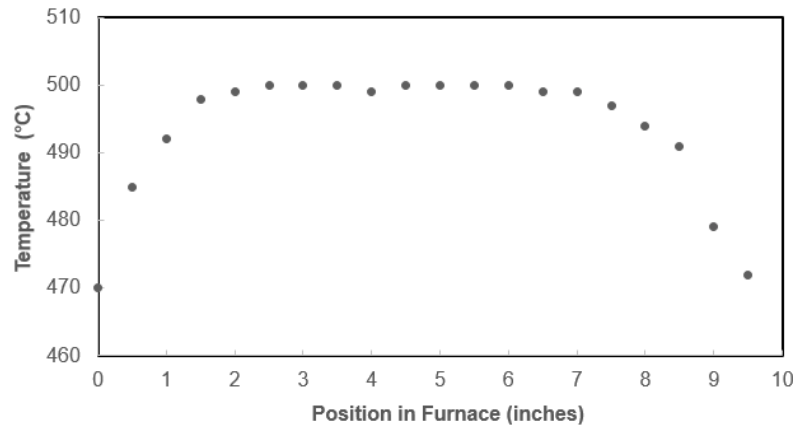
Figure 4-4. Temperature profile of electric furnace at set point of 500°C with 500 mL/min flow of nitrogen

Salt layers were applied to coupons via successive wetting and drying in accordance with previous designed protocols for hot corrosion testing [90]. An aqueous solution of 100 grams per liter NaCl or 50 grams per liter Na_2SO_4 was applied to one side of the ASTM prepared surface of the test coupon via a micropipette and dried in an air environment at 120-130°C. The application of the salt layer was adjusted so that a loading of 4.0 ± 0.1 mg salt/cm^2 coupon area was used in each experiment and is further detailed in Chapter 5.

4.6 Quantifying extent of corrosion

After each corrosion experiment, the samples were left to cool in the furnace under nitrogen flow- to limit spallation of the corrosion product as much as possible. The coupons are then characterized using the techniques discussed in section 4.7 which then enables the extent of corrosion to be quantified.

Uniform corrosion rates are represented as a loss of metal thickness as a function of time. This value can be directly measured from experimental data, or as is often the case, it can be calculated from mass loss data. The mass loss is defined as the difference between the original mass of the specimen (i.e. the sample weight after the ASTM preparation procedure) and the mass of the specimen after exposure and after following the removal of the corrosion product.

The corrosion product removal is performed following the same ASTM G1-03 method discussed before for preparing the corrosion samples. The corrosion product removal uses mechanical and chemical processes. Mechanical cleaning includes scrapping, scrubbing with a non-metallic bristle brush, and possibly placing the coupons in an ultrasonic cleaner depending on the type of corrosion product and the adhesion to the specimen. Throughout the testing it was observed that mechanical cleaning was not sufficient to remove all of the developed corrosion product post-testing. This necessitated the use of an additional chemical cleaning step.

In the ASTM procedure, there are multiple cleaning procedures for each type of alloy. The choice of which procedures to follow is partly a matter of trial and error. The chemical cleaning is typically accompanied with mechanical cleaning (brushing or placing in an ultrasonicator bath). Cleaning may require multiple cycles until a constant weight is obtained. The chemical procedure involves immersion of the corrosion test specimen in a specific solution that is designed to remove the corrosion products with minimal dissolution of underlying metal that was not corroded during the test. The following steps are the generally accepted chemical procedures that were adopted for the alloys tested in this thesis [91].

It is critical to address however, that this procedure should remove only the corrosion products and not result in the removal of a base metal. To determine the mass loss of the base

metal, the cleaning procedure should be replicated on an control specimen. If there is a mass loss associated with the method chosen, and it is reliable, that value should be corrected when assessing the mass loss. Typically when applying the chemical procedure, at most 0.5 mg mass was corrected from the virgin metal loss- which were the case for low alloy steels and the zinc and sodium hydroxide cleaning at 80° C.

It also should be noted that if the primary type of corrosion is pitting, a mass loss measurement is generally not a good indication of the extent of pitting- unless there is also uniform corrosion and the ratio of pitting corrosion to uniform corrosion is small. To evaluate pitting corrosion, another ASTM procedure [92] is recommended, and the pitting can be further quantified by microscopy techniques. In either case however, reporting the mass change per specimen area (e.g. mg/cm^2) is acceptable.

Once the final (and corrected) mass loss is obtained, the mean corrosion rate may then be obtained by applying the following equation:

$$\text{Corrosion rate} = [K * w] / [A * t * \rho] \qquad (4\text{-}1)$$

where t = exposure time (in hours), A is the area of the coupon (cm^2), ρ is the alloy density (in g/cm^3), and w is the mass loss (in milligrams or grams). The densities of the investigated alloy, assembled from various sources are shown in table 4-3. The rate constant, K, is a constant which can be changed depending on what values are of interest, typically either penetration (mm/mil/μm) per time unit. The mass loss per unit area per unit time can also be acceptable.

Table 4-3. Densities of alloys [93-94]

Alloy	Density (g/cm3)
Base metals	
SA 178A	7.86
SA 213 T22	7.85
NSSER-4	7.98
Protective Coatings	
Inconel 625	8.44
Colmonoy 88 (HVOF)	9.89
Colmonoy 88 (laser)	9.89
SP 99	9.89
SW1600	7.73
SW1641	6.31

4.7 Characterization techniques

In addition to determining the mass loss and the corrosion rate, there are a variety of analytical techniques which have been used to identify the chemical and physical changes within a sample. This section provides a brief description of each of the various analytical techniques used in the discussion of this thesis.

4.7.1 Scanning electron microscopy (SEM)

Scanning electron microscopy (SEM) is utilized for surface and cross section imaging. It is a widely used technique to identify physical changes occurring at the microscale level. SEM operates by scanning a sample surface with a beam of electrons, which are generated by an electron gun and focused with magnetic lenses down to a diameter of about 0.01 nm. The electrons interact with atoms at the surface of the sample, leading to emission of new electrons. The emitted electrons are then collected and counted with a detector. Some SEM units have

included two different modes: either detecting secondary electron emission or backscattered electron emission [95]. Both modes provide distinct advantages to the user. The secondary electrons are generated either by the primary beam or any scattered electron that passes near the sample surface. They are emitted after several collisions with most of their energy emerging from the sample surface [96]. As a result, secondary electrons generate high resolution images. Backscattered electrons are reflected back with minimum amount of collisions with surface atoms. However, in a single collision with atoms of different atomic weights, the loss of energy will be different and backscattered electrons will have different energies. So this mode provides images that give a contrast between different elements, in particular for heavier elements [97].

The SEM used mostly in this thesis work is the Hitachi TM-3000, a tabletop unit, shown in Figure 4-5. The Hitachi TM 3000 has an operating voltage of either 5 or 15 kV with magnification up between 15X- 30,000 X and is equipped with back scattered detector.

4.7.2 Energy dispersive spectroscopy (EDS)

SEM can be combined with a number of different techniques for chemical analysis, the most common being energy dispersive spectroscopy (EDS). This allows for an elemental footprint for most of the elements present on the surface of a sample or the surface of a sample's cross section. When the electron beam from the SEM interacts with the surface, X-ray photons

Figure 4-5. Hitachi TM 3000 scanning electron microscope

are generated and radiated. The energy of the radiating photons corresponds to a transition energy which is characteristic for each element ($K\alpha$, $K\beta$, $L\alpha$, $L\beta$ lines). These X-rays are then passed to a semiconductor detector which converts the X-rays of the various elements into electrical signals which are then passed to a multichannel analyzer that separates the various elements into different channels depending on energy.

There are limitations to EDS, most notably it only has a detection limit of elements that are 0.1 wt% or greater [104]. Therefore, the technique is often considered semi-quantitative. Nevertheless it can be useful to provide trends and ratios among major species. The EDS accompanied with the Hitachi TM 3000 is the Bruker Quantax 50.

4.7.3 X-Ray Diffraction

Crystalline salts (e.g. NaCl and Na_2SO_4) and other corrosion products are analyzed by powder X-ray diffraction. Identifying these compounds is very useful in ascertaining reaction mechanisms.

The X-ray source consists of a tungsten filament cathode which generates electrons when heated. When the electron beam impacts the anode, it gives rise to x-rays which are monochromatic before reaching the specimen. The atoms in a crystal are a periodic array of coherent scattering centers and thus can diffract light. The interaction of X-rays with a powdered sample creates secondary "diffracted" beams of X-rays related to interplanar spacings (d) in the crystalline powder according to Bragg's law, $n\lambda = 2d \sin\theta$, where n is an integer, λ is the wavelength of the X-rays, d is the interplanar spacing generating the diffraction, and θ is the diffraction angle [98].

In this work a powder XRD (X'Pert MRD) was used with CuKα-radiation (λ=1.54178 Å) source. The X'Pert software, HighScore Plus, contains a variety of databases for diffraction patterns, most notably from NIST (National Institute of Standards and Technology). This database was used to identify the compounds obtained in the diffraction patterns. A picture of the X'Pert MRD powder diffraction unit is shown in Figure 4-6.

Figure 4-6. X'Pert X-ray Diffractometer

4.8 Research Objectives

4.8.1 Problem statement

The ultimate objective of this research is to propose solutions which can allow waste-to-energy power plants to operate boilers for longer periods of time without corrosion related shutdowns and operate at superheater steam temperatures of 500°C and higher. This is accomplished by providing a scientific understanding of surface reactions related to chloride corrosion and the impact of variables such as temperature; alloying composition, salt deposit, and SO_2/HCl flue gas ratio.

4.8.2 Scientific and engineering questions

The scientific and engineering questions to be addressed by this research are:

(1) What are the likely mechanisms of high temperature corrosion of boiler alloys in the presence of WTE flue gas? Under chloride salt deposits?

(2) What is the relationship between temperatures on corrosion under chloride deposits?

(3) What types of alloys are most suitable for corrosion resistance under aggressive WTE superheater conditions?

(4) What is the relationship of SO_2/HCl to the high temperature corrosion of alloys?

(5) What are the recommendations that can be given to the WTE Industry in order to mitigate corrosion?

Chapter 5: Parametric studies on hydrogen chloride corrosion

5.1 Summary

The following is an experimental investigation into the effects of hydrogen chloride gas on the high temperature corrosion of steels at superheater boiler tube temperatures (450-550°). The experiments focused on two common boiler tube alloys: carbon steel SA178A (Fe-0.1C), low alloy steel SA213 T22 (Fe-2.25 Cr- 1.0 Mo) and a promising material for WTE boiler tubes, NSSER-4 (Fe-17Cr-13 Ni).

In an oxidizing environment at high temperature, the presence of hydrogen chloride gas, accelerates the corrosion steels. The parabolic rate constant of SA178A increase from 0.17 to 1.8 $\mu m^2/h$ with the addition of 800 ppmv of hydrogen chloride to the synthetic flue gas. The acceleration was inferred to be caused by the active oxidation as shown through physical observations, corrosion product layer characterization (XRD, EDS) and thermodynamic calculations. Activate oxidation can be mitigated with alloying additions of chromium and nickel, as demonstrated with experiment using NSSER-4 (Fe-17Cr-13Ni). The austenitic steel had nearly half (53 kJ/mol) the apparent activation energy of the carbon and low alloyed steel respectively (110-111 kJ/mol).

In the remainder of the chapter some additional parameters were investigated on the HCl corrosion behavior. It was determined that concentration of hydrogen chloride in the flue gas had a significant difference in the thickness of scale formed on SA178A a between 0 and 400 ppmv at 500 °C and a moderate effect between 400-800 ppmv. Studies investigating the impact of a

thermal gradient on SA178A also showed that the corrosion rate had a minimal change in mass change in a gas-metal temperature gradient of 260°C as compared to isothermal environment.

5.2 Introduction

The average mass percentage of chlorine in MSW is compared to other solid fuel sources in table 5-1. Several biomass and coal types are listed to demonstrate the variability. MSW has a narrower chlorine range between and with the exception of a few sources (e.g. Illinois River Basin coal, switchgrass) have significantly higher chlorine content. In chapter 1, table 1-1, it was shown that the chlorine content in MSW is contributed from various waste streams including plastics (0.26 wt%), biomass (0.34 wt%), textiles (0.55 wt%) and paper and paperboard (0.06 wt%). Thus, the presence of chloride compounds cannot be avoided in WTE power plants without drastically modifying the fuel composition and plant operation.

Table 5-1. Chlorine content of various solid fuels [99-100]

Fuel	Subcategory	Percent Chlorine (Weight %)
Biomass	bark, coniferous trees	0.02
	straw	0.18
	switchgrass	0.79
	yard wastes	0.11
Coal	Appalachian coal	0.1
	Illinois Basin coal	0.32
	Pacific River Basin coal	0.01
MSW		0.47-0.72

Chlorinated compounds in MSW are converted to hydrogen chloride gas (HCl) in the combustion environment. Hydrogen chloride may form chlorine gas, Cl_2, in oxidizing environment. Below 600°C, chloride gas Cl_2 is the thermodynamically favored species [101]. In addition to HCl and Cl_2, metal chlorides are also present in the form of vapor or condensed species. It has been suggested in literature that these species form as a result hydrogen chloride reacting with the inorganic fraction of MSW [110]. Two examples of common metal chlorides, sodium and zinc, and their formation reactions are shown in equations 5-1 and 5-2 below.

$$Na_2O_{(s,g)} + 2HCl_{(g)} \rightarrow 2NaCl_{(s,g)} + H_2O_{(g)} \tag{5-1}$$

$$ZnO_{(s,g)} + 2HCl_{(g)} \rightarrow ZnCl_{2(s,g)} + H_2O_{(g)} \tag{5-2}$$
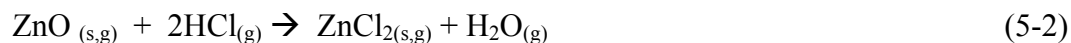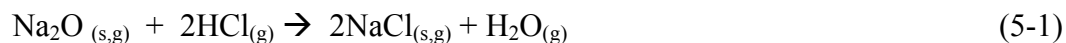
The complexity of corrosion environment in WTE boilers is increased by the participation of the different types of chloride compounds.

The experimental investigation in chapters 5, 6 and 7, is intended to provide an understanding on the corrosion phenomena by identifying the effects of individual parameters on high temperature corrosion. Chapter 5 mostly focuses on the behavior of hydrogen chloride while chapter 6 focuses on the effect of metal chlorides- using sodium chloride as a surrogate compound. Chapter 7 in part investigates the behavior of both chlorine compounds under the influence of changes in the flue gas environment-specifically due to sulfur.

5.3 The effect of hydrogen chloride

The effect of hydrogen chloride on high temperature corrosion was observed by exposing coupons of SA178A carbon steel in an electric furnace over various exposure times at 500°C. In one set of experiments the coupons were subject to a representative WTE flue gas mixture, consisting of 15% H_2O, 12% CO_2, 8% O_2, 100 ppmv SO_2, and 800 ppmv HCl and N_2 balance for a total flow rate of 500 milliliters per minute. In the second set of experiments, hydrogen chloride was removed from the gas mixture and nitrogen was added to keep the total flowrate in both test conditions constant. The coupons were recovered from the furnace after 12, 24, 50, and 72 hours respectively.

Figure 5-1 shows the average mass loss obtained from the coupons of SA178A under the two gas environments. The mass loss is obtained by removing the corrosion product from the coupon surface, following the method specified in ASTM G1-03 discussed in chapter 4. The values in the figure are normalized over the specimen area (mg/cm^2) to account for small changes in the coupon area (typically 3.45 cm^2) and represent the average of six coupons.

The profile of the mass loss versus time shows largely different behavior between the two gas environments. The profile of the gas environment containing 800 ppm HCl has steeper increase at 12 hours and appears to follow a parabolic trend up to 72 hours. The profile of the gas environment containing 0 ppm HCl has more moderate increase and appears to plateau after 24 hours. The values from figure 5-1 can be used to determine the kinetic behavior of the high temperature corrosion of SA178A under the two different corrosive environments. As discussed in chapter 2, high temperature corrosion typically follows a parabolic rate law. This can be determined by plotting square of the weight change over time, and determining whether the best

fit is linear. Both the 800 ppm HCl and 0 ppm HCl exhibited a linear profile with the square of the weight over time. Based on the data it can be concluded that the corrosion under these two environments follow a parabolic rate law. The slope of the plot of the weight squared per time is the parabolic rate constant and is reported in Table 5-2. Additionally, the units are expressed in thickness squared over time. Based on these results, the corrosion rate of SA178A is 11 times greater at 500°C under the 800 ppm HCl environment than the 0 ppm HCl environment.
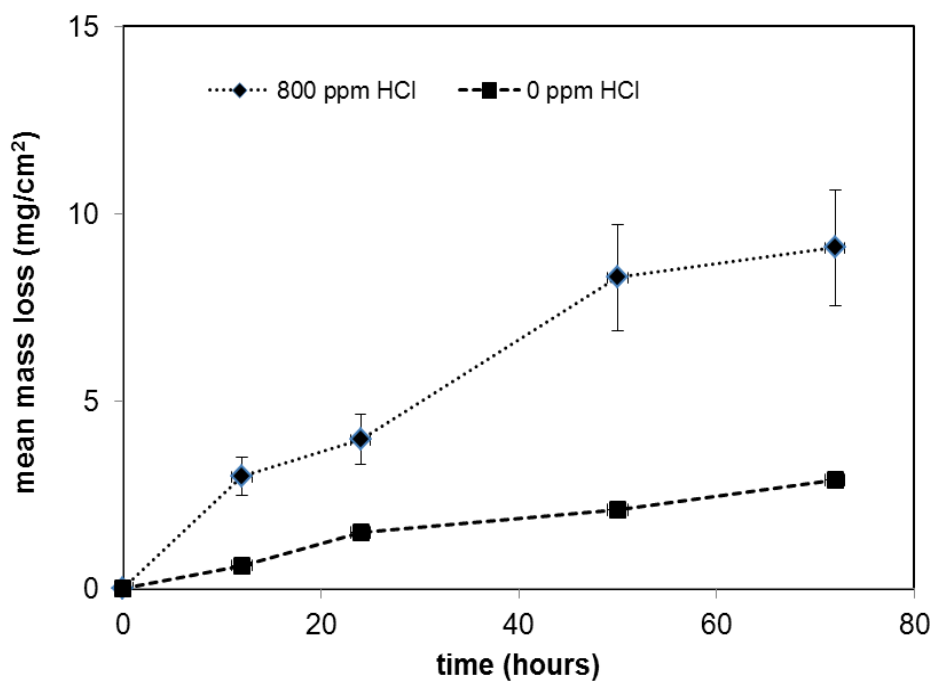
Figure 5-1. Mean mass loss of SA178A versus time (0-72 h) at 500°C under two synthetic flue gas environments (0 ppmv HCl and 800 ppmv HCl)

.

While the corrosion rate is evaluated by determining the total mass removed (intended to be the total corrosion product), it is worth noting that the mass losses are evaluated in two stages which can provide additional insight on the corrosion behavior. First, the corrosion product is lightly scraped and/or brushed to remove scales or powder from the coupon surface. Secondly, the coupons are subjected to chemical cleaning, whereby the corrosion products are dissolved with minimal loss of the base metal.

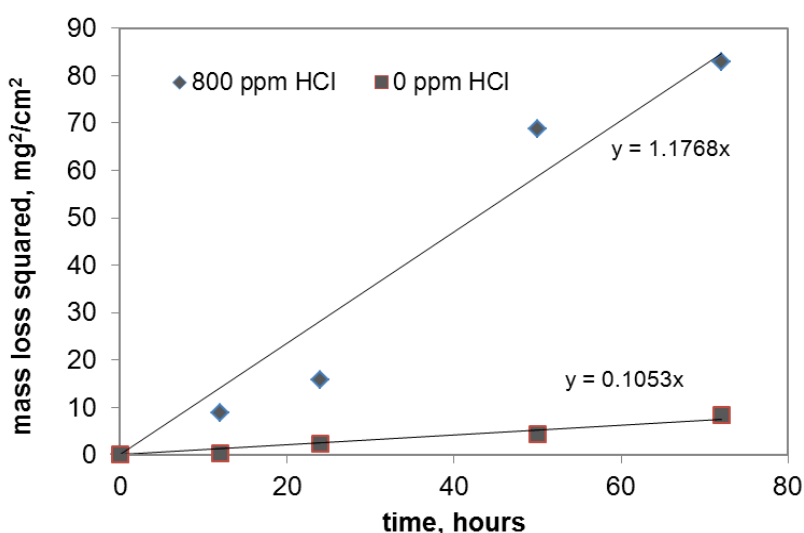**Figure 5-2.** Square of mass loss of SA178A versus time under two synthetic flue gas environments (0 ppmv HCl and 800 ppmv HCl

Table 5-2. Rate constants for SA178A, 500°C (932°F) under corrosive gas mixtures

Test Environment	Parabolic rate constant, 500°C		
	mg^2/cm^2-h	$\mu m^2/h$	mil^2/h
0 ppmv HCl	0.11	0.18	3.0E-04
800 ppmv HCl	1.18	1.7	2.5E-03

59

An example of this mass loss breakdown is shown in table 5-3. The mass loss of SA178A under a WTE mix with 0 ppm HCl after 72 hours has nearly the same overall mass loss (i.e. corrosion layer thickness) as SA178A coupon at 12 hours under 800 ppm HCl. Yet in obtaining the same overall mass loss, the mass loss contributions are significantly different. The coupon under the HCl environment has lost a significant mass due to mechanical cleaning, whereas the coupon under 72 h in a HCl absent environment, required chemical dissolution of the corrosion product.

It can be inferred that a higher a chemical removal suggests a more adherent corrosion product. Thus, the corrosion layer in absence of HCl forms a more adherent corrosion layer to the carbon steel coupons. Figure 5-3 demonstrates this behavior by comparing SA178A coupons after 50 hour experiments. The coupon under the HCl environment appears to have cracks and has already lost mass during the process of cooling down from test temperature to room temperature.

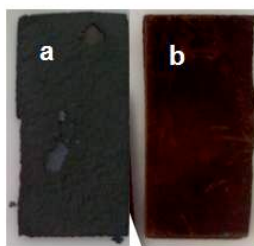
Figure 5-3. Images of SA178A coupons following (a) 50 hours under 800 ppmv HCl and (b) 50 hours under 0 ppmv HCl gas mix

In general, coupons that have a thicker corrosion layer are more susceptible to having a layer peel or scrap off the coupon during temperature fluctuation or when a test specimen is cooled down to room temperature. This behavior is known as spallation. There are various

Table 5-3. Mass change comparison for three test conditions for SA178A at 500°C

Test condition	Total mass loss (mg/cm²)	Spallation & mechanical removal (mg/cm²)	Chemical removal (mg/cm²)
0 ppm HCl, 72 h	2.1	1.7	0.4
800 ppm HCl, 12 h	2.0	0.2	1.8
800 ppm HCl, 50 h	8.4	5.7	2.7

factors which can cause spallation including epitaxial stress, the mode of the diffusing species, and the difference in thermal expansion coefficients between the corrosion layer and the alloy or the types of oxide formed in the corrosion products [102].

The tendency for certain oxides to promote spallation can be predicted using the Pilling Bedworth ratio (PBR)- which is defined as the ratio of the molar volume of the metal oxide to the molar volume of the metal substrate. Equation 5-3 shows the expression of PBR where M stands for the atomic or molar mass, ρ is the species density and n is the atoms of metal per mole of oxide. If there is a large difference in the volume of the oxide versus the metal the oxide is more likely to spall. Therefore, ratios much less than or greater than 1 would be candidates for spallation.

$$PBR = V_{oxide} / V_{metal} = M_{oxide} * \rho_{metal} / n * M_{metal} * \rho_{oxide} \qquad (5\text{-}3)$$

Thermodynamic calculations indicate that Fe_2O_3 and Fe_3O_4 are the predominant corrosion products for high temperature corrosion of SA178A (99 wt% Fe), except at the metal-oxide interface where the partial pressure of oxygen may be $<10^{-10}$ bar, at which iron (II) chloride would be able to form. This is shown in a Fe-O-Cl predominance diagram at the test temperature

of 500°C, which considers the thermodynamic equilibrium between the potential iron oxides and chlorides as well as iron at a fixed temperature. The Fe-O-Cl diagram at 500°C was provided in figure 2-3 and is displayed again below.

Applying this understanding, the PBR calculated for compounds Fe_2O_3 and Fe_3O_4 on Fe was determined to be 1.02 and 1.2 respectively. As these values are approximately close to 1, they are typically considered an adherent oxide. Therefore in the case of SA178A and comparing the test conditions, PBR is not a good marker for explaining spallation of SA178A coupons. Thus, other phenomena should be considered.
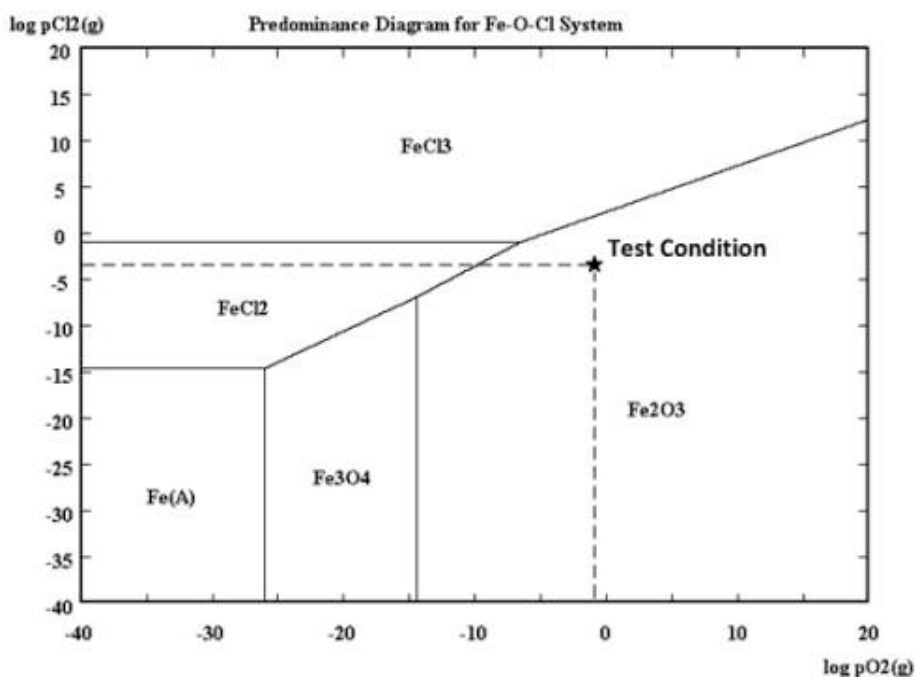

Figure 2-3. Predominance Diagram of Fe-O-Cl system at 500°C

Figures 5-4 and figures 5-5 show the XRD pattern for the scales recovered from SA178A coupons 500° C under the flue gas environments with and without hydrogen chloride. The patterns for the scale are shown on top in red, followed by the peaks of standard compounds

(ICDD software, X'Pert instrument software) in blue below. Both scales were identified to include two types of iron oxides, maghemite and magnetite. This is in agreement with the thermodynamic calculation previously discussed. Additionally, the patterns did not reveal other compounds which would be able to explain why the corrosion product under the HCl containing flue gas was nearly 2.5 times larger in mass.

Figure 5-4. XRD pattern of scale recovered from SA178A coupon at 500°C under flue gas containing 0 ppm HCl (with patterns of highest matched compounds)

Additionally, elemental dispersive x-ray spectroscopy (EDS) spot analysis was performed on two SA178A coupons in the HCl containing environment was performed above and below the spalled corrosion product. An average of 3-spots was taken for both coupons and the results which are shown in Table 5-2. While there is a small detection of sulfur below the corrosion layer, chlorine was not detected. Chlorides were therefore not detected in the corrosion layer surface neither in the scale analysis, nor below. It should be noted however, that the
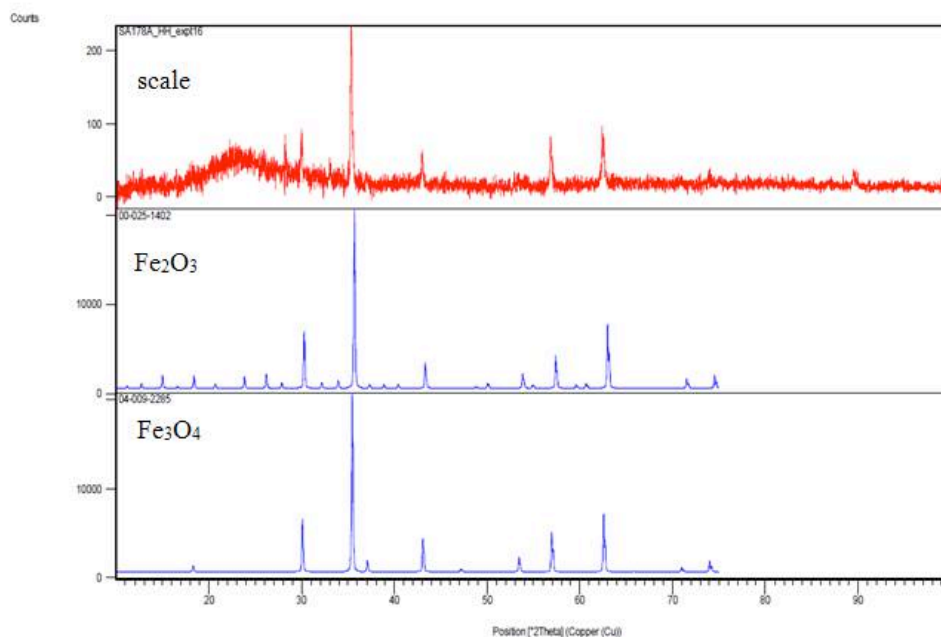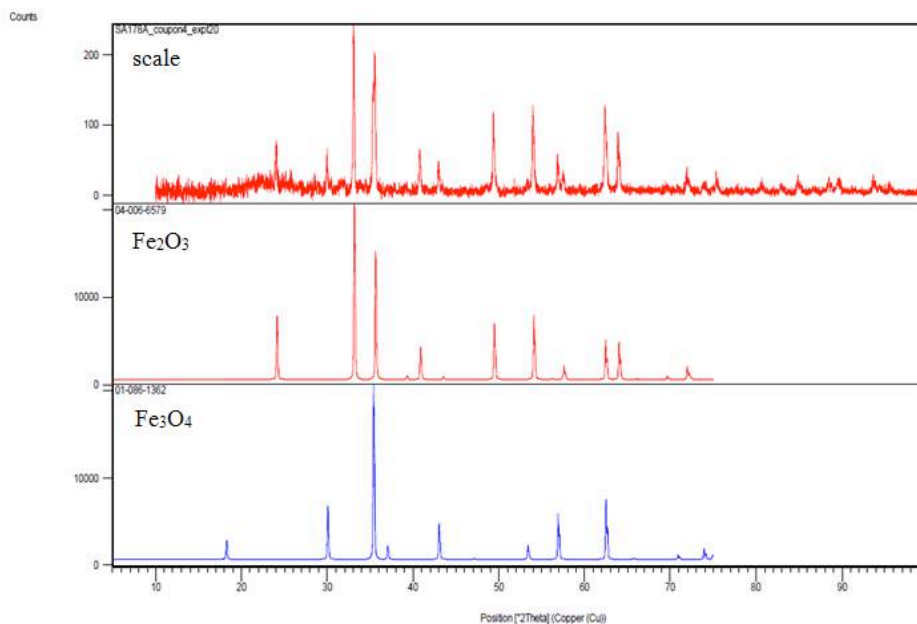
Figure 5-5. XRD pattern of scale recovered from SA178A coupon at 500°C under flue gas with 800 ppmv HCl (with patterns of highest matched compounds)

analysis provide in Table 5-4 is qualitative in that the corrosion layer removal depends on the layer adherence. This does not conclusively eliminate the presence of chlorine or other elements. The oxide layer, as demonstrated in Table 5-3 is not fully recoverable without the use of a chemical solvent or a polishing method (the latter case would likely remove virgin material).

Table 5-4. EDS Analysis of SA178A corrosion layer and below layer
(Values are normalized wt%)

Element	Below Corrosion Layer (wt%)	Corrosion Layer (wt%)
Iron	86	62
Oxygen	13.9	38
Sulfur	0.1	0
Chlorine	0	0

This analysis would be further supported by performing a cross-section SEM-EDS analysis. Other papers have performed this type of study in the past and were able to identify the presence of chlorine below the scale at the interface of the virgin metal [103]. Nevertheless, the results above are in agreement with the literature that the addition of hydrogen chloride engages in the active oxidation mechanism.

5.3.1 Effect of hydrogen chloride concentration on corrosion rate

The effect of the hydrogen chloride concentration was investigated at 0, 400 and 800 ppmv and is shown in figure 5-6. Like the experiments discussed in figure 5-1, the HCl concentration was modified and replaced with nitrogen to maintain the same the total gas flowrate. The mass losses were obtained following 24 hour exposure at 500°C. The error bars represent the standard deviation from the mean of the mass loss obtained from the sample coupons.
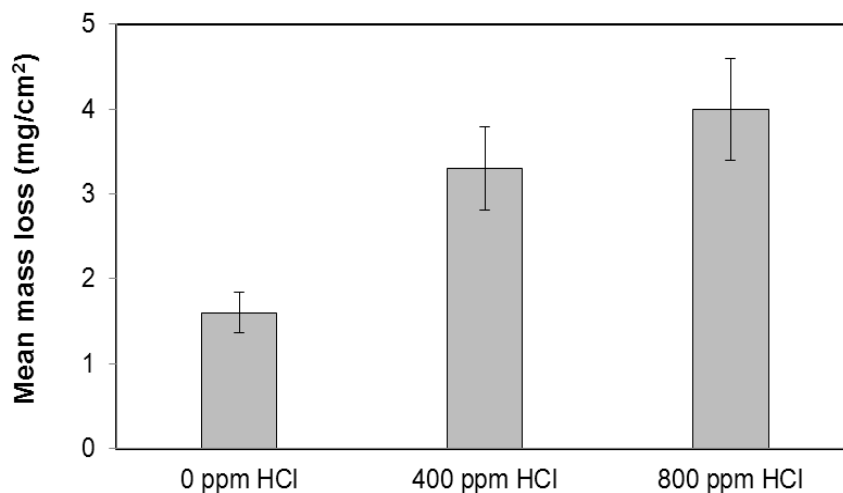

Figure 5-6. Mean mass loss of SA178A after 24 hours at 500°C under flue gas mixtures with 0,400, and 800 ppmv HCl

There is a significant increase between 0 and 400 ppmv HCl, as the value of the average mass loss is doubled from 1.6 to 3.3 mg/cm^2. The average value obtained at 800 ppmv had a marginally higher loss at 4 mg/cm^2. These values, the average of 6 coupons per experiment, had a variation of 0.4-0.6 mg/cm^2, which is demonstrated with the error bars.

The effect of corrosion due to hydrogen chloride is consistent with findings from other authors which investigated the hydrogen chloride effect at 500 ppm and 1000 ppm on alloys between 500-600 °C respectively [104] under a similar WTE flue gas environment. In that study, the corrosion rate of SA178A was elevated by 70% between 0 ppm HCl and 500 ppm HCl and elevation by only 7% between 500 ppmv and 1000 ppmv [114]. This is compared to the data in figure 5-6 which shows a 106% elevation between 0 ppm and 400 ppm HCl and a 20% increase between 400 ppm and 800 ppm. This behavior suggests that there is a possible diffusion limitation above 500 ppm HCl.

5.4 Comparison of alloy behavior

Figure 5-7 shows the mass loss of SA178A, SA213 T22 (Fe-2.25Cr-1Mo) and NSSER-4 (Fe-17Cr-13Ni) under a constant gas environment containing 800 ppm HCl at 450, 500, and 500°C respectively after 24 hours 500°C respectively after 24 hours. The mass loss of the carbon and low-alloyed steel was approximately an order of magnitude greater than the stainless steel, 0.25 mg/cm^2 at 500°C compared with 3.6 mg/cm^2 and 3.9 mg/cm^2 for T22 and SA178A. An image of NSSER-4 coupon vs. the SA213 T22 coupons (figure 5-8) demonstrates the stark contrast between the two corrosion products.

The NSSER-4 corrosion product is a thin film, and only required chemical cleaning in order to determine the total mass loss, whereas the SA 213 T22 exhibited mass loss distribution to SA178A between spallation and mechanical removal to chemical removal. The corrosion resistance of NSSER-4 (Fe-17Cr-13Ni) is consistent with the active oxidation mechanism. The formation of metal chlorides is considered a paramount part of the corrosion process [105] Considering the equilibrium $FeCl_2(s) = FeCl_2(g)$, which would the single type of metal chloride formed in the case SA178A and SA 213 T22, it evident from the calculation provided by figure 5-9 that the equilibrium vapor pressure of $FeCl_2$ is 2 orders of magnitude higher at 500 °C than nickel and chromium chlorides.

A difference in the corrosion behavior of the various steels at the different temperatures can be quantified in terms of an apparent activation energy. As discussed in chapter 2, the kinetics temperature dependence which follows an Arrhenius-type equation-the theory of which is discussed in chapter 2.

The activation energy is usually obtained by the slope of the log of the rate constant versus the inverse of absolute temperature. Using the data from figure 5-7, the parabolic constant cannot be determined, as all of the data points at the three temperatures were obtained at the same exposure time of 24 hours. Instead of the parabolic rate constant, the penetrations of these three materials after the 24-hour test were used to plot their temperature dependence. The densities of the steels- which can be found in chapter 4- were used to convert the mass loss (mg/cm^2) from figure 5-7 into a penetration (units of microns). The mass loss already assumed to be uniform based on normalizing the mass loss per area of the coupon.
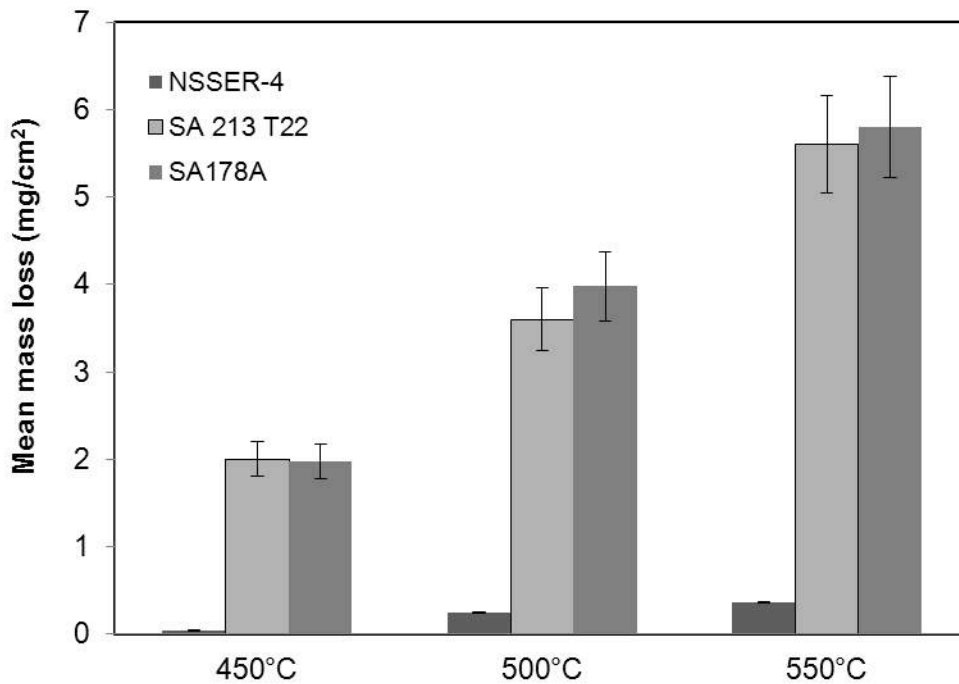
Figure 5-7. Corrosion rates of NSSER-4, SA178A, and SA213 T22 at 450 -550°C, under WTE flue gas containing 800 ppm HCl

The apparent activation energy calculated for SA178A, SA213 T22, and NSSER-4 is reported in Table 5-6. The low alloys steels are on the order of 110-111 kJ/mol, more than double the value for NSSER-4, 53 kJ/mol. Therefore the lower alloyed steeled are more sensitive to temperature than the austenitic stainless steels. The values for the apparent activation energy are comparable with the values obtained by Lee (2009) after 100-hour experiments determined that the apparent activated energies of SA178A and NSSER-4 were 149 kJ/mol and the 59 kJ/mol respectively between 486-586°C. The higher value for the apparent activation energy for SA178A can be explained by the results at 586°C which had a 7-fold increase of the

parabolic rate constant. Removing the value at 586°C, lowers the apparent activation energy to

117 kJ/mol.
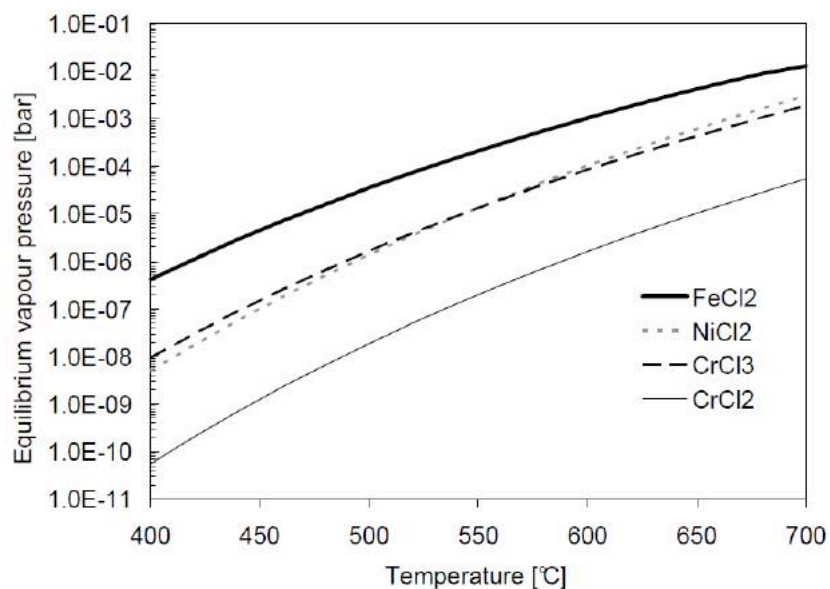
Figure 5-8. Equilibrium vapor pressures of solid metal chlorides as a function of temperature [106]

This agreement interesting to note as that the apparent activation energy for SA178A and NSSER-4 between those results and the result in this section were acquired over different time intervals, for 24 and 100 hours respectively. Therefore, it can be concluded, that the corrosion for SA 178A and NSSER-4 are in the same kinetic regime at 24 hours and 100 hours.

Table 5-5. Comparison of the types of mass losses for alloys, following 24 hour exposure

Alloy	Total mass loss (mg/cm²)	Mechanical removal (mg/cm²)	Chemical removal (mg/cm²)
SA178A	3.9	3.3	0.6
SA213 T22	3.6	2.3	1.1
NSSER-4	0.25	0	0.25

Table 5-6. Apparent activation energy for corrosion of alloy under WTE flue gas

Alloy	Apparent activation energy (kJ/mol)
SA178A	111
SA213 T22	110
NSSER-4	53

5.5 Comparison of isothermal vs. temperature gradient testing

Another interesting variable can be investigated from these results, is the impact of a temperature gradient on furnace experiments. One of the variables which exist in real boiler environments which are difficult to reproduce in laboratory experiments is the temperature gradient between the gas and metal surface. Typically for a WTE superheater, the flue gas and the tube temperature van vary between 200-300°C.   In reality that temperature difference also changes rapidly, based on the behavior in the boiler.

There have been experiments which have looked at high temperature corrosion in WTE environments under a gas-metal temperature gradient as well with a temperature fluctuation.

Lee (2009) looked at the corrosion of SA178A under a gas-metal temperature of ~250°C, by flowing air into a hollowed sample carrier for the alloy coupons within a furnace. Comparatively, Kawahara (2006) conducted tests with gas-metal temperature gradients between100-300 and also examined the gradient ramp rate between 100-300 °C.

Kawahara (2006) examined the effect of thermal gradient on the corrosion of SA178A under a WTE flue gas environment and identified that thermal gradient as high as 200°C had a minimal effect on accelerating the corrosion of SA178A [107]. The rate was affected at fluctuations exceeding 200°C/min over 50 hours, but only marginally increasing the thickness loss by 15% from 0.052 mm to 0.045 mm at a metal temperature of 550°C.

. The corrosion rate – as defined as the mass loss per area per time- is compared in Table 5-7 for the isothermal experiments reported in this chapter with the constant thermal gradient. The results are in virtually agreement with one another. This suggests that the spallation observed from the corrosion tests under the HCl environment likely occurs upon cooling and not during the experiment temperature. Alternatively, the broken layer would allow a significantly higher corrosion rate. Therefore, it is the metal temperature which most strongly governs the high temperature corrosion behavior.

Table 5-7. Comparison of corrosion rate in isothermal and temperature gradient environment ($\Delta T = 240°C$)

Alloy	Metal Temperature (°C)	Gas-Metal Temperature Gradient (°C)	Corrosion rate (mg/cm^2/h)
SA178A (c.s)	510	240°C (Gas ~750°C)	6.60E-02
SA178A (c.s)	500	0°C (isothermal)	6.37E-02

5.6 Conclusions

The high temperature corrosion of hydrogen chloride was examined for steels between 450-550°C. The primary corrosion mechanism was inferred to be active oxidation, based on various observations, the product characterization, and thermodynamic calculations discussed in this chapter. The oxidation induced by hydrogen chloride can be mitigated by replacing low alloyed steel with alloys containing chromium, as demonstrated with NSSER-4 (Fe-17Cr-13Ni). The addition of chromium and nickel has been noted in literature to form a more protective, passive oxide layer. The higher alloyed material also had a lower sensitivity to temperature as quantified by lower activation energy between 450-550°C. NSSER-4 had nearly half (53 kJ/mol) the value of the carbon and low alloyed steel respectively (110-111 kJ/mol).

Chapter 6: High Temperature Corrosion of Alloys below Chloride Salts Deposits

6.1 Summary

In this chapter, the corrosion behavior below chloride salts was investigated with sodium chloride as a surrogate compound. Furnace tests were performed on carbon steel SA17A, low-alloyed steel SA213 T22, austenitic steel NSSER-4 (Fe-17Cr-13Ni) and nickel based coatings (Inconel 625, SP 99, SW1600, SW1641, and colmonoy 88) on SA 213 T22.. Tests were conducted under a simulated WTE flue gas environment, with a NaCl loading of 4.0 mg/cm$^2\pm$ 10% at 450°, 500°, and 550°C for 24 hours.

The addition of the sodium chloride layer accelerated the corrosion of SA178A, SA 213 T22, and NSSER-4 by nearly an order of magnitude below the previous gas exposure containing 800 ppmv HCl. It was determined through a combination of SEM-EDS and XRD that the sodium chloride participates in two reactions. The first is the sulfation reaction in which sodium chloride is converted to sodium sulfate. The second reaction is the formation of sodium chromate, which has been suggested in other literature as a type of active oxidation which can accelerate the corrosion of alloys.

The sodium chloride corrosion tests were the then executed for several nickel based coatings, Inconel 625, Colmonoy 88, SP 99, SW1600 and SW1641 applied on SA213 T22. The tests confirmed similar behavior to that which was observed for the steels, namely the onset of the sulfation reaction and the formation of sodium chromate. Inconel 625, SW1600, and SW1641 were shown to have a significant corrosion penetration below the salt layer, where sodium and sulfur were detected with chromium and oxygen, suggesting the attack of chromium rich oxide

layers. The colmonoy 88 applied coatings, conversely, demonstrated excellent corrosion resistance. It is suggested that the alloying addition of tungsten helps to mitigate the effective pitting corrosion caused by localized depletion of the passive chromium rich oxide layer by sodium chloride.

6. 2. Introduction

Corrosion of alloys below chloride-containing ash deposits is considered to be even more severe than in a chlorine-containing atmosphere without deposits. Gaseous HCl is less corrosive than alkali chloride deposits. These compounds can accelerate corrosion, even at temperatures below first melting temperature (FMT) [118-120]. The atmosphere in contact with the deposits and the corrosion layer affects reactions which can alter the deposit and the partial pressure of oxidizing agents near the metal [108].

In the following experiments, the behavior of the various alloys was investigated under the sodium chloride layer at the three temperatures discussed in chapter 5 (450°, 500°, and 550°C respectively). The samples were covered with NaCl by droplet addition of an aqueous solution and dried at 110°C to evaporate the moisture. The coupons were weighed afterward in order to report the mass addition from the salt layer and were controlled to 4.0 mg/cm^2. The coupons intentionally had parts of the surface uncovered to allow for surface characterization of the coupon surface with and without a chloride layer.

6.3. Studies with SA178A, SA213 T22, and NSSER-4

6.3.1 Mass change and observations

Steel coupons underwent significant corrosion under the sodium chloride salt layer, following 24 hour experiments under the WTE flue gas exposure. The average mass loss in mg/cm^2, of the coupons of SA178A, SA213 T22, and NSSER-4 at 450°, 500° and 550°C is shown figure 6-1. The values of are an average of 6 coupons. The values of SA178A and SA 213 T22 are similar to each another varying between 33-65 mg/cm^2 for the temperature range investigated. NSSER-4 had a marginal mass loss of 0.6 mg/cm^{2,} at 450 °C but increased significantly with temperature. At 450°C, NSSER-4 had a favor of 55 smaller mass loss than SA178A, at 500 °C it was 23 and by 550°C it was a factor of 11 smaller. For industrial purposes, the austenitic steel, Ni-17Cr-13 Ni, showed once again an excellent corrosion resistance under an aggressive oxidizing-chlorinating environment.

The mass loss of three steels under the sodium chloride layer can be compared with the results in chapter 5, in figure 5-7, which displayed the mass loss under the HCl-containing flue gas alone. The values varied from 2 mg/cm^2 to 6 mg/cm^2 between 450°C and 550°C. Therefore, as expected, the corrosion below the sodium chloride layer was even more severe, by an order of magnitude or more.

Examples of coupons from SA213 T22 and NSSER-4 are shown in figure 6-2. SA 213 T22 and SA178A were virtually identical in appearance, so SA178A is not shown. At 450°C, some oxidation is visible around and under the white deposit- which was originally part of the sodium chloride layer that was applied to the coupons. After the 24 hours tests at 500°C, the

appearance of a white deposit was still visible on the NSSER-4 coupon but nearly undetectable

for the carbon and low alloy steel. The corrosion layer on SA178A and SA213 T22 was
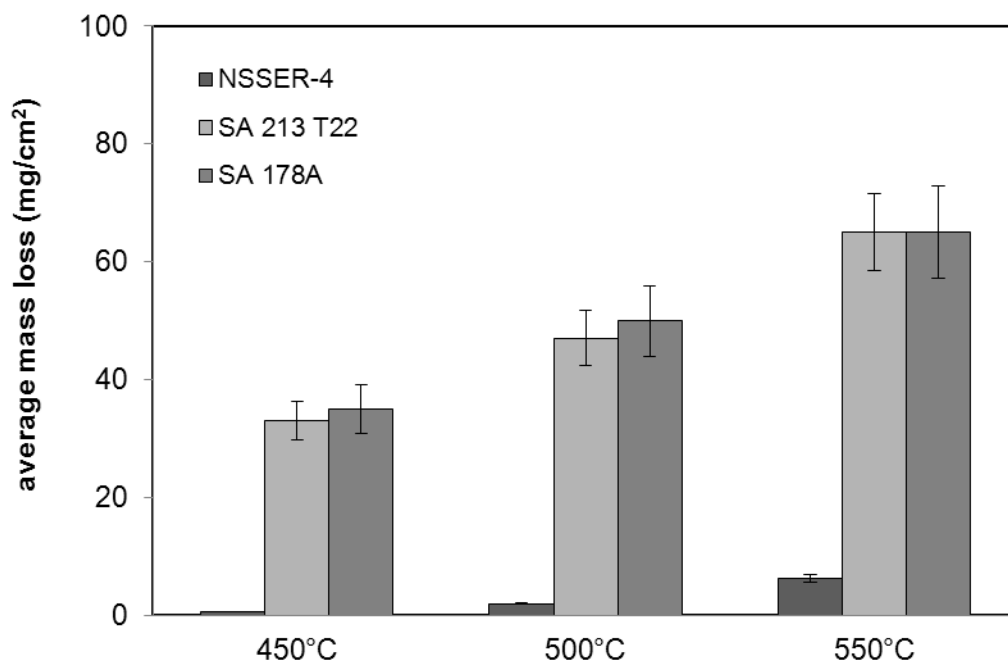

Figure 6-1. Average mass loss of SA178A, SA213 T22, and NSSER-4 under NaCl layer and WTE flue gas at 450°, 500°, and 550 °C

Alloy	450°C	500°C	550°C
SA213 T22			
NSSER-4			

Figure 6-2. Coupons of SA213 T22 and NSSER-4 under NaCl layer following 24 experiments at 450, 500, and 550°C

sufficiently large to exhibit spallation when cooled to room temperature. The spalled corrosion layer was harvested and ground into powder and analyzed via X-ray diffraction- the results of which are discussed in section 6.3.3. At 550°C the NSSER-4 coupons also exhibited a powdery residue but still did not produce a recoverable corrosion layer. The residue that could be recovered was also studied.

6.3.2 Surface characterization

The surface of coupons SA 213 T22 and NSSER-4 coupons was also investigated by SEM-EDS. Figures 6-3 shows the micrograph and the elemental composition of the SA 213 T22 at 450 and 550°C. The surface image and elemental analysis are consistent with the physical observations in Figure 6-2. The EDS analysis also suggests that the sodium chloride that was present on the coupon surface from sodium chloride is now a composed of chloride and sulfate. This suggests that some of the sodium chloride salt layer has reacted with the sulfur in the synthetic WTE flue gas mixture to form sodium sulfate. This was compared to the surface SEM-EDS of NSSER-4, figure 6-4 which only showed sulfur on the surface. Additionally, it was observed that no chromium was found on the surface of the coupon around the salt at 550 C, while some was present at the lower temperature.

6.3.3 XRD of corrosion products

As mentioned in section 6.3.1, the spallation of SA213 T22 coupons was retrieved following the experiment. The scales were ground with an agate mortar and pestle and analyzed via powder x-ray diffraction. The pattern from the scales recovered at 450°C and 550°C are

shown in figures 6-5 and 6-6. Both samples detected a mixture of iron oxides and sodium chromate. The scale at 550° also detected chromium iron oxide. Neither sample detected sodium chloride or sodium sulfate.

Figure 6-3 (a). Surface SEM-EDS of SA213 T22 coupon following 24 hour experiment under sodium chloride layer at 450°C. Surface shows a mixed chlorine-sulfur surface, suggesting the conversion of NaCl to Na_2SO_4. Iron, oxygen, and alloying element M also detected.

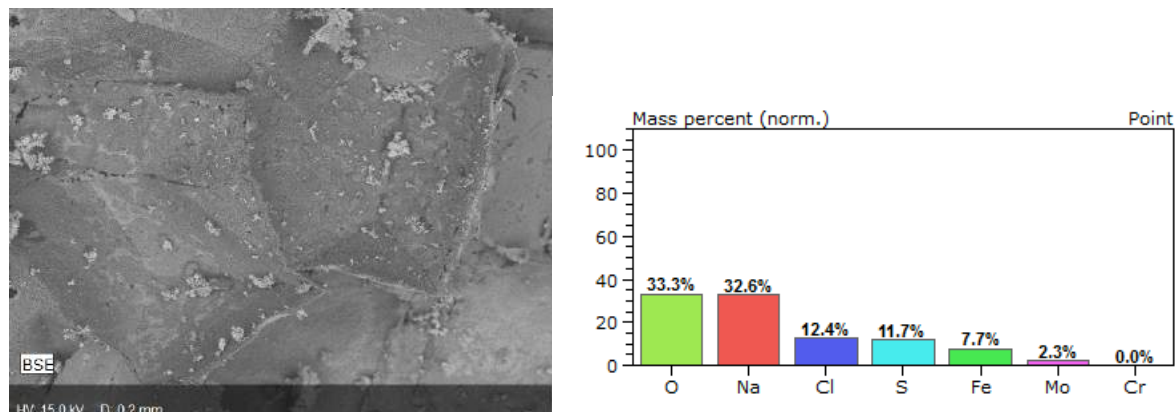**Figure 6-3 (b).** Surface SEM-EDS of SA213 T22 coupon following 24 hour experiment under sodium chloride layer at 550°C. Surface shows surface that is rich with iron oxides with a small mass percent of sulfur and sodium. Chlorine is barely detected.

Figure 6-4 (a). Surface SEM-EDS of NSSER-4 coupon following 24 hour experiment under sodium chloride layer at 450°C. Surface largely shows the salt layer on the coupons surface which detects no chlorine, but 16.9 wt% sulfur.
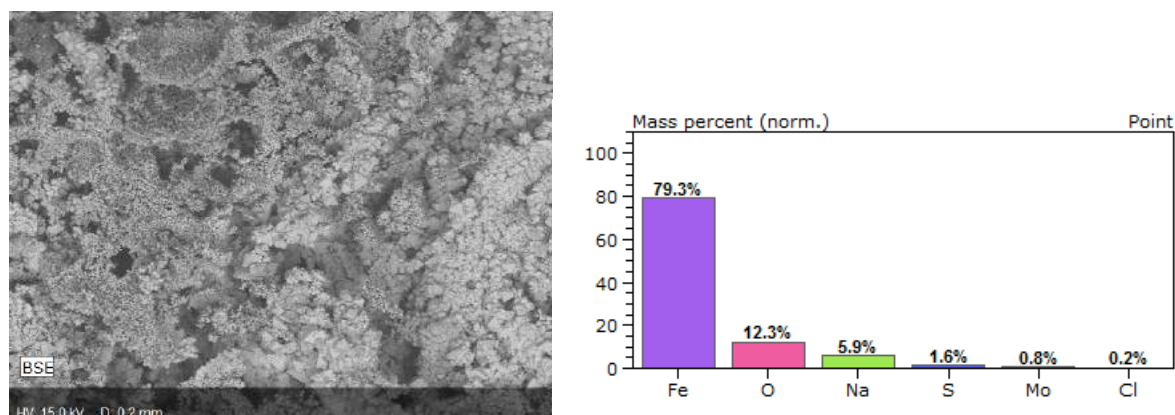

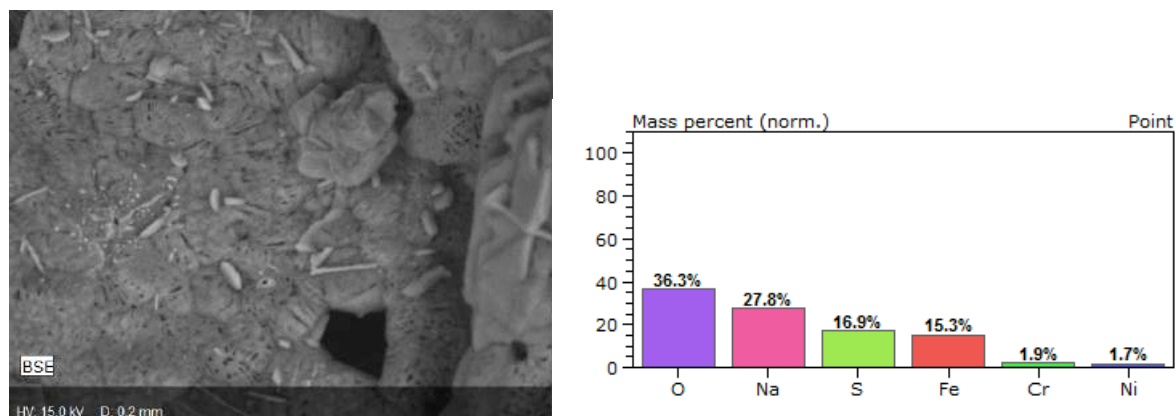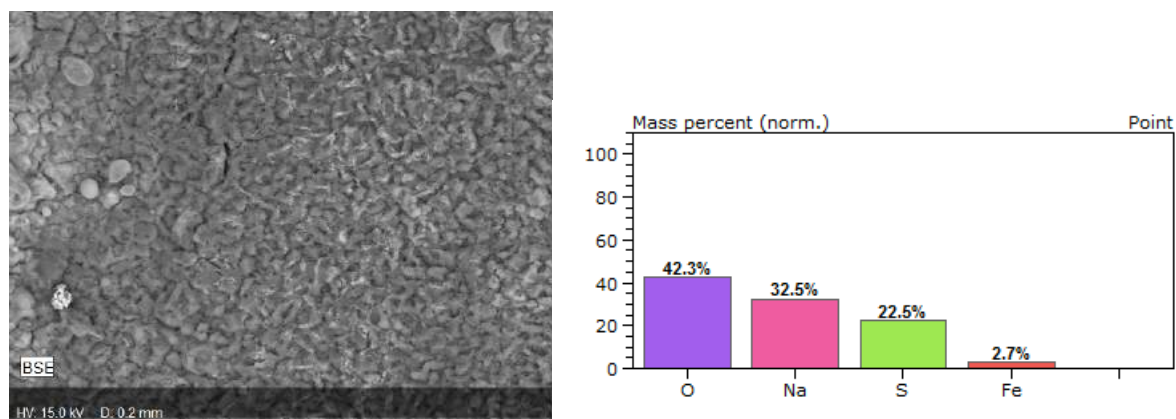**Figure 6-4 (b).** Surface SEM-EDS of NSSER-4 coupon following 24 hour experiment under sodium chloride layer at 550°C. Surface largely shows the sodium and sulfur from the salt layer surface.

The mass recovered from the scales was relatively large, about 80-90 mg such that the entire mass was not analyzed in the run. This may explain why surface analysis detected the presence of sulfur compounds and the XRD pattern did not identify a sulfur compound. It should also state that one of the limitations of EDS is the penetration depth of ~100 nm for backscattering detector. Therefore while sulfur may have been present, the remnant of the salt may not have been present. Meanwhile, as the corrosion products of NSSER-4 coupon were too small to recover at 450°C, the oxide layer was thin enough such that the only powder recovered was sodium sulfate.

Figure 6-5. XRD pattern of scale recovered from SA 213 T22 following 24 hour experiment at 450°C. Peaks identified include iron oxides: Fe_2O_3 and Fe_3O_4 and a sodium chromium oxide
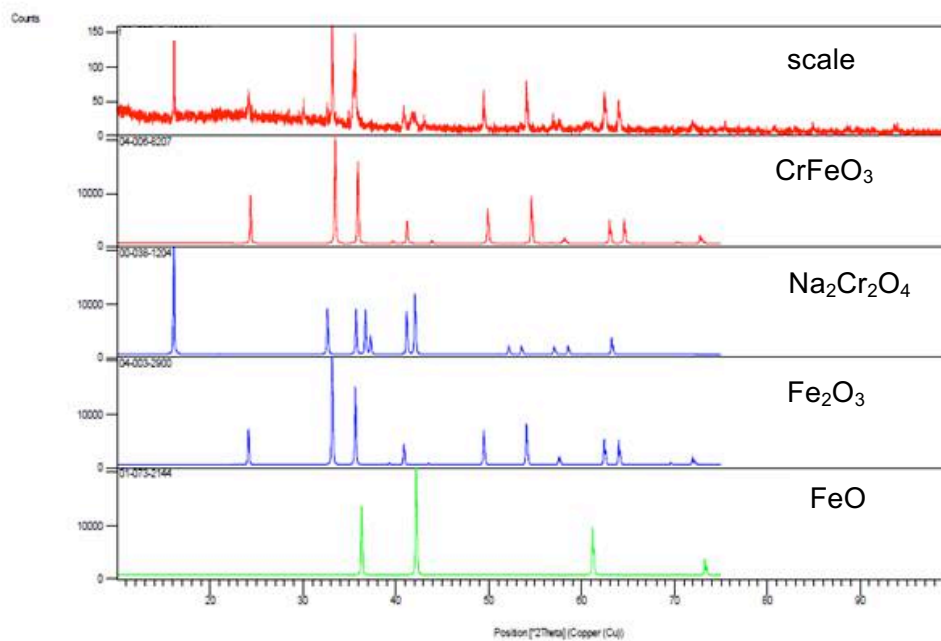
Figure 6-6. XRD pattern of scale recovered from SA 213 T22 following 24 hour experiment at 550°C. Peaks identified include iron oxides: Fe_2O_3, chromium iron oxide,
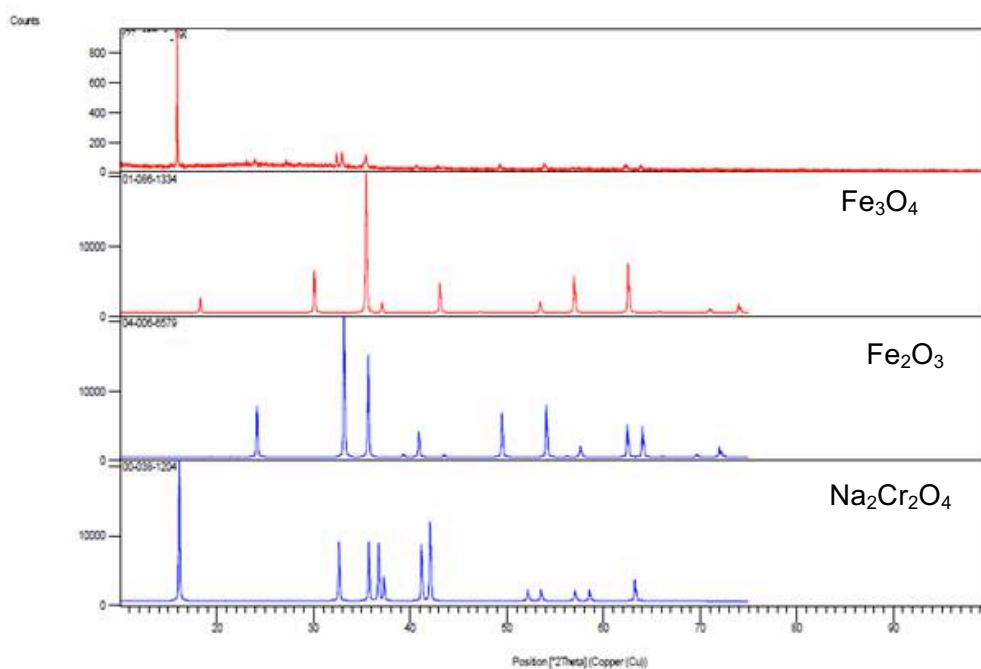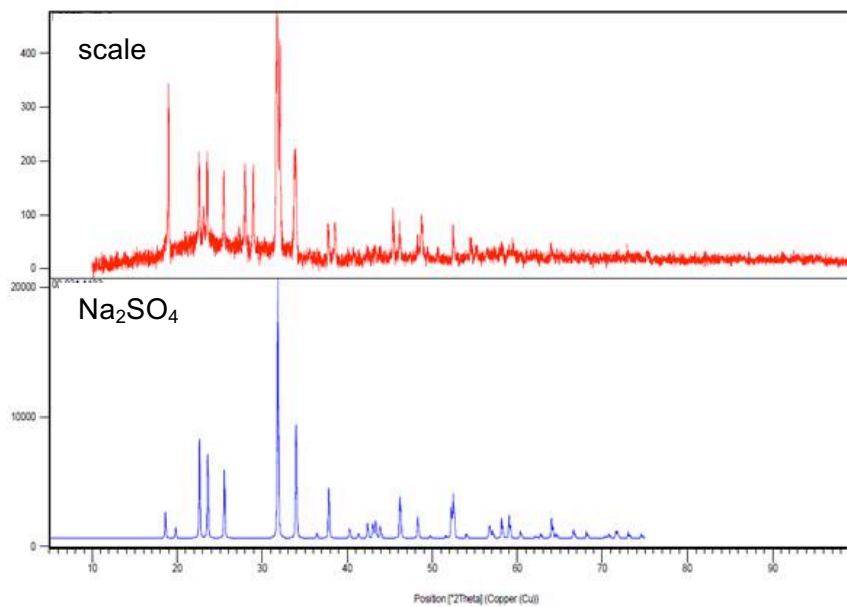

Figure 6-7. XRD pattern of powder recovered from NSSER-4 coupon following 24 hours experiment at 450°C.
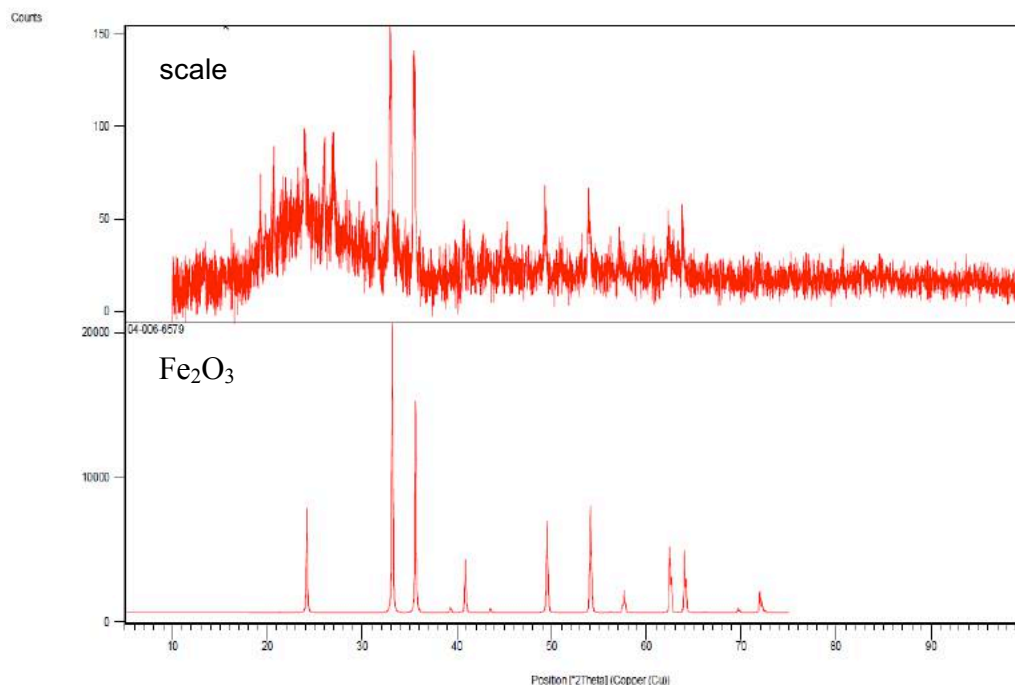
Figure 6-8. XRD pattern of powder recovered from NSSER-4 coupon following 24 hour experiment at 550°C.

6.3.4 Discussion

Based on the high temperature corrosion literature review that was conveyed in chapter 2, there are three possible options for sodium chloride to accelerate corrosion at 450-550°C. The first is the formation of a molten chloride mixture, which in turn fluxes, or dissolves the surrounding metal oxides. Table 2-5 in chapter 2 identified some common molten chloride mixtures. Based on the temperature investigated, the only mixture that could exist under the conditions investigated here is the $FeCl_2$-NaCl which has a first melting temperature at 370°C. As stated in previous chapters, iron chlorides are only stable in environments with very low partial pressure of oxygen. According to the Fe-O-Cl predominance diagram at 500°C, the partial pressure of oxygen at the oxide-metal interface would need to be on the order of 10^{-14} bar for formation of iron chloride species to be thermodynamically possible. So while the formation of

the low melting mixture cannot be ruled out it would occur where virtually no oxygen is present. An additional considered for a molten phase is $NaCl$-Na_2SO_4 since the product characterization in figure 6-3 identified the conversion of sodium chloride to sodium sulfate. However, the FMT temperature of a $NaCl$-Na_2SO_4 is at 657°C. Therefore, it is highly unlikely that the elevated corrosion rates for SA178A, SA213 T22, and NSSER-4 shown in figure 6-1 would attributed to a molten salt corrosion. A second possible reaction mechanism is the sulfation reaction. Reaction 6-1 below demonstrates the reaction stoichiometry. 1 mole of chlorine gas is released for every 2 moles of sodium chloride converted to sulfate. This release of additional Cl_2 alone may not necessarily accelerate the high temperature corrosion of alloy, since it has been already been

$$2\ NaCl + SO_2 + O_2 =\ Na_2SO_4 + Cl_2 \qquad\qquad (6\text{-}1)$$

$$2\ NaCl + Fe_2O_3 + 0.5\ O_2 =\ Na_2Fe_2O_4 + Cl_2 \qquad\qquad (6\text{-}2)$$

$$2\ NaCl + Cr_2O_3 + 2.5\ O_2 =\ 2Na_2CrO_4 + 2Cl_2 \qquad\qquad (6\text{-}3)$$
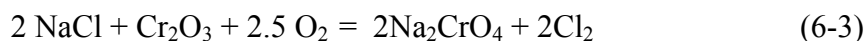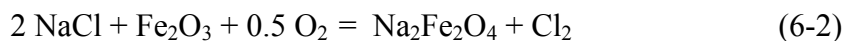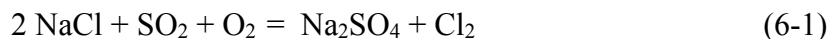
At 500°C: ΔG (rxn **6-1**) = -100 kJ/mol;
ΔG (**rxn 6-2**) = -54 kJ/mol;
ΔG (**rxn 6-3**) = -287 kJ/mol

shown in Chapter 5 that effectively doubling the concentration of HCl from 400 ppmv to 800 ppmv at 500°C, only increase the mass loss by about 20%. However, some in the literature have suggested that the sulfation reaction can accelerate corrosion if the chlorine gas diffuses from the

deposits into the oxide layer [109]. However, as it will be shown in chapter 7, sulfation reaction has demonstrated in some cases to mitigate the corrosion of alloys.

The third reaction that is considered was previously discussed in chapter 2, in which alkali chlorides (e.g. NaCl) react with iron or chromium oxides. The reactions being discussed here—and shown in the schematic, figure 6-8. As in the case of the sulfation reaction (reaction 6-1) chlorine gas is released, this can be similar to the active oxidation mechanism discussed for HCl. Unlike the behavior of HCl, this reaction consumed an oxide that was present on the alloy surface, thus depleting a protective barrier to the virgin metal surface. Based on the XRD pattern in figures 6-5 and 6-6 identifying the formation of sodium chromate, it is most likely that the acceleration under the sodium chloride layer is caused by these types of reactions. As will be shown in the following section, the formation of sodium chromate was observed again for Inconel 625 coupons which further support this claim.

Although the XRD pattern recovered from the small powder from the NSSER-4 coupons was inconclusive, in terms of identifying a probable mechanism, it should be noted that the powder analysis and the surface EDS are marked by a significantly high concentration of iron and a low concentration of chromium. This may suggest that the chromium layer which grown on the surface of the alloy was depleted by sodium chloride allowing for the outward growth of iron oxides. Further characterization would be needed to confirm this hypothesis- specifically, a cross sectional image of a NSSER-4 coupon with an elemental mapping to identify where iron, chromium, and nickel and perhaps chloride resides.
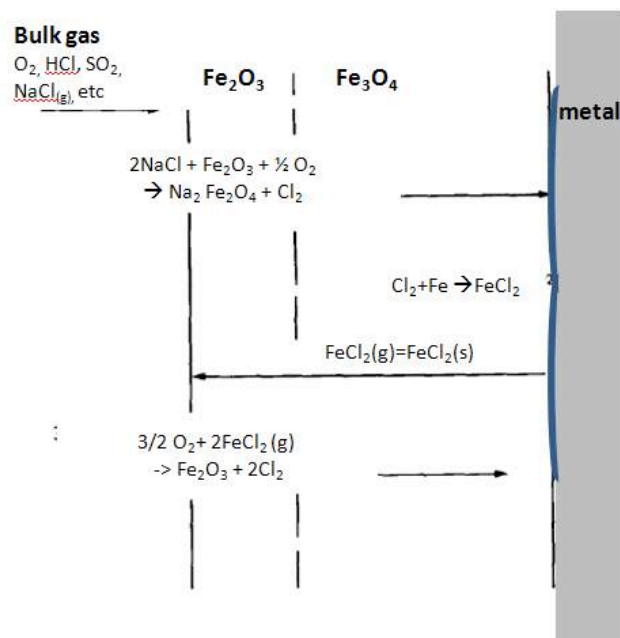
Figure 6-9. Illustration of an active oxidation mechanism induced by alkali chlorides

6.4. Studies with nickel coatings

The experiments with SA178A, SA 213 T22, NSSER-4 not only provided insight on the corrosion behavior under sodium chloride layer, it served as the validation of 24 hour furnace test as an approach for investigating the corrosion behavior of multiples alloys in a relatively short period of time. This test was executed to rank the corrosion resistance of various nickel coatings applied to SA 213 T22. The composition of the alloys and the coating process was previously shown in Table 4-2 and is repeated below as matter of convenience to the reader.

The results of six coating are discussed in the following section. They were comprised of 5 unique materials: Inconel 625, Colmonoy 88, SP 99, SW1600, and SW1641. The other coating was Colmonoy 88 applied by a laser weld, so that the performance of the application technology can also be compared. SP 99 has a very similar composition to colmonoy, with the addition of 1 wt% Molybdenum. SW1600 and SW1641 belong to a group of NiCrMoBSi alloys. For these

experiments, the coupons were fabricated with base metal, SA 213 T22 included. The sodium chloride layer was applied only to the top surface of the coupons, with the coating material. As SA213 T22 has been extensively studied at these temperatures and gas conditions, the mass loss of the SA213 T22 was subtracted from the overall mass loss to report the true mass loss of the coated material. The values for the mass loss are those from the gas environment (figure 5-7), as sodium chloride was not applied to the base metal. Careful consideration was also taken to polish the base metal and flatten the coupon and measure is area with a caliper to have an accurate area for the mass correction. This method for reporting the mass loss was validated by the cross section measurements of the corrosion images in Table 6-2. The rank and relative proportion of the largest measured corrosion depth is, outside of one outlier, consistent with the trend in mass loss measurements.

Table 4-2. **Elemental** composition of investigated protective coatings

Alloy	Process	Composition							
		Ni	Cr	C	B	Si	Mo	W	Fe
Inconel 625	laser	Balance	21.5	0.1			10		5.6
Colmonoy 88	HVOF	Balance	15	0.8				17.3	10.9
Colmonoy 88	laser	Balance	15	0.8				17.3	10.9
SP 99	laser	Balance	15		3	4	1.0	17.3	3.5
SW 1600	TS and IH	Balance	15		3.1	4.3	2.5		
SW 1641	TS and IH	Balance	37.1		3.6	3.4	3		
Substrate		Composition							
		Ni	Cr	C	B	Si	Mo	W	Fe
SA213 T22			2.25	0.1			1		Balance

6.4.1. Alloy ranking

The results of coating tests are provided in figure 6-7 for all three test temperatures. The mass loss of the base metal, SA213 T22, was also included for comparison. As expected, the coating mass losses were lower than SA 213 T22, with the exception of SW1600. (It should be noted that since SW1600 is more a dense material than SA213 T22, the calculated corrosion penetration, corrosion rate would be smaller, even if the mass change were identical). The mass loss for the coatings typically varied between 10-40 mg/cm^2 between the tested temperature range. The hierarchy of the coatings was the same at each temperature, i.e. the best performing alloy had the lowest mass loss at each temperature and the worst performing alloy had the greatest mass loss at each temperature.

High velocity oxygen fuel applied (HVOF) colmonoy 88 was the superior material with a mass loss ranging between 0.3-3.1 mg/cm^2. This equates to a corrosion rate of 5.0 E-04 mil/h at a the temperature of 450°C. The mass loss acquired for the HVOF colmonoy 88 was a factor of ten lower than the next resistant coating which was the laser cladded colmonoy 88.

6.4.2 Mass loss and observations

The images of coupon surfaces following the furnace experiments can be found in Appendix A. The sodium salt layer behaved in some ways similarly to the experiments on low alloyed steels and NSSER-4. The sodium salt layer remained largely visible at 450° and 500°C and was then indistinguishable at 550° C. One difference with the salt on the nickel coatings was the appearance of a color change from white to yellow. This was observed most prominently for SW1600.

Each coating itself underwent color changes after the furnace test, with the exception of the HVOF colmonoy 88 which was initially dark. The most intense color changes on the coating surface were observed at or around the sodium salt layer. For some alloys the color change was a black film (laser colmonoy 88), and red for other coatings (e.g. SP 99). Inconel 625 and SW 1600 had what can be described as a macroscale pit forming around the sodium salt deposit at 450° and 500°C. At 550 °C, the surface appeared to have a uniform corrosion.
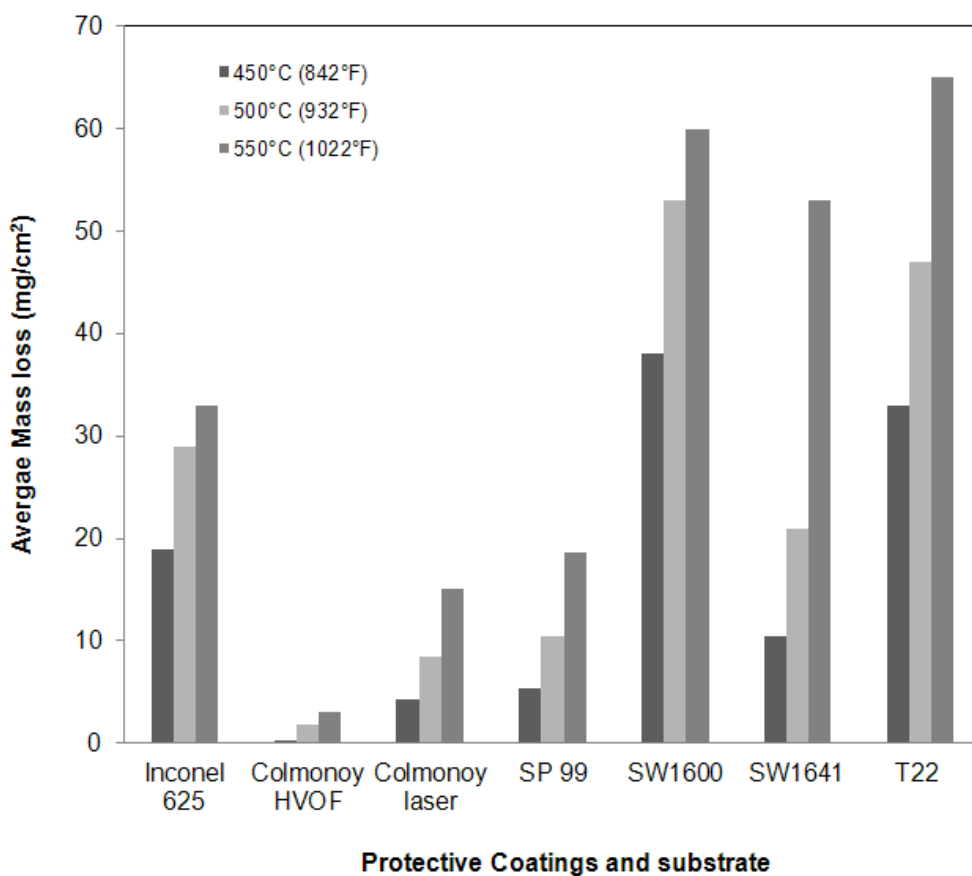

Figure 6-10. Average mass loss of Ni-coatings, Inconel 625, Colmonoy 88, SP 99, SW1600, and SW1641 applied to SA213 T22 following 24 hour exposure under NaCl layer and WTE flue gas at 450°, 500°, and 550°C

6.4.3 Product analysis

With the exception of Inconel 625, the corrosion products could not be removed from the coupon without compromising the coating surface. The corrosion products from Inconel 625 were grounded and studied with XRD. The pattern of the scale is provided in figure 6-7. The other coatings were embedded in POLYCAST-128 metallographic resin and a cross section SEM-EDS analysis was performed. The image for the nickel coatings at 500° C are shown in Table 6-1. The elemental composition of the corrosion products adjacent to the coating surface is also provided, as the average of four EDS spot analysis.

The peaks in the Inconel 625 scale include nickel oxide, sodium sulfate, sodium chromate and iron oxide (magnetite). The detection of sodium chromate is an indication of a reaction between sodium chloride and chromium oxide as previously discussed in section 6.3.4. Additionally, iron is observed on the coupon surface via SEM-EDS analysis in figure 6-8. The combination of a depleted chromium oxides and the onset of iron oxide forming on the coupon surface can help explain the high mass loss measured for the Inconel coupons. The depletion of the protective chromium oxide layer allows for outward growth of the iron oxide layer to the surface. The formation of sodium chromate may also suggest why a yellow residue was observed on the salt layer on the surface of coupons like SW1600. Sodium chromate is a yellow solid at room temperature, whereas sodium sulfate and sodium chloride are white [110].

Three salient observations can be conveyed from the cross section elemental analysis in Table 6-1. The first is that similar to Inconel 625, SW1600 and SW1641 show an unexpected
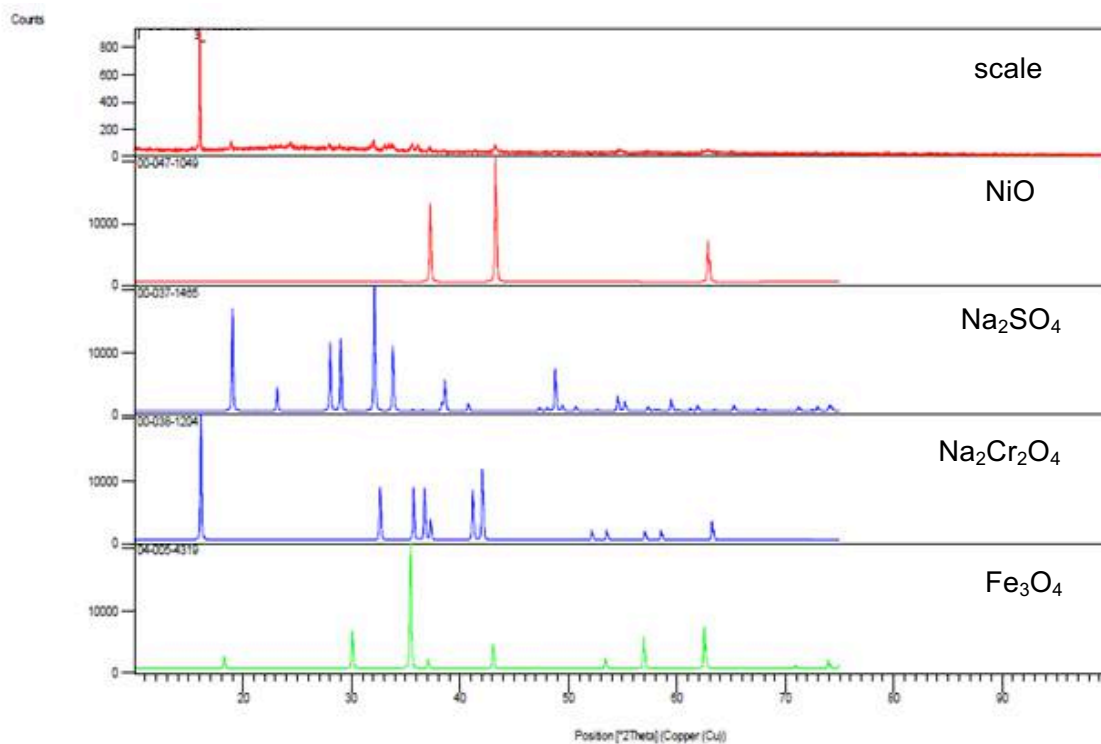
Figure 6-11. XRD pattern of scale recovered from Inconel 625 coating at 500°C.
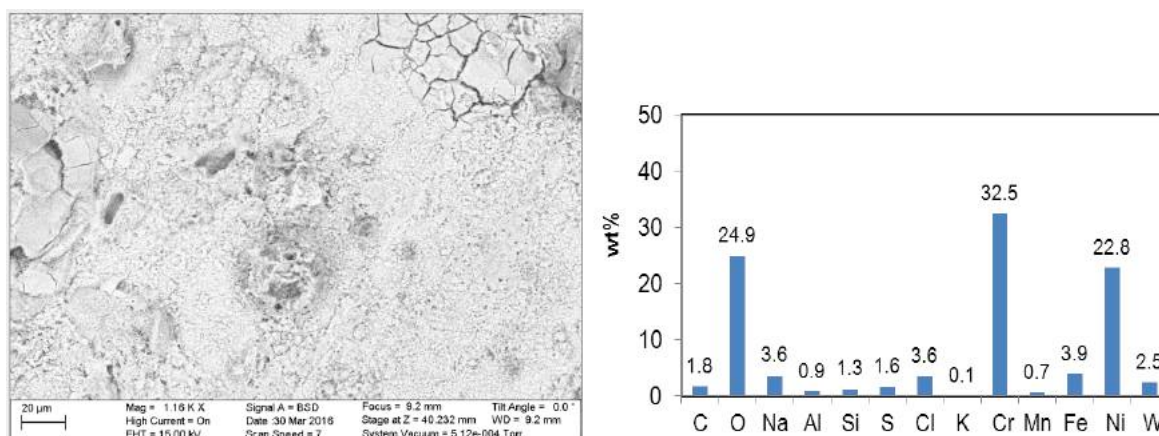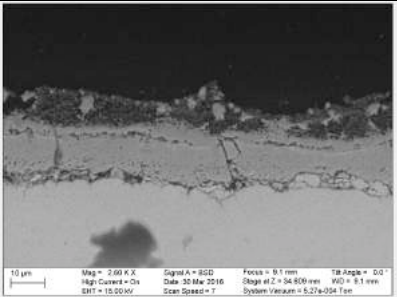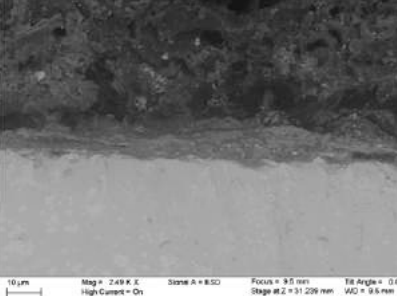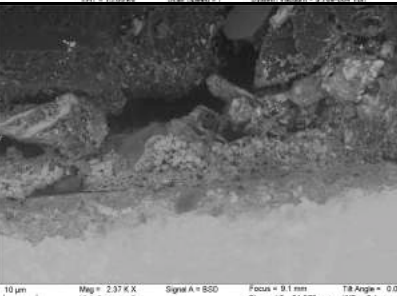

Figure 6-12. Surface SEM-EDS of Inconel 625 scale at 500°C. The iron content on the surface averaged 3-4 wt% in spots like the one shown above.

value for iron, 3 and 5 wt% respectively. Unlike Inconel 625, which contains iron, the source of in SW1600 and SW1641 is likely from an impurity which was introduced during the coating process. The cross section image confirms that the coating was still intact below the corrosion penetration. It should be noted also that iron is even measured on the surface SW1600 and SW1641 coupons. It is most notably observed at 550 °C detects iron at 1 and 3.6 wt% on the surface at 550°C (figure 6-9). The second observation is that SW1600 and SW1641 also had a comparatively lower value for chromium at 1 and 4 wt% while the sodium and sulfur peaks were discernibly higher. In the elemental mapping for these images, shown in chapter 7, the fissures found below the salt layer (most notably seen in SW1641) feature chromium, oxygen, sulfur, and sodium. Based on the behavior observed for Inconel 625, it can be inferred that the sodium chloride attacks the chromium rich oxide layer.

The second important observation is that the three coatings which have the lowest mass loss have one common feature: the alloying of tungsten and substantial concentration of tungsten found adjacent to the metal surface. While not commonly cited in high temperature corrosion literature, tungsten is cited elsewhere for improving resistance against pitting corrosion [111-112]. Simply defined, pitting corrosion is a localized form of attack that results in a rapid penetration at small discrete areas. Pitting corrosion results from a failure of a passive film. It can be argued that the high temperature corrosion of alkali chlorides is a form of pitting corrosion. Tungsten alloying benefits are often compared with molybdenum, as they are both strong carbide former sand solid solution strengtheners [113]. In terms of corrosion resistance, molybdenum and tungsten have been shown to increase the passivity of austenitic steels and nickel alloys but stabilizing microstructure. Despite their similarities, it is apparent, especially

Table 6-1. Cross section image of coatings Colmonoy 88, SP 99, SW1600 and SW161 under NaCl layer at 500°C and compositions of corrosion products adjacent to metal surface

Coating	Cross section image (500°C)	Corrosion products adjacent to metal (wt%)
Colmonoy88 (HVOF)		32 O, 5Na, 10W 4 S, 15Cr, 5 Fe, 26 Ni
Colmonoy88 (laser)		31 O, 11Na, 7W, 7S, 14 Cr, 6Fe. 28 Ni
SP 99		32 O, 4Na, 3 Si, 10 W, 4 S, 1Cl, 12Cr, 5 Fe, 27 Ni
SW1600		40O, 24 Ni, 22 S, 10 Na, 1 Cr, 5 Fe

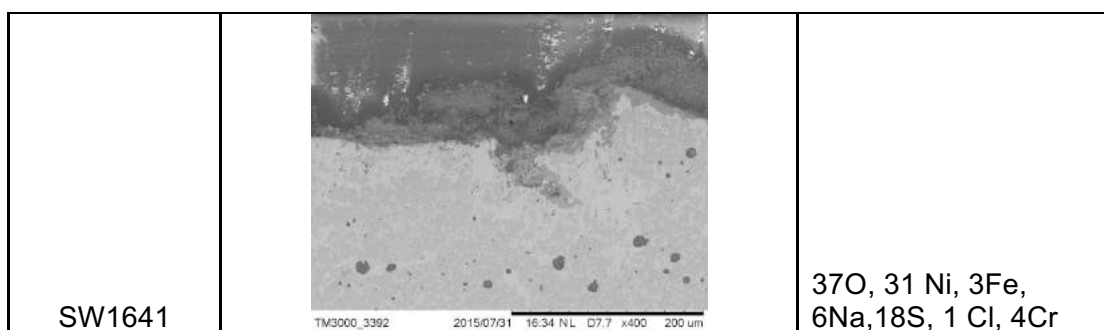|		
SW1641	TM3000_3392 2015/07/31 16:34 NL D7.7 x400 200 um	37O, 31 Ni, 3Fe, 6Na,18S, 1 Cl, 4Cr

Table 6-2. Comparison of corrosion depth measured by coupon cross section (average of 3 penetration depths) and mass loss obtained from ASTM method. The depths are consistent with the mass loss reported, with the exception of the laser cladded colmonoy 88

Comparison of average corrosion depth and mass loss at 500°C		
Coating	Mass loss (mg/cm^2)	Depth, μm (mil)
Colmonoy 88 (HVOF)	1.8	2.5 (0.1)
SP 99	10.4	21.4 (0.83)
Colmonoy 88 (laser)	11.6	40.4 (1.6)
SW1641	21	58.0 (2.3)
SW1600	53	101 (4)

when comparing the results of Inconel 625 (which contains ~10% Mo) the addition of tungsten is more effective in increasing the corrosion resistance under alkali chlorides. It would be of interested to quantify whether there is a relationship that can be expressed between the corrosion performance under chloride salts and the percentage of tungsten in nickel-chromium alloys. A relationship for pitting corrosion in iron (III) chloride solution has been developed for austenitic steels and nickel alloys. For the latter, the resistance to pitting corrosion (PREN) is expressed as PREN= % Cr + 3* (%Mo + %W) [126]. While this relationship does not hold for the data provided in this chapter, it can serve as the impetus for a future study on various nickel coating with varying additions of molybdenum and tungsten.
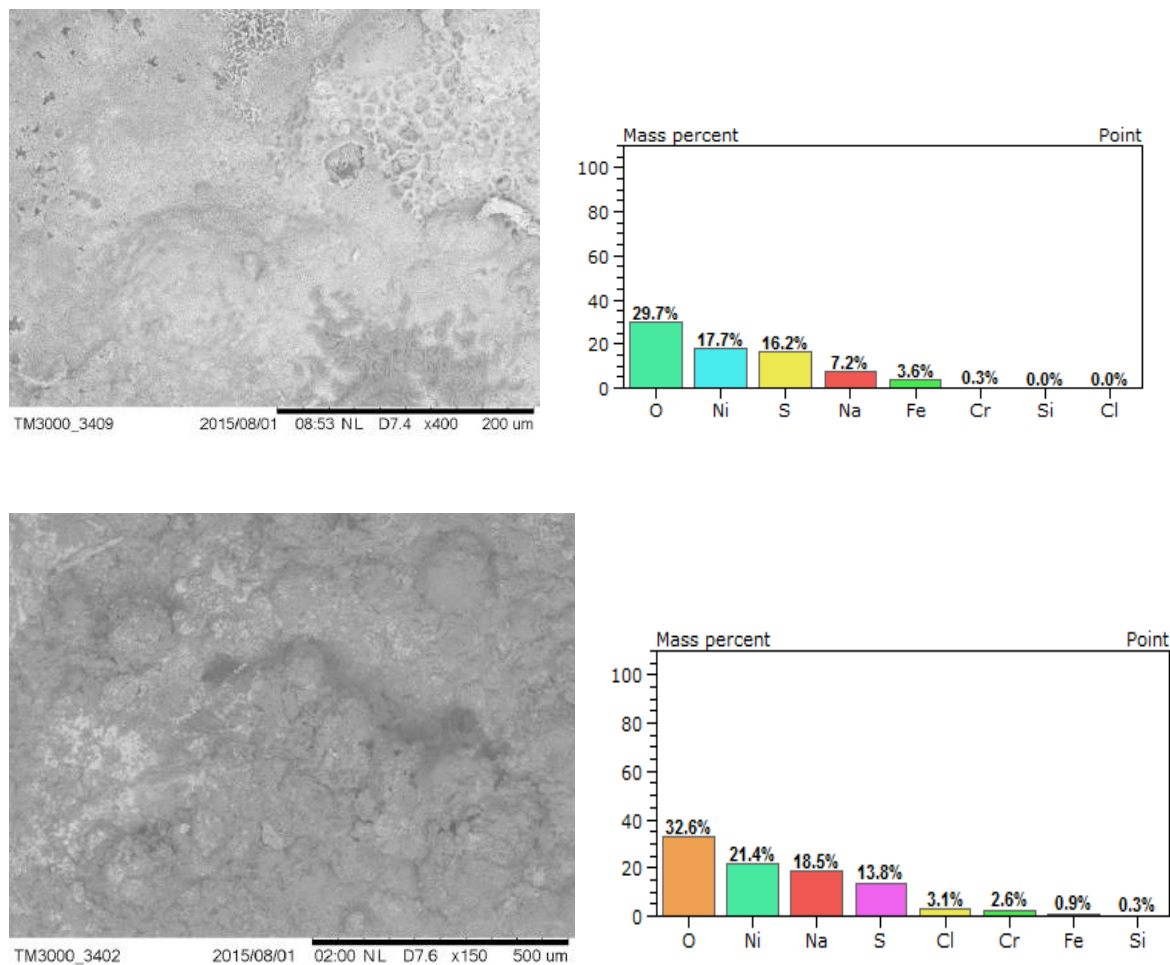
Figure 6-13. SEM-EDS of surface of SW1600 (top) and SW1641 (bottom) coupons at 550°C. EDS. Surface EDS shows the presence of iron on both surfaces, which is unexpected.

Lastly, the results in figure 6-7 revealed that the HVOF application of colmonoy 88 had ten-fold improvement in corrosion resistance over laser welded coating. The elemental composition adjacent to the alloy surface does not provide enough information to distinguish why HVOF performed significantly better than the laser cladding. The cross section measurement for the laser colmonoy coating did identify one location under the chloride layer which has a more

significant penetration than under the HVOF coating. This was realized by the skewed average penetration reported in table 6-2. Thermally sprayed coatings are mainly attacked through oxides and voids at splat boundaries. The extent of the oxides at splat boundaries is controlled by reducing the spraying temperature [114]. It is recommended based on the performance of the HVOF coating in this chapter, to continue with the current spray conditions.

6.5. Conclusions

One of the common chlorine compounds present in WTE boilers are alkali chlorides. These compounds are one of the major components in fly ash. As shown in this chapter, the deposition of alkali chlorides on boiler tube surfaces readily engage in high temperature corrosion mechanisms The sodium chloride induced corrosion occurs below the salt layer and has a proclivity for depleting alloy surfaces of protective and semi-protective oxides. The extent of corrosion is more aggressive that hydrogen chloride and is quantifiable for many alloys even after 24 hours of simulated exposure. One of the ways to mitigate the corrosion induced by sodium chloride, is to add elements such as tungsten and molybdenum which have been shown in other corrosion literature to have reduce pitting corrosion. In the tests discussed in chapter 6, tungsten was especially effective, as part of Colmonoy 88.

Chapter 7: The Effect of Sulfur on High Temperature Corrosion

7.1. Summary

In this chapter, the effect of sulfur on WTE boiler corrosion is discussed. Sulfur is a minor component of MSW, an order of magnitude less than chlorides. Industrial experience has shown that the introduction of sulfur sources (e.g. coal, sulfur additives) into WTE boilers replaces boiler tube deposits rich in chlorides with sulfates and subsequently corrodes at much lower rates. These trends have prompted several research endeavors into understanding the mechanisms and developing commercial approaches for its use.

Experiments have demonstrated that sulfates are semi-protective on WTE boiler tube surfaces up to temperatures of 550°C. The corrosion rates for carbon steel and Fe-17Cr-13Ni (NSSER-4) under sodium sulfate had an order of magnitude less corrosion than under sodium chloride. The remainder of the chapter investigates the how the change of sulfur in the gas composition, expressed using the SO_2/HCl ratio, impacts the high temperature corrosion of alloys. Typical levels of the SO_2/HCl flue gas ratio in WTE boilers range between 0.1-0.3 [115]. As the ratio is increased above 0.3, the experiments have shown that the corrosion of several candidate superheater tube alloys is reduced at temperatures as high as 500°C. The limitations on this behavior and differences with industrial experience are discussed.

7.2 Introduction

MSW and biomass also have significantly lower quantities of sulfur when compared to other fossil fuels such as utility coals. Table 7-1 presents typical ranges of sulfur content for utility coals, various biomass feedstocks, and MSW. The sulfur content of MSW is generally about an order of magnitude less than other sources. Table 2-1 in chapter 2 showed that the vast majority of sulfur in MSW is found in textiles and rubbers.

Table 7-1. Sulfur content of various solid fuels [116,117].

Fuels	Subcategory	Sulfur (Percent)
Biomass	poplar wood	0.01-0.03
	switchgrass	0.07 - 0.11
	yard wastes	0.1-0.3
Fossil Fuels	coal (low rank; lignite/sub-bituminous)	1.0 - 3.0
	coal (high rank bituminous/anthracite)	0.5 - 1.5
	oil (typical distillate)	0.2 - 1.2
Municipal Solid Waste		0.05-0.1

In general, sulfur bounded in solid fuels is present in one of three forms, pyritic, organic, and or sulfate [1]. Specifically regarding MSW combusted with excess air, the likely sulfur compounds liberated into the boiler consist of oxides and sulfates. SO_2, sulfur dioxide, is typically the largest form of sulfur present, but can oxidize to SO_3- the thermodynamically favored form below 700°C in the presence of abundant oxygen, as described by equation 7-1.
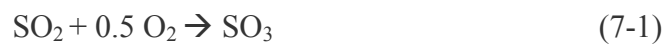
$$SO_2 + 0.5\ O_2 \rightarrow SO_3 \qquad\qquad (7\text{-}1)$$

Table 7-2 indicates the thermodynamic predominance of SO_2 and SO_3. This shows the Gibbs free energy of the conversion of sulfur dioxide to sulfur trioxide. This reaction is thermodynamically favorable at low temperatures up till about 800 °C. It is also well known that the homogeneous oxidation of SO_2 to SO_3 is kinetically limited. It has been suggested that metal oxides present in the boiler as well as in the WTE fly ash from MSW combustion can catalyze this reaction [118,119]. Similar to chlorides, sulfates are typically found in boiler deposits, both in the waterwall and in the superheater. The most common sulfates are either heavy metals such as lead or zinc or alkali/alkali-earth metals such as sodium, potassium, and calcium.

The corrosion at high temperatures attributed to sulfur compounds has been well investigated [120,121]. In addition to reacting with heat exchange surfaces, sulfur compounds can react with chlorine compounds present in the process gas and in the boiler deposits, influencing different corrosion reactions to occur. The following section is a description of the industrial experience between sulfur and chlorine compound which provided the experimental investigation in the rest of this chapter.

Table 7-2. Thermodynamic data of sulfur dioxide oxidation

| SO_2 (g) + 0.5 O_2 = SO_3 (g)	
Temperature (°C)	ΔG (kJ/mol)
300	-90
400	-71
500	-52
600	-33
700	-15
800	3
900	22
1000	40

7.3 Industrial Experience

In the 1970's as part of work commissioned by the Solid Waste Management Office of the US Environmental Protection Agency (US EPA), the Battelle Memorial Institute performed tests to discern the effects of chlorine and sulfur compounds on WTE corrosion. The finding was made that the addition of elemental sulfur with MSW trended with a substantial reduction in boiler corrosion- as determined by corrosion probes [122]. Those results gave rise to a series of tests to investigate the relationship how controlled additions of elemental sulfur, and later co-firing MSW with high-sulfur coals, affected boiler corrosion.

Table 7-3 demonstrates the results obtained from the corrosion study of two metal tube alloys (carbon steel A10 and stainless steel 316) following 1000 hours inside the boiler. The alloys were a part of corrosion probes- consisting of alloys rings fixed to a hollowed tube to allow for air flow. The air flow was designed to control the metal rings to an average temperature within the ranges of operating superheater tubes. The corrosion rate was determined by the thickness loss measured in the alloy rings after 1000 hours, and normalized to a reference condition- which was the combustion of raw refuse. The rates were plotted as a function of the SO_2/HCl, which demonstrate the addition of sulfur into the furnace. These studies concluded that at investigated temperature 370 °C and 593 °C--the addition of sulfur yielded a lower corrosion rate. These results have served as the motivation for various approaches to mitigate chloride corrosion that are discussed in chapter 3.

Table 7-3. Corrosion rate of alloys measured in Battelle plant test (mils/hour) [123]

Carbon Steel					SS310 (25 Cr 20 Ni)			
SO$_2$/HCl	370°C	482°C	593°C		SO$_2$/HCl	370°C	482°C	593°C
0.3	0.28	0.33	0.55		0.3	0.04	0.14	0.23
1.5	0.22	0.25	0.32		1.5	0.02	0.03	0.03

To understand the effect on the tube thickness, the deposition on the alloys rings was analyzed via XRD and identified that smaller corrosion layers were observed under sulfate deposits. The hypothesis is that the presence of sufficient SO$_2$ in the furnace atmosphere, the sulfation of metal chlorides would occur. A general expression of the sulfation reaction is shown below in equation 7-2.

$$2MCl_{(s,g)} + SO_{2\,(g)} + 0.5\ O_{2\,(g)} + H_2O_{(g)} \rightarrow M_2SO_{4\,(s)} + 2HCl \qquad (7\text{-}2)$$
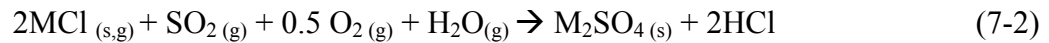
In the remainder of this chapter, laboratory experiments demonstrate the phenomena between sulfur and chlorine compounds in WTE superheaters. The objective is to elucidate the behavior of sulfur injection as a method for mitigating high temperature chloride corrosion. Several factors are examined, including the effects of deposit, temperature, alloy scale with respect to the SO$_2$/HCl ratio.

7.4 The effect of the sulfate layer

Furnace tests were performed to distinguish the different corrosion behavior of alloys under synthetic boiler tube deposits at superheater conditions. Pure compounds were used to investigate the behavior related to compounds, groups of compounds commonly found in boiler

deposits. Sodium sulfate was applied on coupons of SA 178A (carbon steel) and NSSER-4 (17 Cr-13 Ni-Fe) at the same loading (4.0 mg/cm^2 ±10%) which was tested in chapter 5 and 6. Sodium sulfate was utilized in these experiments since sodium chloride was chosen as the surrogate metal chloride compound, as sodium sulfate would be the expected compound if sodium chloride were to undergo a sulfation reaction. The coupons were subjected to a typical WTE gas mix with SO$_2$/HCl =0.3 at a temperature of 500°C for 24 hours.

Figure 7-1 displays the mean mass loss of six coupons of SA178A and NSSER-4 under following the furnace tests. The mean mass loss of NSSER-4 is shown magnified by a factor of 10 to be visible on the same axes as the carbon steel specimens. The mass loss of the sulfate covered coupons had a mass loss similar or slightly higher than the coupons exposed to the gas environment and was about an order of magnitude smaller than the corrosion rates obtained under a 100% chloride deposit. Examples of NSSER-4 from these experiments are shown in figure 7-2. A white residue is present on the coupons which were coated with sodium sulfate, which are the unreacted sulfate. In contrast, the deposited sodium chloride is no longer present on the coupon and a thicker mass change was observed. Given the changes in the corrosion rate, and the observation of the surface, the sulfate layer appears to prevent further corrosion and remain nearly intact on the surface.

The stability of the sodium sulfate layer was obtained by repeating the previous 24 hour tests under the WTE gas over a wide for a range of temperatures. Figure 7-3 shows the mean mass loss of NSSER-4 coated with sodium sulfate following 24 hour experiments at 450°C, 500°C, 550°C, and 700°C respectively. 700°C was utilized as an extreme temperature. The results of NSSER-4 under the sulfate layer are plotted alongside the mass loss of NSSER-4 in the absence of a salt deposit. Between 450 and 500°C the mass loss is nearly identical, and slightly

diverges at 550°C. It is at this temperature the sulfate layer becomes highly corrosive. At 700°C, the sulfate is very aggressive and accelerates the mass loss by more than a factor of 4.
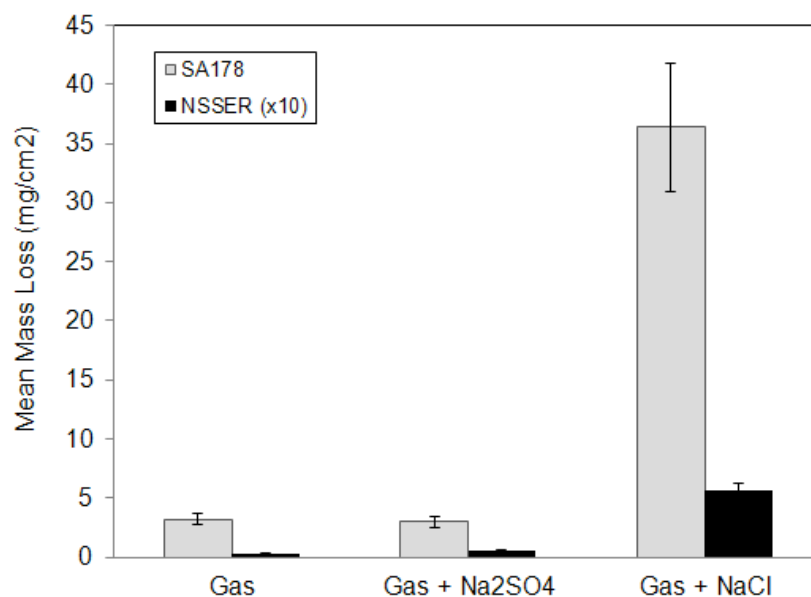

Figure 7-1. Mass Loss of SA178A and NSSER-4 in the presence of WTE flue gas and under NaCl and Na_2SO_4 at 500°C after 24 hours
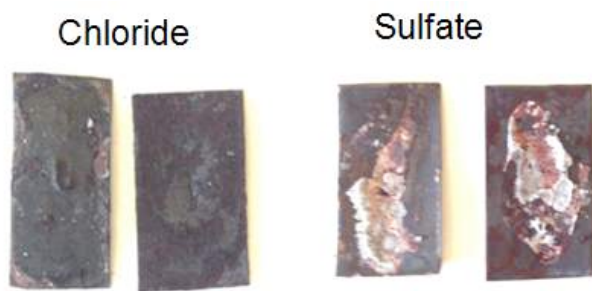

Figure 7-2. NSSER-4 coupons following 24 hour experiments at 500°C under sodium chloride and under sodium sulfate deposits
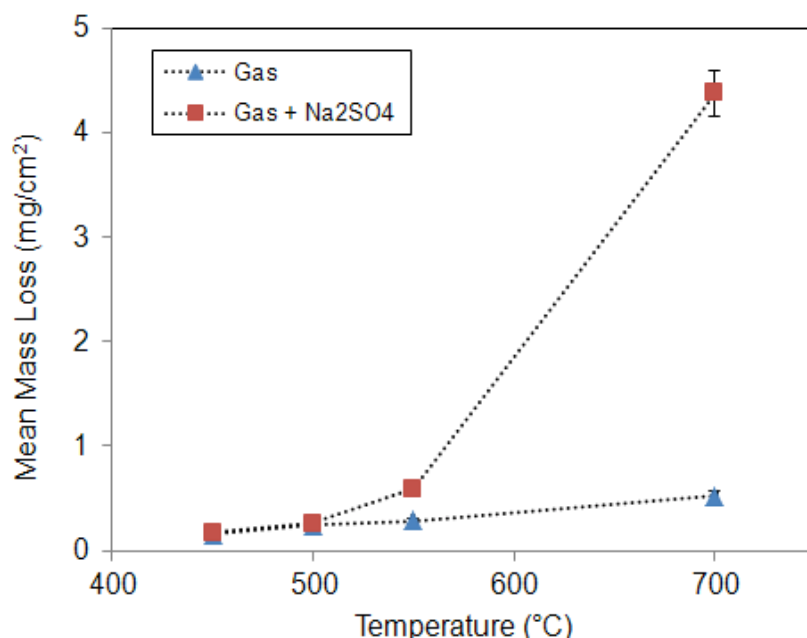
Figure 7-3. Mass loss of NSSER-4 versus temperature (450-700°C) after 24 hour exposure to WTE flue gas and flue gas and Na_2SO_4 deposits

At 550° C and above, the sulfate later no longer provides protection for the coupon surfaces. It has been discussed in chapter 2 that sulfate induced high temperature corrosion is a factor at these temperature due to the formation of pyrosulfates- which can flux oxide layers. [124].

7.5 Tests varying the SO_2/HCl ratio

The relationship between the SO_2/HCl ratio and corrosion of alloys was investigated for several variables: the type of deposit (sulfate, chloride) compared to virgin material, water concentration, temperature, and alloy type. These tests were designed to understand the potential mitigation mechanism(s) that may be occur. Additionally, these tests can be added to the library of how different boiler materials and operating conditions respond to changes in the sulfur/chlorine ratio in the combustion feed.

For all of the experiments discussed in the proceeding sections, the SO_2/HCl ratio was modified by adjusting the SO_2 concentration relative to a constant HCl concentration of 800 ppmv. In doing so modification of the SO_2/HCl ratio would replicate the field test discussed at the beginning of this chapter. Unless otherwise specified (experiments in section 7.5.1), all experiments discussed are 24 hour furnace tests- similar to those discussed in chapter 6.

7.5.1. Effect of different salt layers

In Figure 7-4 the SO_2/HCl concentration is varied between 0.1-2.0 at 500° C for coupons of SA178A. Ratios between 0.1-0.3 can be considered in the range of normal plant operation, whereas higher than 0.3 can be considered sulfur addition. In these initial tests, no deposit (i.e. no salt layer) was applied to the coupons. Similarly the tests were repeated for select ratios at the shorter exposure time of 12.5 hours-to determine whether any variations were visible at smaller scales. The data can be considered a flat line between the varies flue gas ratios, which is to say the average corrosion (mass loss) of the alloys was not impacted by varying the flue gas ratio.
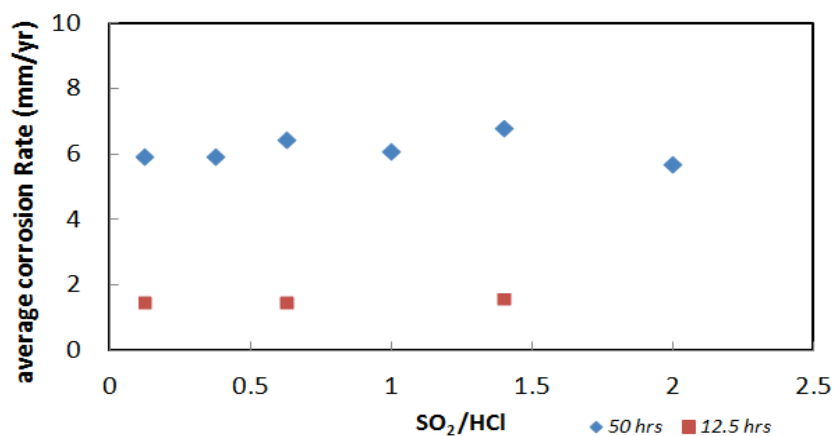

Figure 7-4. Corrosion of SA178A versus SO_2/HCl ratios 0.1-2.0; 500°C and 50 hours

The data in figure 7-4 is consistent with thermodynamic predominance diagrams provided in figure 7-5 and 7-6 respectively. These diagrams consider the thermodynamic equilibrium for a metal in a mixed gas environment at a specified temperature. The diagrams were constructed using *HSC Chemistry* software. Figure 7-6 corresponds to Fe-O-Cl at 500°C and figure 7-7 corresponds to Fe-O-S at 500°C. As SA178A is a low carbon steel, iron is >99 wt% of its composition. Both diagrams indicate that the predominant compound found in the corrosion layer is Fe_2O_3. Fe_3O_4 may be present at lower partial pressures of oxygen, between the corrosion layer and the virgin alloy interface. It is also possible at very low partial pressures, interfacing between Fe_3O_4 and the virgin alloy interface iron sulfides and/or iron (II) chloride.
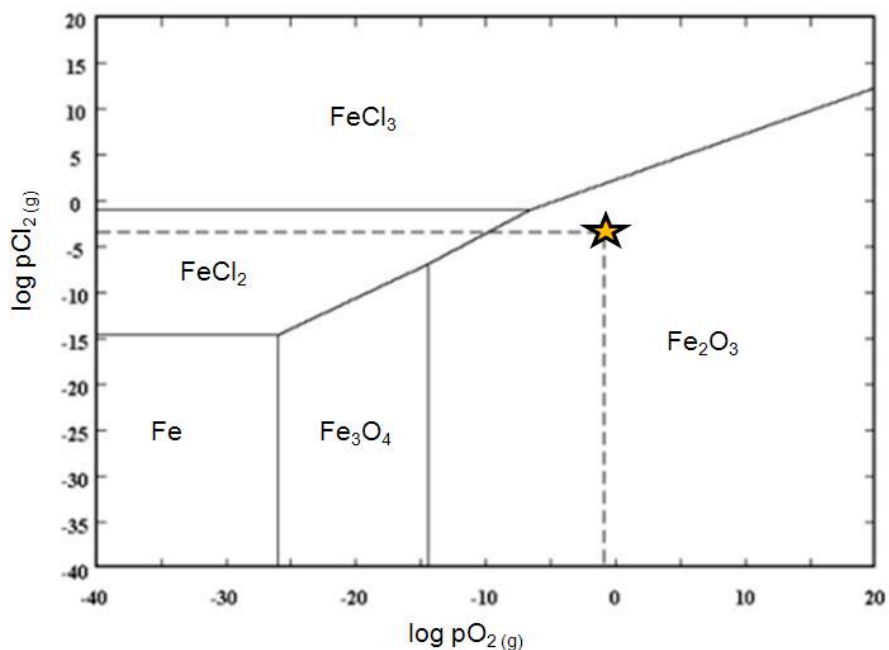

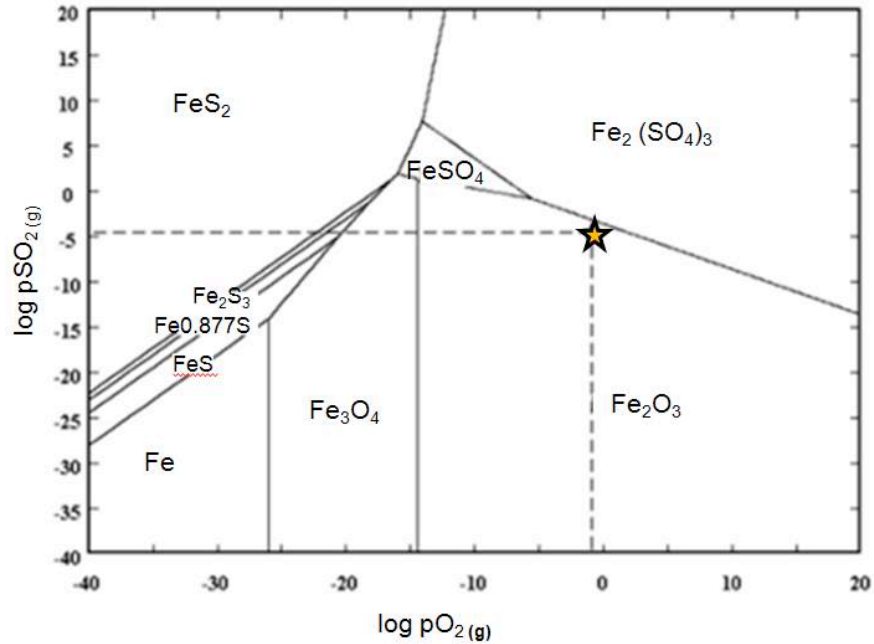**Figure 7-5**. Fe-O-Cl predominance diagram, 500°C

Figure 7-6. Fe-O-S predominance diagram, 500°C

Based on these diagrams, there is no difference in product composition at higher SO_2/HCl. Even as SO_2 is increased and the driving force for SO_2 to diffuse to the oxide-metal interface is also increased, the predominant products will remain the same as long as sufficient oxygen is present. This analysis is confirmed by considering the XRD pattern of the scales generated from SA178A at different SO_2/HCl ratios and comparing. This comparison is shown in figure 7-7.
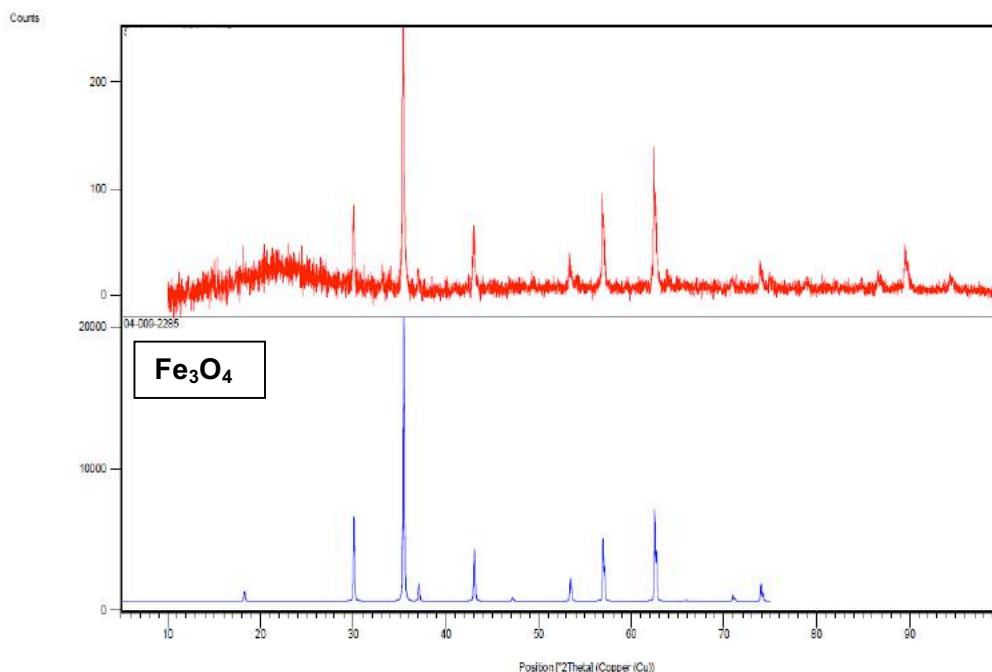
Figure7-7. XRD pattern of scale of T22 recovered after 50 hours

Figure 7-8 shows the average corrosion rate for NSSER-4 at various SO_2/HCl ratios under sodium sulfate and sodium chloride after 24 hours at 500°C. The corrosion rates of the coupons under the sodium sulfate layer are about an order of magnitude smaller than the values under the sodium chloride. The values are invariant with the gas composition. Comparatively the corrosion under the sodium chloride shows a modest, yet discernible decrease at every ratio. The oxide layer is 27% smaller at $SO_2/HCl = 2$ than the layer measured at $SO_2/HCl = 0.1$.

This result agrees with the findings provided in earlier plant studies that the SO_2/HCl is able to suppress the corrosion of alloys under chloride deposits. Furthermore the sulfate layer at 500° C, which has been shown to be relatively inert, maintains this behavior at 500°C as the SO_2 concentration in the synthetic flue gas is varied between 100 ppmv to 1600 ppmv.
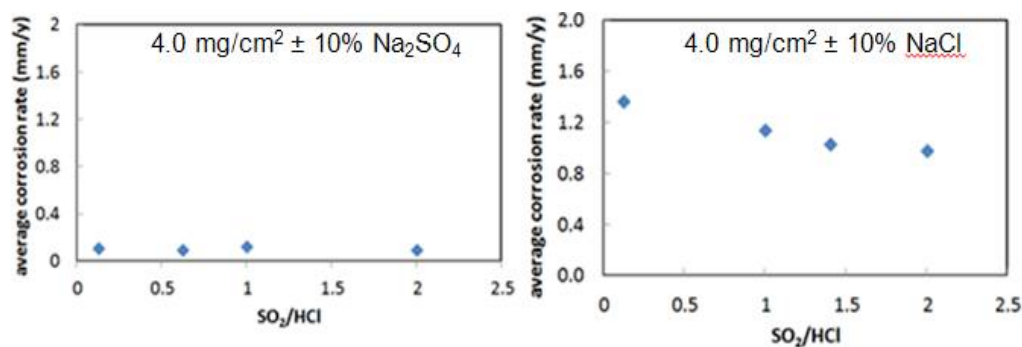
Figure 7-8. The corrosion rate of NSSER-4 vs SO2/HCl at 500 °C under chloride and sulfate layers

Some literature had suggested sulfates in the presence of SO_2 and O_2 at temperatures of 500°C or greater were susceptible to alkali tri-sulfates [125].   Under these conditions, the molten compound can dissolve the protective oxide layer, further accelerating corrosion.

7.5.2 Effect of water

Figure 7-10 shows the corrosion rate of NSSER-4 under a sodium chloride layer in two different gas environments. One data set is the typical gas environment, replotted from figure 7-9 (15% H_2O). The other set is the same experiments performed in an anhydrous (0 vol% H_2O) environment.   The purpose of the study was to determine whether the postulated sulfation reaction of alkali chlorides proceeds as equation 7-3 or as equation 7-4 or both- and whether this has an impact on alloy corrosion rate. Under the anhydrous experiments, the corrosion rate is similar to the reference condition and remains stagnant the same value. Under the moist environment, as mentioned previously the rate is suppressed with respect to an increase in the

SO$_2$/HCl ratio. The findings from figure 7-9, coupled with literature suggest that conversion of alkali chlorides follows equation 7-3, that is sodium forms a sulfate and releases HCl gas.
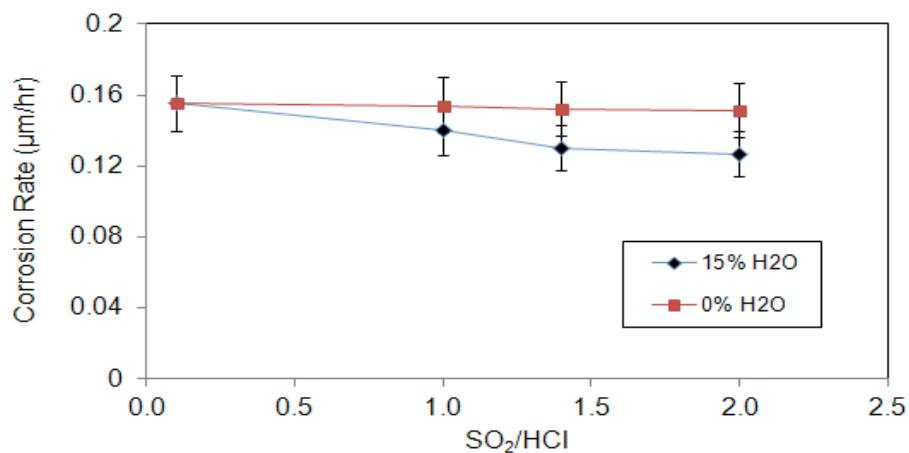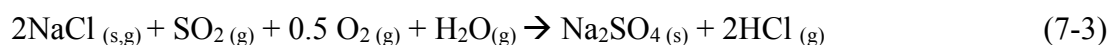

Figure 7-9. The corrosion rate of NSSER-4 under a NaCl layer vs. the SO$_2$/HCl ratio at 500°C; the effect of water vapor

$$2NaCl_{(s,g)} + SO_{2\,(g)} + 0.5\;O_{2\,(g)} + H_2O_{(g)} \rightarrow Na_2SO_{4\,(s)} + 2HCl_{(g)} \qquad (7\text{-}3)$$

$$2NaCl_{(s,g)} + SO_{2\,(g)} + O_{2\,(g)} + \rightarrow Na_2SO_{4\,(s)} + Cl_{2(g)} \qquad (7\text{-}4)$$

Previous literature has investigated the sulfation reaction under anhydrous conditions at temperatures between 100-650°C. Different products were formed on the NaCl surface at different ranges of temperature and Cl$_2$ was detected in the gas phase. Experiments in the presence of water vapor yielded the expected products of Na$_2$SO$_4$ and HCl [126].

7.6 Effect of SO$_2$/HCl ratio on various alloys under chloride salt layer

In chapter 6 an alloy comparison was made among multiple candidate superheater materials and tube coatings. In this chapter the comparisons between those materials are continued, focusing on the influence of the SO$_2$/HCl ratio on the high temperature corrosion behavior.

Figure 7-10 are initial results with the materials that were investigated in the previous studies. These results demonstrate the relationship between the corrosion change and the SO$_2$/HCl are not the same for each alloy. A much steeper effect (an 80% decrease) was observed for the carbon steel as compared to NSSER-4 (27%) over the entire range. Whereas the corrosion rate continues to drop up to SO$_2$/HCl = 2 for the carbon steel, the profile appears to plateau for NSSER-4 after SO$_2$/HCl = 1.4.
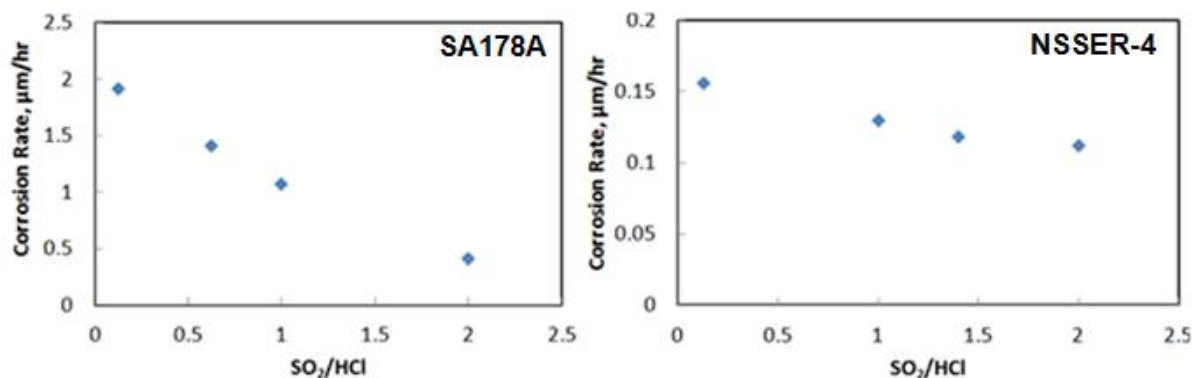

Figure 7-10. Corrosion rate of SA178A and NSSER-4 vs. SO2/HCl ratio at 500 °C

For the remainder of the comparative alloy study, three SO$_2$/HCl ratios and three temperatures were chosen. SO$_2$/HCl ratios of 0.3, 0.6, and 1.0 were chosen as the median range of those investigated in the preliminary tests. It was determined that within this range, a trend

would be discernable because of the industrial experience increasing the sulfur/chlorine ratio as similar levels. The temperatures of 450°, 500°, and 550°C were chosen as a way of complementing the analysis discussed in chapter six.

A plot of the mass loss per area for SA213 T22 (Fe-2.25Cr-1Mo) under a sodium chloride layer versus the SO_2/HCl ratio is shown in figure 7-11. At 450°C and at 500 °C (the bottom 2 lines) positive trends are observed. The largest change occurs at 450°C between SO_2/HCl = 0.3 to 1.0, a 38% reduction. At 500°C, the rate drops to 28% within those same conditions. At 550°C, no relationship was defined- as the change was within experimental error.
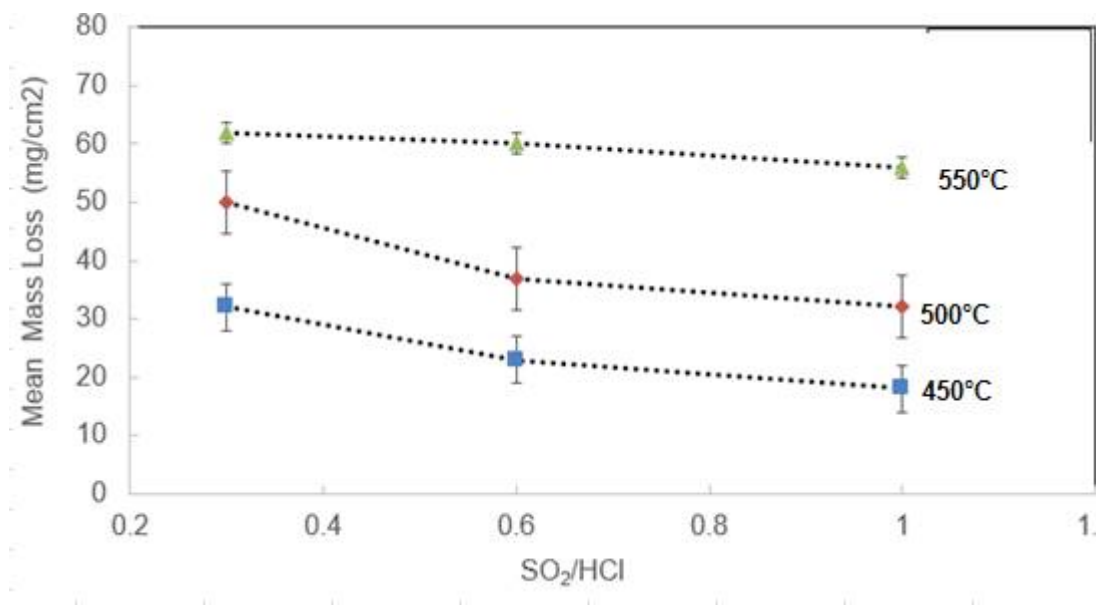

Figure 7-11. The effect of SO_2/HCl on the mass loss of SA 213 T22 at 450°, 500°, 550° C.

Inconel 625 laser weld on T22 is shown in figure 7-12. As shown in chapter 6, Inconel reduces the mass loss obtained from post-test analysis by nearly 50%. Similarly to T22, Inconel exhibits a trend at 450°C between SO_2/HCl = 0.3 to 1.0, a 38% reduction. At higher temperatures

however the trend is indistinguishable. The most different behavior of the materials investigated belongs to HVOF applied Colmonoy 88 which did not demonstrate any trend. The rates for Colmonoy88 are comparatively much lower than any of the materials investigated in this study-but were still measurable within the sensitivity of the laboratory equipment.
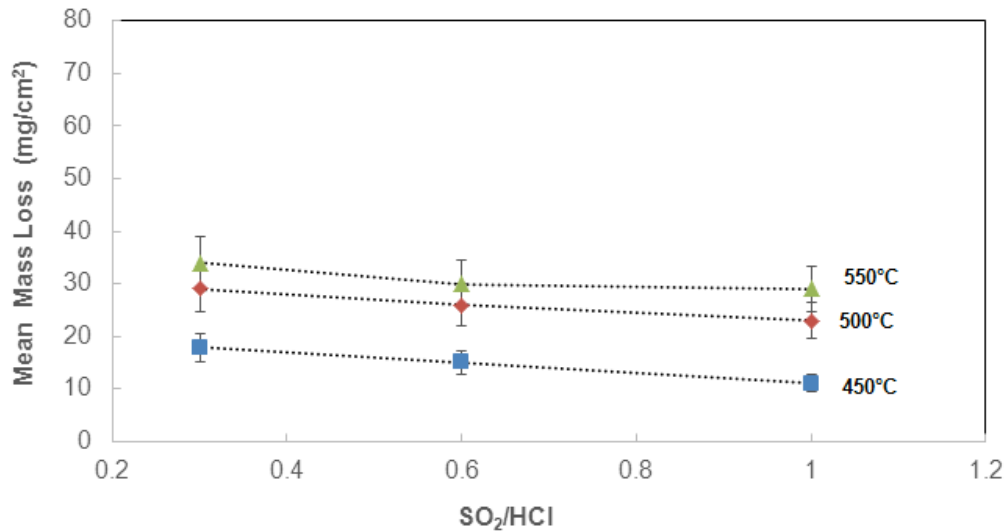

Figure 7-12. The effect of SO_2/HCl on the mass loss of Inconel 625 at 450°, 500°, 550° C.
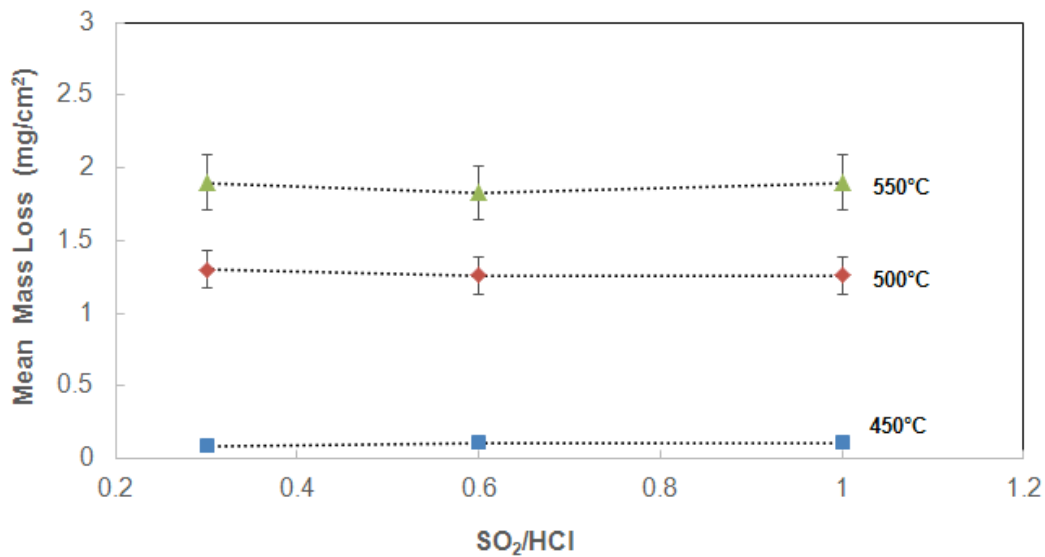

Figure 7-13. The effect of SO_2/HCl on the mass loss of Colmonoy 88 HVOF at 450°, 500°, 550° C.

There are several insights that can be discussed from the tests of the different alloys at the different temperatures. The first is that increasing SO_2/HCl appears to that have greater impact on alloys with higher corrosion rates. SA178A and T22 corrosion were the most sensitive to changes to the ratio. NSSER-4 and Inconel 625 with moderately high corrosion had measurable, yet smaller sensitivity to the ratio, whereas Colmonoy88 had none.

One possible explanation for the sensitivity could be attributed to the alloys surface and whether sulfation was promoted by different metals. This was refuted by comparing the salt surface of the Inconel 625 (figure 7-14) and stainless surface (figure 7-15) respectively as shown with accompanying EDS analysis. The images reveal the salt layer present on the surface of the coupon following the 24 hour experiment. For both alloys the EDS measurement indicates no presence of chloride on the surface and a significant concentration of sulfur- suggesting that the layer on the surface has completely reacted with the gas environment. Considering the alloying content the trend cannot be attributed solely to one metal on the surface.

Another interesting observation is that the sodium chloride was not expected to completely react to sodium sulfate under these tests after 24 hours. Previous literature on the sulfation of solid sodium chloride at 500 C for an SO_2 partial pressure of 0.0003 atm predicted a conversion of 8% at 450 °C, 16% at 500 °C, and 19% at 550 °C [127]. Those experiments were conducted in a flow through reactor with NaCl placed on a porous quartz glass support. In the case of these experiments, either iron, chromium or nickel oxide supported the sodium chloride. Another important observation is that although there were different corrosion trends with the SO_2/HCl at different temperatures, this was not impacted by the presence or lack of the sodium sulfate on the surface. Figure 7-16 show the images of the salt layer on SW 1600, another Ni coating, at each temperature. In all the cases, the surface chloride concentration was negligible

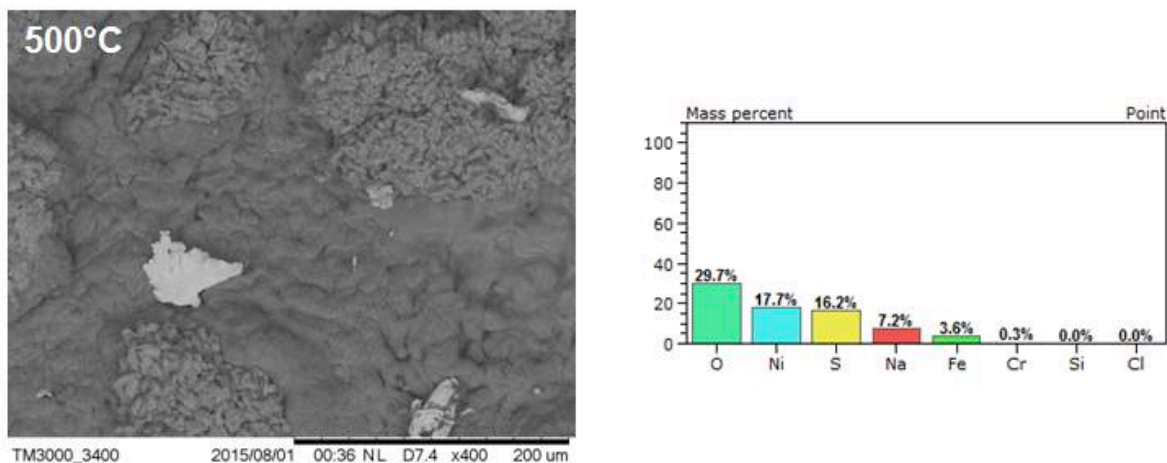after 24 hours. That does not suggest however that the chlorides not participate in the alloy corrosion.

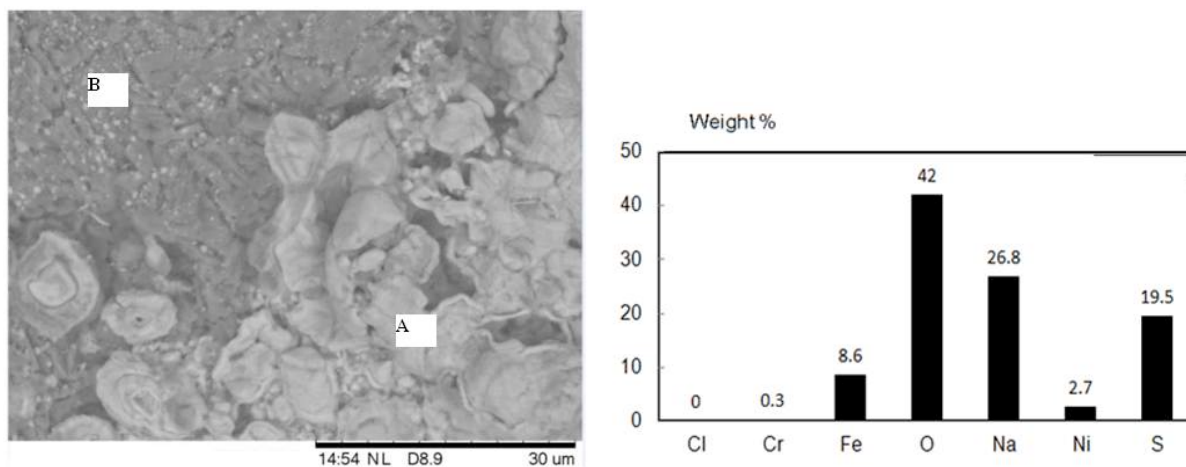**Figure 7-14.** Salt coverage and EDS values for Inconel 625 after 24 hour tests at $SO_2/HCl = 0.3$

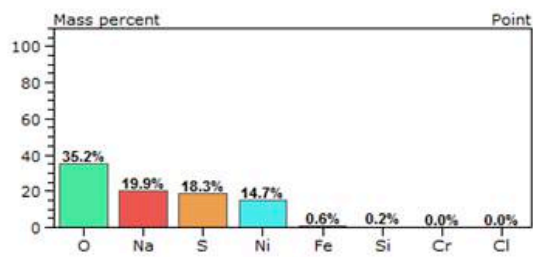**Figure 7-15.** Salt coverage and EDS values for NSSER-4 after 24 hour tests at $SO_2/HCl = 0.3$

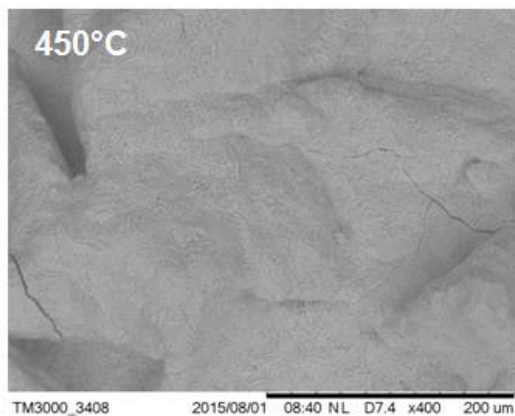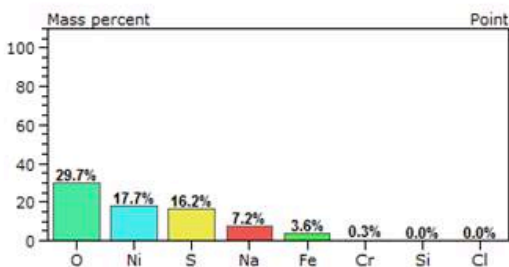**Figure 7-16 (a).** SEM- EDS values for SW1600 at SO_2/HCl = 0.3, 450°C

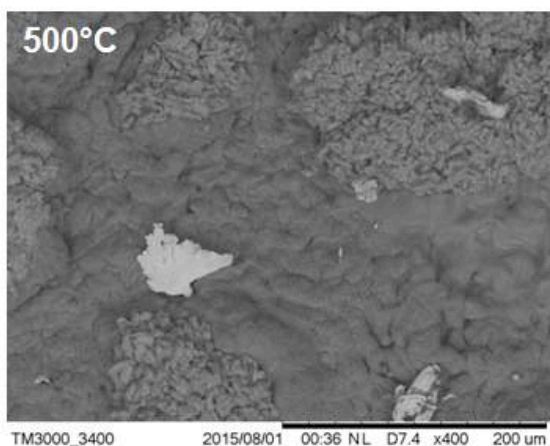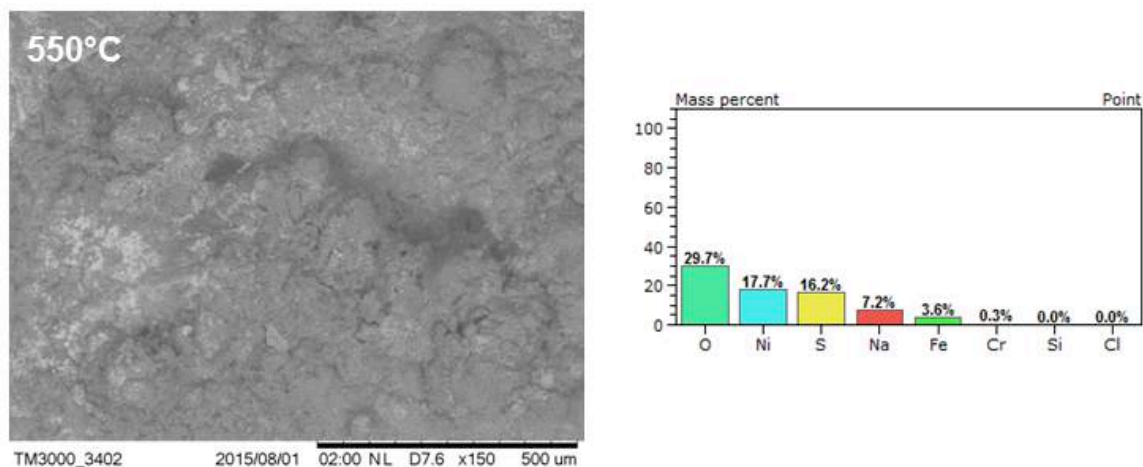**Figure 7-16(b).** SEM- EDS values for SW1600 at SO_2/HCl = 0.3, 500°C

Figure 7-16(c). SEM- EDS values for SW1600 at $SO_2/HCl = 0.3$, 550°C

The images in figures 7-17 (a-c) are the cross section taken for a nickel overlay on T22, after 24 hours furnace tests at 450 °C and 550°C respectively for $SO_2/HCl = 0.3$ The images are couples with EDS mapping to show the presence of individual elements displayed in the image. The substrate T22 is not shown in the images- only the coating, corrosion layer, salt layer and resin-used to preserve the corrosion layer for cross section.

At each temperature the salt layer is visible, indicated by the presence of sodium. This is most noticeable at 450 C, where the least corrosion has occurred. In the area marked by sodium, sulfur and oxygen is co-present, reflecting the EDS data shown for the surface in figures 16 and 18 respectively. Below the deposit, the cross section demonstrates large fissures in the coating which looks characteristically like the diffusion observed with chlorine. These fissures occur in areas on the coating where chromium is present. At 450° and 500°C, chlorine is not present in the fissures, but sulfur and oxygen. At 550°C however, chlorine is present where the largest fissures are present, along with sulfur, oxygen, and chromium. The chlorine is detected below

116

sodium and below sulfur. The detection of chlorine at higher temperatures may suggest why the SO$_2$/HCl did not have an impact at 550 °C.

The images at 550° C, may also explain the discrepancy between the laboratory data and field data. In section 7-3, it was reported that increases in the SO$_2$/HCl were effective in reducing corrosion in WTE power plants as high for boiler tubes as high as 593 °C. In the plant, sulfur is co-fired with MSW allowing for the sulfation of chlorides in the gas phase, prior to condensing and reacting with boiler tubes. In the case of the laboratory, the chlorides are initially present on the alloy surface and can equally participate in corrosion or sulfation reactions. The data suggests that the chloride-metal oxide reactions may be faster than the sulfation reaction at 550° C.

7.7 Conclusions

Experiments have shown that sulfates are semi-protective on WTE boiler tube surfaces up to temperatures of 550°C. The mass loss for carbon steel and Fe-17Cr-13Ni (NSSER-4) under sodium sulfate had an order of magnitude less corrosion than under sodium chloride. Using this behavior, the SO$_2$/HCl ratio in the synthetic flue gas was increased from 0.3 to 0.6 and 1.0 respectively to determine the impact on sodium chloride corrosion. The surface of coupons was readily converted from chlorine to sulfur demonstrating the effect of SO$_2$. As the ratio is increased above 0.3, the experiments have shown that the corrosion of several candidate superheater tube alloys is reduced at temperatures as high as 500°C. The impact of sulfating the alloy was observed most prominently with alloys that were aggressively corroded by the chloride layer. At 550 °C, there was no trend with respect to increases of the ratio, which suggest that other corrosion reactions, faster than the sulfation reaction, govern the corrosion rate.

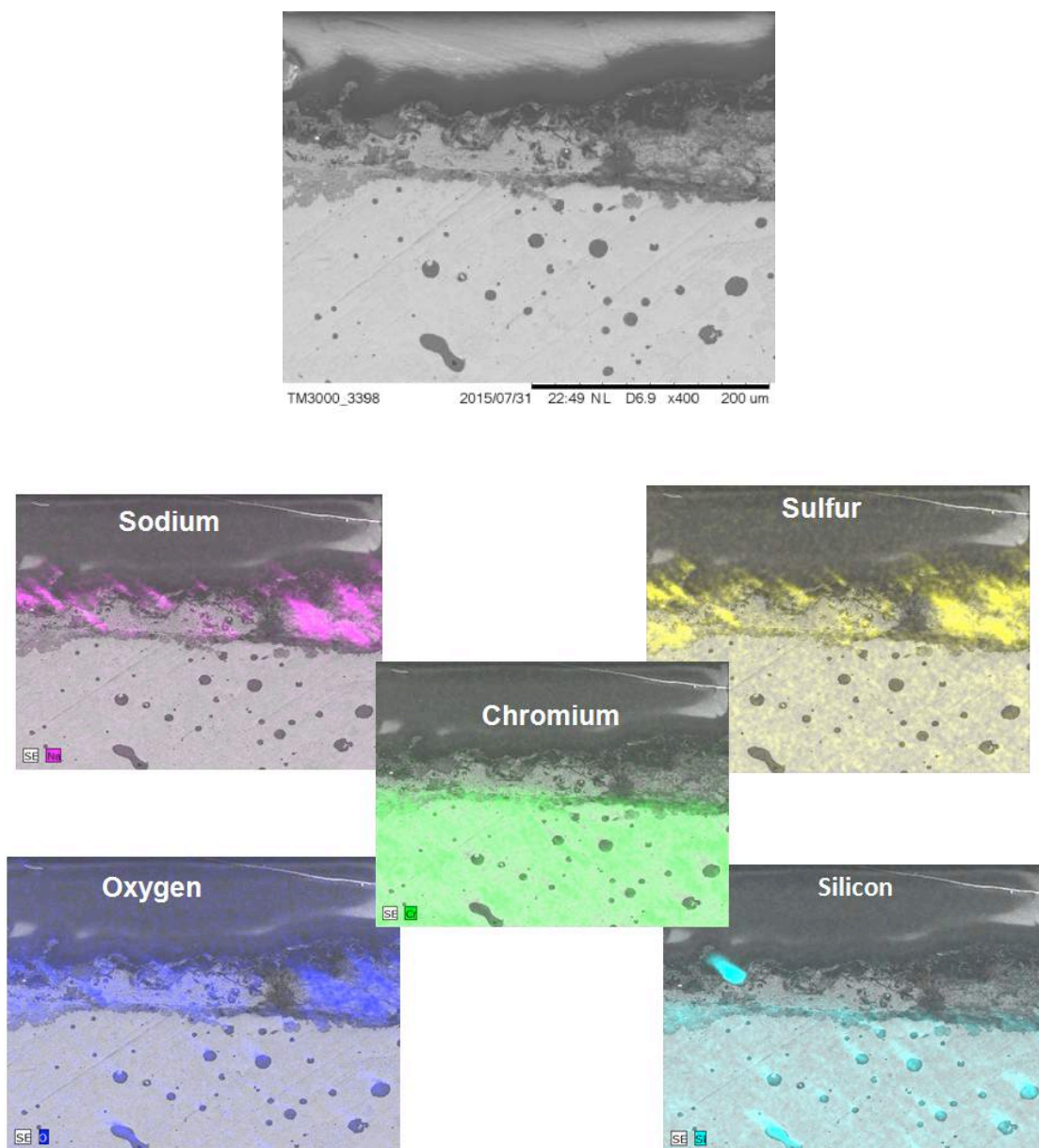**Figure 7-17(a)**. SEM and EDS Mapping for SW1600 at 450°C , $SO_2/HCl = 0.3$

Notes: The elemental fingerprint of sodium and sulfur are in the same locations in this cross section maps. The presence of chlorine was not detected. Either it was not present at all (total conversion of chloride to sulfate) or chlorine is present at such a low amount it was in the noise of the EDS data.
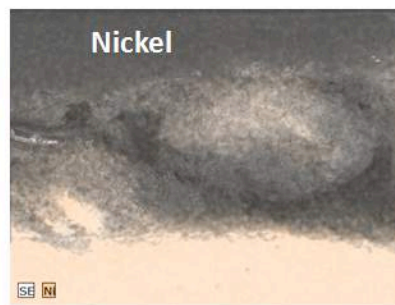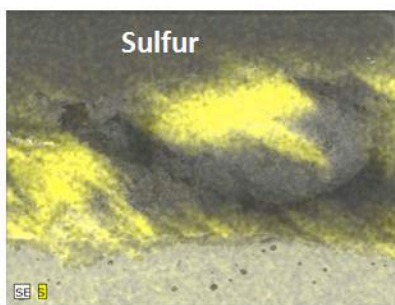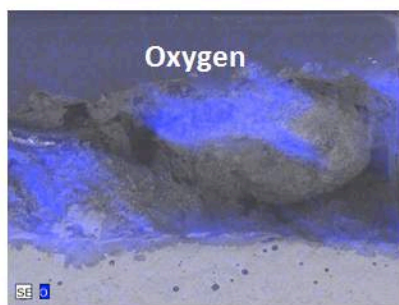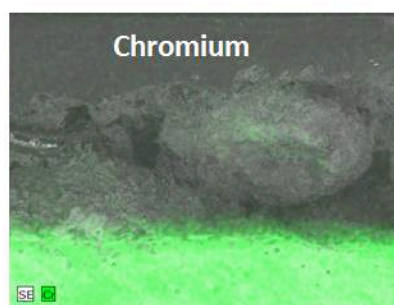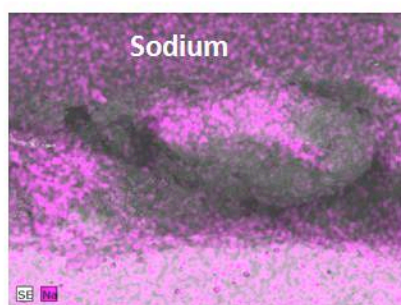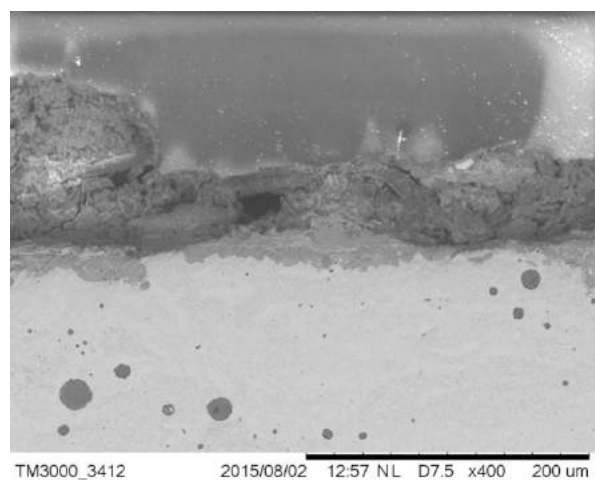
Figure 7-17(b). SEM and EDS Mapping for SW1600 at 500°C , $SO_2/HCl = 0.3$

Notes: Similar to the 450°C map, sodium and sulfur are the present on surface with no Cl present. The oxidize layer under sulfate appears rich in chromium.
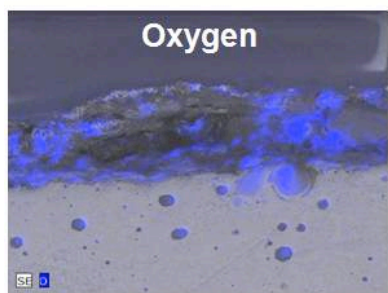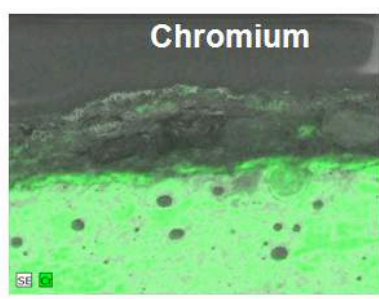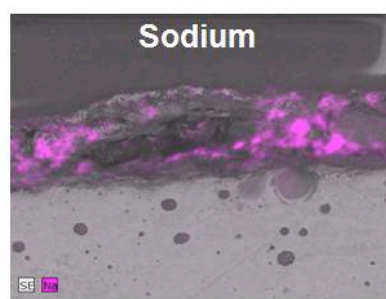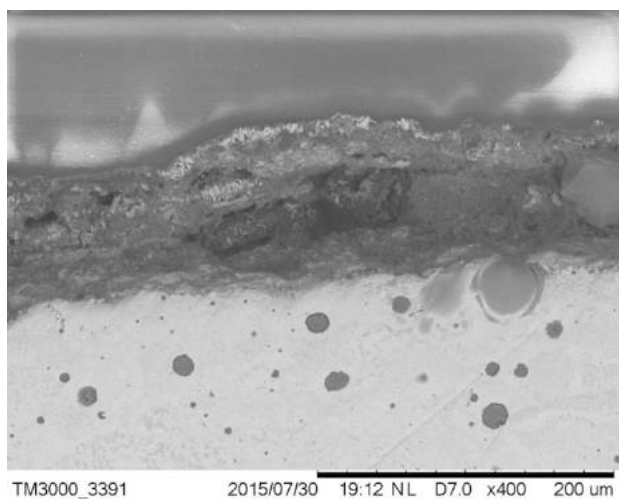
Figure 7-17(c). SEM and EDS Mapping for SW1600 at 550°C , SO_2/HCl = 0.3

Notes: There is considerable sulfur present, but chlorine is also present below the sulfur and below the sodium and it is residing with oxygen and chromium

Chapter 8: Economic Impacts of Corrosion Mitigation

8.1 Introduction

This chapter discusses some of the economic impact that corrosion mitigation can have on a WTE plant. The annualized cost factor is evaluated for the alloys investigated in chapter 6 against a benchmark superheater tube material, SA 213 T22. The analysis is used to iden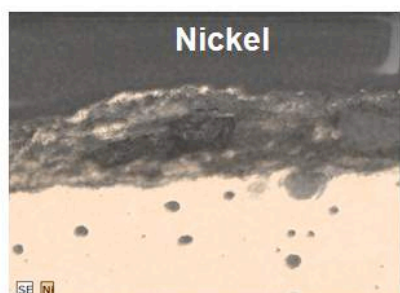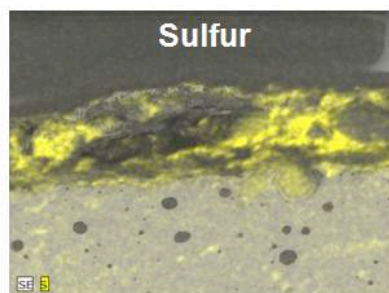tify relative installation costs at which certain materials are feasible. Additional impacts discussed in this chapter include savings from reduced downtime and failure and the price of corrosion additives.

8.2 Annualized cost factor

Generally defined, the annual cost is defined as the payment of owning and operating an asset over its entire lifetime. The equivalent annual cost (EAC) is calculated by dividing the net present value of the asset (i.e. equipment) over the annuity factor. This type of calculation requires information on installation costs, tax rate, acceptable rate of return, depreciation, and the estimate lifetime of the equipment [128].

Given the competitive nature of the power and WTE industry the information necessary to calculate the equivalent annual cost, specifically the installation costs, are not readily available. Instead, an less accurate but convenient method can be applied to distinguish the economic feasibility of using one type of material in a superheater over another by calculating the annualized cost factor- which is presented in equation 8-1 below, which is the ratio of a cost

factor and life factors for a given a material. An annualized cost factor less than 1 would make the material an attractive option.

$$\text{Annualized cost factor} = \text{cost factor/life factor} \qquad (8\text{-}1)$$

The cost factor considers the purchase price of a material and labor cost for installation. Some examples of typical cost factors are shown below. The cost factors are relative to a benchmark material, which in the case of superheater boiler tubes is SA 213 T22--which was been heavily investigated in this work. For example, a cost factor of 2.5 for TP 310H means that the cost and installation of a superheater with that stainless steel will be approximately 2.5 times more expensive. Examples of cost factors are shown in Table 8-1 for common utility boiler alloys TP 310H and Inconel 625 [142].

Table 8-1. Examples of cost factor for SH tube alloys [129]

Cost Factors (Relative to SA 213 T22)	
TP 310H	2.5
Inconel 625	2.4

There are additional factor that can be weighed into the cost factor: For example: the cost of a heavy wall superheater is approximately 10% more costly than a normal boiler. In the case of coatings, the cost of laser cladding is approximately 1.6 times the cost of thermal spray [130].

The life factor is defined as the ratio of the wastage rate of a material with the wastage rate of a baseline or benchmark material. Once again, the benchmark material for this evaluation

is SA 213 T22, which also happens to have the highest wastage rate of any material tested in this thesis (equivalent to SA178A).

Using the mass loss data from chapter 6, the life factor is estimated for the coatings investigated in chapter 6 at the lowest and highest temperatures investigated 450°C (842°F) and 550°C (1022°F) and is displayed in Table 8-2. The highest factors belong to HVOF colmonoy 88, which had superior corrosion resistance. Although the cost factors are not known for all of these materials, the information is available for Inconel 625, in table 8-2, and has a CF= 2.4. Using the most conservative life factor (i.e. the life factor at 550°C), the annualized cost factor of Inconel 625 is 1.2. As that value is greater than 1, Inconel 625 is not a desirable material in the environment investigated in chapter 6.

Conservatively, using the value of the laser cladding instead of the HVOF coating, it can also be shown that the installation of a colmonoy 88 protected superheater can be as much as 4.3 times the cost of a T22 superheater tube and be feasible, or approximately 1.4 times the cost of an Inconel 625 superheater replacement.

Table 8-2. Life factor calculated for Ni coatings based on mass loss data

Coating	Life Factor (Relative to SA 213 T22)	
	450°C (842°F)	550°C (1022°F)
Inconel 625	1.7	2
Colmonoy 88 (HVOF)	110	21
Colmonoy 88 (laser)	7.7	4.3
SP 99	6.1	3.5
SW1600	3.1	1.2
SW1641	1.0	1.1

8.3 Savings from extended tube lifetimes

An estimation of the costs associated with a given forced outage was published in the ASME CRTD Vol 38 report for Waste Incineration plants. The calculation can be using some simplifying assumptions, which are listed below [131].

The cost of a forced outage

The cost of forced outage has several factors. The minimum time required to repair a failed tube, provided that the tube location is accessible and the replacement piece is a stock item, is 12 to 16 hours. This time assumes 4 to 6 hours for the boiler to cool down, 4 hours to make the repair, and 4 to 6 hours for hydro-testing the boiler and heat up.

Cost of repairing the failure

Two boilermakers are typically used at an hourly rate each (with overtime) x tb hours on site per outage + cost of materials. The boilermakers are required to be on-site to make preparations, to carry out the repair, and to be available through the hydrotest. It is assumed that the labor necessary for providing access to the failure and performing the boiler operating functions is provided by the normal operating staff, so that their time is not charged to the outage

Buying power, replacement power

The cost of replacement power is calculated as the cost of natural gas required to augment the firing of the remaining boilers to maintain output.

This is expressed as: *steam flow to be replaced (lb/hr) x enthalpy for operating steam temperature (MBtu/lb) x cost of natural gas (SC/MBtu) x duration of outage (hr)]/[utilization efficiency (e)].*

Based on the model used by Joyner and Lai [132], it can be estimated that a WTE plant spends about $170,000 per failure. Using the life factor in table 8-2, the potential savings by replacing SA213 T22 with other materials is shown in figure 8-1 for a three-year period. For example, since the corrosion resistance of Inconel 625 is a factor of 2 better than the resistance of SA 213 T22, it assumed that the frequency between failures will also double. Based on these assumptions it can be shown that installation of a colmonoy 88 coated boiler can save about $130,000 year in avoided costs

8.4   Corrosion Additives

Another consideration is the use of corrosion additives to mitigate corrosion- such as the addition of a sulfur containing chemicals, to increase the SO_2/HCl ratio.   There are a few technologies that are either operating at commercial scale, such as the ChlorOut[TM] ammonium sulfate based additive by Vattenall or the sulfur recirculation technology by Gotaverken Mijo The commercial scale for Chlorout is predominantly for biomass fired plants, 50 MWe or smaller, which have a higher alkali content in their feed and have significant alkali chloride corrosion issues.
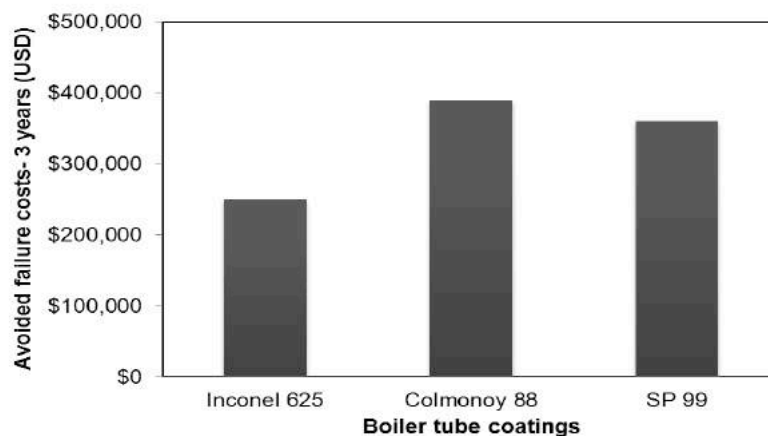
Figure 8-1. Estimated avoided costs by replacing SA 213 T22 with nickel based boiler coatings (three year calculation)

For this exercise, the optimistic assumption is made that a new additive cannot exceed the annual plant cost toward on corrosion maintenance. Table 8-3 shows the corrosion maintenance cost of several WTE power plants from a WTERT survey in 2004, corrected for inflation in 2016 dollars. Normalizing the cost with the tonnage of waste burned annually (tonnage of waste/day x days of annual operation), the value is estimated (in 2016 dollars) at $1.68 per ton MSW combusted. It should also be considered that the cost for the extra $Ca(OH)_2$ needed to remove the excess SO_2 would be $0.21/ton combusted. This assumes that the sulfur dosage would increase the SO_2 concentration in the boiler by a factor of 3 and that the cost of lime is $30/metric ton. Correcting for the cost of the additional sulfur removal and the acceptable cost of the corrosion additive would need to not exceed $1.47 ton of MSW combusted. Depreciation cost of any additional infrastructure and the variable cost of the additive should have to compete with this value.

Table 8-3. Cost of maintenance reported by 7 WTE power plants 2004 WTERT Survey on Boiler Corrosion [145]

	Surveyed WTE Plants (2004 WTERT Survey)						
	A	**B**	**C**	**D**	**E**	**F**	**G**
corrosion maintenance ($/year)	50000	100000	18000	145000	253000	320000	99120
Capacity (ton MSW day)	255	250	242	460	608	250	264
Days of operation (per year)	330	346	327	332	306	328	344
Cost/ton combusted ($/ton)	0.59	1.16	0.23	0.95	1.36	3.90	1.09
Average	**$ 1.33**						

8.5 Conclusions

This chapter discussed some of the economic impacts from the corrosion testing performed in previous chapters. The annualized cost factor was defined and discussed as a way of justifying replacement of expensive, yet more corrosion resistant alloys. The corrosion resistance of coating colmonoy 88 and SP 99 can be attractive options if costs are not prohibitive. Based on its relative corrosion performance colmonoy 88 can afford an installation cost as much as 4.3 times the cost of a T22 superheater tube or approximately 1.4 times the cost of an Inconel 625 superheater replacement, and be economically feasible.

Chapter 9: Conclusions and Suggestions for Future Work

9.1 Conclusions

Waste-to-energy is the environmentally preferred approach for managing post-recycled wastes. One of pressing issues related to waste-to-energy technology is the problem of high temperature corrosion in boilers. The combustion of municipal solid wastes produces a highly corrosive environment which can react with, and deteriorate, heat transfer surfaces. Chlorine, which is readily present in MSW (0.47-0.72 wt%), has been identified as the important corrosive species.

The experimental work discussed in this thesis investigated the corrosion behavior of chlorine in waste-to-energy boilers, with specific interest on superheater tubes. The goal of this research was to provide solutions which can enable WTE operators to reduce frequency of corrosion related shutdowns and operate at higher steam temperatures, thus increasing electricity production. This was achieved through furnace experiments designed to replicate the fireside corrosion environment of WTE boilers, with a synthesized flue gas and chloride deposits at temperatures between 450-550°C (842-1022°F). The behavior was investigated for three commercial steels: carbon steel (Fe-0.1 C), low alloyed steel (SA 213 T22), an austenitic steel (Fe-17.1Cr-13Ni), and 6 different nickel coatings applied on SA 213 T22.

The introduction of 800 ppmv of hydrogen chloride in flue gas increased the parabolic rate constant (0-72 h) of SA178A from 0.18 to 1.7 μm^2/h. This was caused by the active oxidation mechanism- in which the metal forms non-protective, less adherent oxide. This mechanism was inferred through a combination of physical observation, product characterization

via XRD and EDS, and agreement with thermodynamic calculations. The active oxidation affected by hydrogen chloride can be mitigated by replacing iron with chromium and nickel, as was demonstrated with NSSER-4 (Fe-17Cr-13Ni), which had an apparent activation energy (53 kJ/mol), that was half the apparent activation energy of the carbon and low alloyed steels (110-111 kJ/mol).

Another important chlorine compound in WTE boilers are chloride salts, which are readily contained in fly ash. Using sodium chloride as a surrogate compound, the corrosion behavior under chloride salts was investigated by applying a salt layer (4.0 mg/cm^2) on coupon surfaces. Corrosion under the chloride layer was much more severe than under the HCl-containing atmospheres alone. The mass loss for the commercial steels was accelerated by more than an order of magnitude. Based on SEM and XRD coupon and corrosion product characterization, the acceleration of the mass loss was inferred to be caused by another active oxidation mechanism in which the sodium chloride consumes protective or semi-protective oxides. The accelerated corrosion rates were realizable even after 24 hour furnace tests. This observation led to the development of an furnace test which could be used to rank new alloys.

The furnace tests were executed for six different nickel coatings, including Inconel 625 (Ni-Cr-Mo), SW1600, SW1641 (Ni-Cr-Mo-B-Si) and Colmonoy 88 and SP 99 (Ni-Cr-B-W). Colmonoy 88, showed superior corrosion resistance to the chloride environment with mass losses between 0.3-3.1 mg/cm^2 between 450-550°C. The mass loss of the Ni-Cr-Mo, and Ni-Cr-B-So were shown to be significantly higher between 10-30 mg/cm^2 The improved corrosion resistance was attributed to the alloying addition of tungsten, and to a lesser extent molybdenum, which has been shown in other literature to improve the corrosion resistance of pitting corrosion.

Experiments have shown that sulfates are semi-protective on WTE boiler tube surfaces up to temperatures of 550°C. The mass loss for carbon steel and Fe-17Cr-13Ni (NSSER-4) under sodium sulfate was an order of magnitude lower than corrosion under sodium chloride. On the basis of these results, the SO_2/HCl ratio in the synthetic flue gas was increased from 0.3 to 0.6 and 1.0 respectively to determine the impact on sodium chloride corrosion. The surface of coupons was readily converted from chlorine to sulfur demonstrating the effect of SO_2. As the ratio is increased above 0.3, the experiments showed that the corrosion of several candidate superheater tube alloys is reduced at temperatures as high as 500°C. The impact of sulfating the alloy was observed most prominently with alloys that were aggressively corroded by the chloride layer. At 550 °C, there was no trend with respect to increases of the ratio, which suggests that other corrosion reactions were faster than the rate of sulfation.

9.2 Recommendations for the WTE industry

Based on the results of this research, several recommendations can be made for the WTE industry. The first is that colmonoy 88 and SP 99 should be investigated for longer term testing and/or field tests based on their corrosion resistance. It would especially be of interest to determine whether the HVOF application of Colmonoy 88 performs can withstand the erosion and thermal fluctuations that were not simulated in this work. The second recommendation is for WTE plants to explore the installation of sacrificial surfaces – similar to the concept of the chloride trap discussed in chapter 3. The chloride trap is a section of screen tubes, which are maintained in the temperature range of 300-400°C. Low melting ash-typically composed of chlorides-are designed to condense on the walls of the empty pass. The removal of metal chloride deposits would not eliminate the high temperature corrosion attack of HCl but, as shown

in chapter 6, the removal of metal chlorides can reduce the wastage rate of superheater alloys by nearly an order of magnitude. Finally, the third recommendation would be to investigate sulfur additive technologies that would have dual purpose- similar to the "Chlorout" additive discussed in chapter 3, which is used for corrosion mitigation and for NO_x reduction.

9.3 Suggestions for future work

Better understanding of the chlorine cycle (Chapter 5)

Although it is obvious that HCl accelerates the high temperature corrosion of metals, the mechanism is not entirely clear- in particular the diffusion of HCl and metal chlorides. HCl-induced corrosion could be analyzed in more detail with some advanced techniques such as high temperature mass spectroscopy to analyze the different volatile species and quantify their impact on the corrosion attack [132]. More detailed post-exposure analyses such as GDOES, SEM and TEM may be also helpful in understanding the interaction between chlorine and the various alloying elements and how this affects the scale growth.

Behavior of other chloride deposits (Chapter 6)

Laboratory studies investigating alloy performance in the presence of molten and solid chlorides are of great interest. In particular, a comparison can be made on the high temperature corrosion behavior of individual chloride salts such as potassium and calcium chloride with the results of sodium chloride. Furthermore, a test can be developed in which alloys are exposed to a synthetic fly ash mixture that is designed to form a melt at test temperatures. This would allow for short (~24 hour) duration experiments to rank alloys that have been assumed to have excellent corrosion resistance. A mixture of 40 wt% K_2SO_4, 40 wt% Na_2SO_4, 10 wt% KCl, and

10 wt% NaCl would be a possibility as well as mixtures containing heavy metal chlorides such as zinc and lead chlorides, to simulate corrosion for lower temperature superheater tube alloys.

Comparison of metal coating methods (Chapter 6)

This thesis compared the performance of thermal spray and laser cladding of colmonoy 88 on SA 213 T22, and a discernible difference was observed. It would be valuable to compare to the difference between thermally spray and laser cladding coating methods for multiple alloys. This would help optimize both the alloy selection and parameters of the application process. In general HVOF is a cheaper than laser cladding and has a lower heat input. But laser cladding layers have a thicker build up and are considered more robust [133].

The effect of alloying additions of Cr +W + Mo on pitting corrosion resistance

It would be of interested to quantify whether there is a relationship that can be expressed between the corrosion performance under chloride salts and the alloying composition pf nickel-chromium alloys. An empirical value called PREN, Pitting resistance equivalent number, has been developed for pitting corrosion for austenitic steels and nickel alloys in aqueous chloride environment. PREN did fit well with data acquired in chapter 6, but its relevance to other applications is an impetus for a further study. The design criteria for those experiments would be the change in mechanical properties a result of changing the alloy composition.

References

1. Environmental Protection Agency: Advancing Sustainable Management, Assessing Trends in Material Generation, Recycling and Disposal in the United States (June 2015)

2. D. Shin (2014) *Generation and Disposition of Municipal Solid Waste (MSW) in the United States – National Survey* (MS Thesis) Retrieved from Columbia University libraries

3. N. B. Klinghoffer, and Castaldi, M.J. (2013) Waste to energy (WTE): an introduction. *Waste to Energy Conversion Technology* (pp. 3-9) Philadelphia, PA: Woodhead Publishing Limited.

4. N. J. Themelis, Y.H. Kim, and M.H. Brady, Energy recovery from New York City municipal solid wastes. Waste Management & Research, 2002. 20(3): p. 223-233.

5. C. S. Psomopoulos, A. Bourka, and N.J. Themelis, "Waste-to-energy: A review of the status and benefits in USA", *Waste Management* 29 (2009) 1718–1724.

6. N.J. Themelis, N.J., Y.H. Kim, and M.H. Brady, Energy recovery from New York City municipal solid wastes. Waste Management & Research, 2002. 20(3): p. 223-233.

7. Integrated Waste Services Association web site, http://www.wte.org/

8. P. Simmons, N. Goldstein, S. Kaufman, N.J. Themelis, J. Thompson, The State of Garbage, BioCycle, 1 (2006) 26-43.

9. N.J. Themelis, P.A. Ulloa, Methane generation in landfills, Renewable Energy, 32 (2007) 1243-1257.

10. E. Matthews and N.J. Themelis, Potential for reducing global methane emissions from landfills, 2000-2030 in *11th International Waste Management and Landfill Symposium,* Sardinia, 2007.

11. Bogner *et al.,* Mitigation of global greenhouse gas emissions from waste: conclusions and strategies from the Intergovernmental Panel on Climate Change, 4th assessment, *Waste Management and Research,* 2008, 26: 11-32, wmr.sagepub.com/cgi/reprint/26/1/11.

12. American Standard of Testing Methods (ASTM) D866 testing method

13. Energy Information Administration: Energy Explained: Waste-to-energy (MSW) http://www.eia.gov/Energyexplained/?page=biomass_waste_to_energy#tab2

14. C. Ducharme, Analysis of a Thermal Plasma Assisted Waste-to-Energy Processes, 18th North American Waste To Energy Conference (NAWTEC 18) 2010. Florida, USA.

15. S. Goff. (2011). Energy from Waste Retrieved from http://www.seas.columbia.edu/ earth/wtert/sofos/homepage

16. L. M. Grillo (2013) Municipal Solid Waste Combustion Plants *Waste to Energy Conversion Technology* (pp. 3-9) Philadelphia, PA: Woodhead Publishing Limited.

17. J. Gittinger and W. Arvan (1998), Considerations for the design of RDF-fired refuse boilers, presented to *Power-gen Europe* 1998, Milan.

18. C. C. Velzy and L. Grillo, (2007a), Fuels and Furnace, in Avallone, E, Baumeister, T, and Sadegh, A, *Marks' Standard Handbook for Mechanical Engineers,* 11th edition, New York, McGraw Hill, pp. 7-48 – 7-53.

19. C. Velzy and L. Grillo, (2007b), Waste to energy combustion, in Kreith F and Goswami, D, *Handbook of Energy Efficiency and Renewable Energy,* Boca Raton, CRC Press, pp 24-1 – 24-42.

20. F. Rinaldi and B. Najafi, "Temperature Measurement in WTE Boilers Using Suction Pyrometers" *Sensors* 2013, 13, 15633-15655.

24. Albina, D.O., K. Millrath, and N.J. Themelis. Effects of Feed Compositions on Boiler Corrosion in Waste-to-Energy Plants. in 12th North American Waste To Energy Conference (NAWTEC 12). 2003. Florida, USA.

21. P. R. Roberge, P.R., Handbook of Corrosion Engineering. 2000: Mc Graw Hill.

22. D.N. French, *Metallurgical Failures in Fossil Fired Boilers,* 2nd ed., John Wiley & Sons Inc.

25. S.H. Lee., N. J. Themelis, and M. Castaldi, High-Temperature Corrosion in Waste- to-Energy Boilers. Journal of Thermal Spray Technology, 2007. 16(1): p. 104-110.

26. N.J., Themelis, Chlorine Balance in a Waste-To-Energy Facility. 2005, Earth Engineering Center.

27. A.S. Khanna (2002), High Temperature Oxidation and Corrosion, ASM International

28. Jones, D.A., Principles and Prevention of Corrosion, 2nd Edition, Upper Saddle River, NJ Prentice Hall 1996

29. P. Koftsad (1988), High Temperature Corrosion, Elsevier Applied Science, London

30. P. Viklund, (2011), PhD Thesis, KTH

31. C. Wagner, Journal of the Electrochemical Society 103, p.627-633 (1956)

32. R. Roberge, P.R., Handbook of Corrosion Engineering. 2000: McGraw Hill.

33. A.S. Khanna (2002), High Temperature Oxidation and Corrosion, ASM International

34. C. Wagner, Corrosion Science 9, p.91-109 (1969)

35. P. Viklund, "High Temperature Corrosion during Mass Incineration, " (2011), PhD Thesis, KTH

36. P. Rademakers, W. Hesseling and J van de Wetering, "Review on Corrosion in Waste Incinerators, and possible effects of bromine." TNO Report, 2002

37. S.H. Lee., N. J. Themelis, and M. Castaldi, High-Temperature Corrosion in Waste- to-Energy Boilers. Journal of Thermal Spray Technology, 2007. 16(1): p. 104-110.

38. J. Pettersson, C. Pettersson, N. Folkeson, L.-G. Johansson, E. Skog, J.-E. Svensson, Materials Science Forum 522-523, p.563-570 (2006)

39. Y. Kawahara, Corrosion Science 44, p.223-245 (2002).

40. H. J. Grabke, E. Reese and M. Spiegel, Corrosion Science 37, p.1023-1043 (1995).

41. A. Zahs., Spiegel, M. and Grabke J.H, " Chloridation and oxidation of iron, chromium, nickel and their alloys in chloridizing and oxidizing atmospheres at 400-700°C, Corrosion Science (42), 1093-1122, 2000

42. D.O Albina (2005), MS Thesis, Columbia University.

43. C. Pettersson, J. Pettersson, H. Asteman, J.-E. Svensson, L.-G. Johansson, Corrosion Science 48, p.1368-1378 (2006).

44. H. J. Grabke, Materials and Corrosion, 54, p.736-746 (2003).

45. P. Henderson, P. Szakalos, R. Pettersson, C. Andersson and J. Högberg, Materials and Corrosion 57, p.128-134 (2006)

46. E. M. Levin, C. R. Robbing, H. F. McMurdie, Phase diagrams for ceramists, The American Ceramic Society Inc. (1969)

47. S. C. Cha, M. Spiegel, Materials and Corrosion 57, p.159-164 (2006)

48. A. Zahs., Spiegel, M. and Grabke J.H, " Chloridation and oxidation of iron, chromium, nickel and their alloys in chloridizing and oxidizing atmospheres at 400-700°C, Corrosion Science (42), 1093-1122, 2000

49. G.Y. Lai "Corrosion Mechanism and Alloy Performance in Waste-to-Energy Boiler Combustion Environment", 12th North American Waste-to-Energy Conference, Georgia USA, 2004

50. Y. Kawahara,., High temperature corrosion mechanisms and effect of alloying elements for materials used in waste incineration environment. Corrosion Science, 2002. 44(2): p. 223.

51. J. Pettersson, C. Pettersson, N. Folkeson, L.-G. Johansson, E. Skog, J.-E. Svensson, Materials Science Forum 522-523, p.563-570 (2006)

52. Babcock & Wilcox, Steam: its generation and use 40th edition

53. Adams, B., et al. Seghers Boiler Prism: a Proven Primary Measure against High Temperature Boiler Corrosion. in 12th North American Waste to Energy Conference. 2004. Savannah, U.S.A.

54. D.A. Jones, Principles and Prevention of Corrosion, 2nd Edition, Upper Saddle River, NJ Prentice Hall 1996

55. G. Wright, *Metals Handbook,* Vol 13. *Corrosion,* 9th edition, ASM International, Metals Park, OH, p. 97, 1987.

56. E. Hanson and M. Turner, "Second year Comparison of Superheater Metal Wastage Rates Utilizing Various Boiler Tube Alloys in a Waste-to-Energy Facility", Proceedings of the 11 Annual North American Waste to Energy Conference (NAWTEC 11), 2003.

57. M.A. Uusitalo, P.M.J. Vuoristo, Chlorine corrosion of thermally sprayed coatings at elevated temperatures, in: E. Lugsheider (Ed.), International Thermal Spray Conference, Essen, Germany, 4–6 March 2002, DVS, pp. 429–434.

58. G.Y Lai, *High Temperature Corrosion of Engineering Alloys,* ASM International, Materials Park, OH, 1990.

59. Bu-Qian Wang, Erosion-corrosion of coatings by biomass-fried boiler fly ash, Wear, 1995, 188 p.40-48.

60. R. Smith, Chemical Process: Design and Integration, Wiley and Sons

61. Y. Kawahara, M. Kira, Corrosion prevention of waterwall tube by field metal spraying in municipal waste incineration plants.

62. M.A. Uusitalo, Corrosion Science 46 (2004).

63. M. Spiegel, R. Warnecke, Performance of thermal spraycoatings under waste incineration conditions, in: Corrosion 2001, Houston, TX, Nace, paper 182.

64. L.N. Moskowitz, Journal of Thermal Spray Technology 2 (1993) 21.

65. K. Dopler, H. Kreye, R. Schwetzke, Journal of Thermal Spray Technology 9 (2000) 407.

66. S. Sharp, Sharp Consulting, "Energy from Biomass- Lessons Learned from European Boilers"

2011 PEERS Conference

67. F.J. Perez, J. Nieto, J.A. Trilleros, Materials Science Forum 522-523 (2006) 531-538.

68. E. Otero, A. Pardo, F.J. Perez, Oxidation of Metals, 49 (5/6) (1998) 467-484.

69. Bu-Qian Wang, Wear, 1995, 188, p 40-48.

70. Y. Kawahara, M. Kira, Corrosion, 1997, 53(3), p 241-251.

71. V. Fantini, Laser Cladding: a new technology for corrosion and erosion of boiler tubes, global solutions, Proceedings of the International Thermal Spray Conference (2007), 1120-1124.

72. J.M. Guilemany. M. Torrell, Journal of Thermal Spray Technology, 2008, 17(2), p 254-262

73. S.C. Cha, H.W. Gudenau, GT Bayer, Materials and Corrosion, 53 (2002) 195-205.

74. Bu-Qian Wang, Wear 1999 (1996) 268-274.

75. Ragnar Warnecke, Bernd Benker, Christian Deuerling, Ferdinand Haider, Siegried Horn, Jürgen Maguhn, Volker Müller, Hermann Nordsieck, Barbara Waldmann and Ralf Zimmermann, "The mechanisms of corrosion and how to avoid them", presented at 5th ISWA Beacon conference on Waste-to-Energy. October 25-26, 2007, Malmö, Sweden.

76. Sharp, Sharp Consulting, "Energy from Biomass- Lessons Learned from European Boilers"

77. E. Bjorkman, Energy & Fuels **1997,** 11, 1026-1032

78. D.A. Jones, Principles and Prevention of Corrosion, 2nd Edition, Upper Saddle River, NJ Prentice Hall 1996

79. D.O Albina (2005), MS Thesis, Columbia University

80. Vattefall, "ChlorOut Concept", http://chlorout.vattenfall.com/en/our-concept.htm.

81. S. Andersson, J. Froitzheim, E. Larsson and J.Pettersson, "Sulphur recirculation for increased electricity production in MSWI" Proceedings: International Symposium on Energy from Biomass and Waste Venice, Italy; 8-11 November 2010.

82. Wark, K., C.F. Warner, and W.T. Davis, Air Pollution: Its Origin and Control 3ed. 1997:Prentice Hall.

83. S. Goff, Dry scrubbing operation in WTEs Corrosion Research, J.T. Nickolas, Editor. 2008: New Jersey.

84. S.H. Lee, PhD Thesis (2009), Columbia University

85. Babcock & Wilcox, Steam: its generation and use 40th edition

86. S.H. Lee., N. J. Themelis, and M. Castaldi, High-Temperature Corrosion in Waste- to-Energy Boilers. Journal of Thermal Spray Technology, 2007. 16(1): p. 104-110.

87. MatWeb Website: Colmonoy

88. MatWeb Website: SP 99

89. P. J. Goodhew, J. Humphrey, R. Beanland, Electron Microscopy and Analysis 3rd Ed., Taylor and Francis, London (2001

90. A.S. Khanna (2002), High Temperature Oxidation and Corrosion, ASM International

91. Hitachi: http://www.microscopy.ou.edu/hitachi-3000.shtml

92. http://www.charfac.umn.edu/instruments/eds_on_sem_primer.pdf

93. D. Brune, R. Hellborg, H. J. Whitlow, O. Hunderi, Surface Characterization: A User's

94. G. Sorrel, Materials at High Temperature, 14. No. 3. 1997. 137-150. 21

95. AEBOM: Wood fuels handbook

96. Ya.E. Yudovich , M.P. Ketris International Journal of Coal Geology 67 (2006) 127–144.

97. A. Zahs, M. Spiegel, H. J. Grabke, Corrosion Science 42, p.1093-1122 (2000)

98. D. Young, (2008) High Temperature Oxidation and Corrosion of Metals, Elsiever.

99. Viklund et al. Oxidation of Metals August 2011, Volume 76, Issue 1, pp 111-12

100. S.H. Lee, PhD Thesis (2009), Columbia University

101. M. Spiegel, Materials and Corrosion 50, p.373-393 (1999).

102. N. Otsuka, Corrosion Science 50, p.1627-1636 (2008).

103. Kawahara, Y., Evaluation of high-temperature corrosion life using temperature gradient corrosion test with thermal cycle component in waste combustion environments. Materials and Corrosion,2006. 57(1): p. 60-72.

104. . K. Salmenoja, K. Mäkelä, "Prevention of Superheater Corrosion in the Combustion of Biofuels", Paper No. 238. Corrosion 2000 Orlando, USA (2000).
119. N. Folkeson, J. Pettersson, C. Pettersson, L.-G. Johansson, E. Skog, B.-Å. Andersson, S. Enestam, J. Tuiremo, A. Jonasson, B. Heikne, J.-E. Svensson, Materials Science Forum, 595-598, p.289-297 (2008)
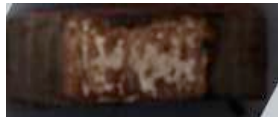
105. A. Zahs, M. Spiegel, H.J. Grabke, Corrosion Science 42 (2000) 1093.

106.. R. Pettersson, L. Liu, J. Sund, Corrosion Engineering, Science and Technology 40 (3), p. 211-216 (2005).

107. H. J. Grabke, E. Reese and M. Spiegel, Corrosion Science 37, p.1023-1043 (1995).

108 CRC Handbook of Chemistry

109. J. S. Kim, P. J. Xiang, and K. Y. Kim, Corrosion, February 2005, Vol. 61, No. 2, pp. 174-183

110. H.J. Park and H.W. Lee, Int. J. Electrochem. Sci., 9 (2014) 6687 – 6698

111. R.A. Antunes and M. C.L. de Oliveira , Corrosion Science 76 (2013) 6–26

112. M.A. Uusitalo et al. Corrosion Science 46 (2004) 1311–1331

113. https://web.anl.gov/PCS/acsfuel/preprint%20archive/Files/20_2_PHILADELPHIA_04-75_0094.pdf

114. S. Agblevor, *Energy & Fuels* 1995, 9, 635-640

115. Classification and comparison of municipal solid waste based on thermochemical characteristics Journal of the Air & Waste Management Association Volume 64, Issue 5, 2014

116. David J. Bayless a , Ashikur R. Khan a , Srinivas Tanneer a & Rajkumar Birru, "An Alternative to Additional SO3 Injection for Fly Ash Conditioning", Journal of the Air & Waste Management Association, 50:2, 169-174

117. Catalytic oxidation of SO_2 to SO_3 in the presence of fly ash US Patent 5011516S

118. Bryers, R. Flagging, Slagging, Fouling, and high Temperature Corrosion of Heat Transfer Surfaces due to Impurities in Steam Raising Fuels, Progress in Energy and Combustion Science Vol 22, pp 29-120, 1996

119. P. Koftsad, *High Temperature Corrosion,* 2nd Ed, Elsevier, New York, 1988

120. Krause, H.H. Effects of Flue Gas Temperature and Composition on Corrosion from Reuse Firing, Nace Conference 1991, Paper 242

121. Rademarkers, P., W. Hesseling, and J.v.d. Wetering, Review on corrosion in waste incinerators, and possible effect of bromine. 2002, TNO Industrial Technology.

122. Karlsson A, Moller P and Johansen V, "Iron and Steel Corrosion in a System of O_2, SO_2 and Alkali Chloride. The Formation of Low Melting Point Salt Mixture", Corrosion Science (30), pp. 153-158, Pergamon Press, 1990

123. Harb JN and Smith EE, "Fireside Corrosion in PC-Fired Boilers", Prog. Energy Combustion Science, 1990, Vol.16, pp 169-190

124. Fielder. W.; Stearns, C.; Kohl, F. Reaction of NaCl with Gaseous SO_3, SO_2, and O_2. *J.Electrochem. Soc.* 1984 *131,* 2414-2417

125. Boonsngsup, L.; Iisa, K.; Federick, W. Kinetics of the Sulfation of NaCl at Combustion Conditions, *Ind. Eng. Chem. Res.*, 1997, *36* (10), pp 4212–4216

126. D.A. Jones, Principles and Prevention of Corrosion, 2nd Edition, Upper Saddle River, NJ Prentice Hall 1996

127. E. Hanson and M. Turner, "Second year Comparison of Superheater Metal Wastage Rates Utilizing Various Boiler Tube Alloys in a Waste-to-Energy Facility", Proceedings of the 11 Annual North American Waste to Energy Conference (NAWTEC 11), 2003.

128. Hayden Laser Services:

https://de356l4tocdyu.cloudfront.net/pdf/LAM2012%20Presentation%2011.pdf

129. ASME Center for Research and Technology Development (CRTD) Volume 38 (1996): Assessment of Factor Affecting Boiler Tube Lifetimes in Waste-Fired Steam Generators: New Opportunities for Research and Development.

130. D. Joyner and G. Y. Lai, "Economic Impacts and solutions for waste-to-energy corroson management," Proceedsings of the 7th Annual North American Waste to Energy Conference (NAWTEC 7), 1999.

131. P. Viklund, (2011), PhD Thesis, KTH

132. M.A. Uusitalo et al. Corrosion Science 46 (2004) 1311–1331.

133. R.A. Antunes and M. C.L. de Oliveira , Corrosion Science 76 (2013) 6–26

Appendix A: Images of tests coupons

Images of coatings following 24 h experiments under NaCl layer and WTE synthetic flue gas mixture at 450, 500, and 550°C

Coating	450°C	500°C	550°C
Inconel 625			
Colmonoy 88 HVOF			
Colmonoy 88 laser			
SP 99			
SW1600			
SW1641			